

INVESTIGATIONS OF FLOW AND FILM COOLING ON TURBINE BLADE EDGE
REGIONS

A Dissertation

by

HUITAO YANG

Submitted to the Office of Graduate Studies of
Texas A&M University
in partial fulfillment of the requirements for the degree of

DOCTOR OF PHILOSOPHY

August 2006

Major Subject: Mechanical Engineering

INVESTIGATIONS OF FLOW AND FILM COOLING ON TURBINE BLADE EDGE
REGIONS

A Dissertation

by

HUITAO YANG

Submitted to the Office of Graduate Studies of
Texas A&M University
in partial fulfillment of the requirements for the degree of

DOCTOR OF PHILOSOPHY

Approved by:

Chair of Committee,
Committee Members,

J.C. Han
H.C. Chen
Taher Schobeiri
S.C. Lau

Head of Department,

Dennis O'Neal

August 2006

Major Subject: Mechanical Engineering

ABSTRACT

Investigations of Flow and Film Cooling on Turbine Blade Edge Regions.

(August 2006)

Huitao Yang, B.E.; Ph.D., Beijing University of Aeronautics and Astronautics, P.R. China

Chair of Advisory Committee: Dr. J.C. Han

The inlet temperature of modern gas turbine engines has been increased to achieve higher thermal efficiency and increased output. The blade edge regions, including the blade tip, the leading edge, and the platform, are exposed to the most extreme heat loads, and therefore, must be adequately cooled to maintain safety.

For the blade tip, there is tip leakage flow due to the pressure gradient across the tip. This leakage flow not only reduces the blade aerodynamic performance, but also yields a high heat load due to the thin boundary layer and high speed. Various tip configurations, such as plane tip, double side squealer tip, and single suction side squealer tip, have been studied to find which one is the best configuration to reduce the tip leakage flow and the heat load. In addition to the flow and heat transfer on the blade tip, film cooling with various arrangements, including camber line, upstream, and two row configurations, have been studied. Besides these cases of low inlet/outlet pressure ratio, low temperature, non-rotating, the high inlet/outlet pressure ratio, high temperature, and rotating cases have been investigated, since they are closer to real turbine working conditions.

The leading edge of the rotor blade experiences high heat transfer because of the stagnation flow. Film cooling on the rotor leading edge in a 1-1/2 turbine stage has been numerically studied for the design and off-design conditions. Simulations find that the increasing rotating speed shifts the stagnation line from the pressure side, to the leading edge and the suction side, while film cooling protection moves in the reverse direction with decreasing cooling effectiveness. Film cooling brings a high unsteady intensity of the heat transfer coefficient, especially on the suction side. The unsteady intensity of film cooling effectiveness is higher than that of the heat transfer coefficient.

The film cooling on the rotor platform has gained significant attention due to the usage of low-aspect ratio and low-solidity turbine designs. Film cooling and its heat transfer are strongly influenced by the secondary flow of the end-wall and the stator-rotor interaction. Numerical predictions have been performed for the film cooling on the rotating platform of a whole turbine stage. The design conditions yield a high cooling effectiveness and decrease the cooling effectiveness unsteady intensity, while the high

rpm condition dramatically reduces the film cooling effectiveness. High purge flow rates provide a better cooling protection. In addition, the impact of the turbine work process on film cooling effectiveness and heat transfer coefficient has been investigated. The overall cooling effectiveness shows a higher value than the adiabatic effectiveness does.

DEDICATION

To my parents, my sister, my wife Maggie, and my daughter Katherine.

ACKNOWLEDGMENTS

I would like to express my appreciation to Dr. J.C. Han and Dr. H.C. Chen, for their guidance, encouragement and help throughout my graduate study. I would like to thank Dr. M.T. Schobeiri and Dr. S.C. Lau, for their advice and sharing their time as committee members.

I am grateful to my parents and sister for their love, encouragement and support. I also thank my wife Maggie, for her endless support, and my lovely daughter Katherine, for her prayers. I owe them much.

Special thanks to my colleagues and friends, Lesley, Shantanu, Janice, Franz, Liu, Trent, Ahn, Xu, Lei, Gong and Hu. Their advice, help and friendship are greatly appreciated. I also wish to thank the staff at Texas A&M for their kindness and help provided during my study.

TABLE OF CONTENTS

	Page
ABSTRACT.....	iii
DEDICATION	v
ACKNOWLEDGMENTS.....	vi
TABLE OF CONTENTS.....	vii
LIST OF FIGURES.....	ix
LIST OF TABLES	xiv
NOMENCLATURE.....	xv
CHAPTER	
I INTRODUCTION.....	1
1.1 Background of Turbine Blade Cooling	1
1.2 Flow and Film Cooling on Blade Tip Region	1
1.3 Film Cooling on the Blade Leading Edge.....	3
1.4 Film Cooling and Heat Transfer on the Rotor Blade Platform	4
1.5 Objective.....	6
II NUMERICAL METHODOLOGY.....	7
2.1 Description of Conservation Equations	7
2.2 Reynolds Stress Turbulence Model	7
2.3 Near Wall Treatment.....	9
2.4 General Procedures of Numerical Simulation.....	10
III BLADE TIP LEAKAGE FLOW AND HEAT TRANSFER	11
3.1 Problem Definition, Computational Domain, and Boundary Conditions	11
3.2 Results and Discussion	13
3.2.1 Pressure and Velocity	13
3.2.2 Heat Transfer Distribution.....	21
3.2.3 Heat Load of the Various Blade Tips	28
3.3 Conclusions of Blade Tip Leakage Flow and Heat Transfer	31
IV BLADE TIP FILM COOLING	32
4.1 Arrangement of Film Holes on Blade Tip.....	32
4.2 Computational Details	35
4.3 Results and Discussions.....	38
4.3.1 Distribution of Pressure Ratio	37
4.3.2 Film Coolant Pathlines	41
4.3.3 Film Cooling Effectiveness.....	44
4.3.4 Effect of Rotation on Film Cooling Effectiveness	49
4.3.5 The Heat Transfer Coefficient of Film Cooling	55
4.4 Conclusions of Blade Tip Film Cooling	58
V FILM COOLING ON THE BLADE LEADING EDGE.....	59
5.1 Problem Definition and Computational Details.....	59
5.2 Results and Discussion for Two-Dimensional Study.....	62
5.3 Results and Discussion for Three-Dimensional Study.....	68

CHAPTER	Page
5.3.1 Flow Field	68
5.3.2 Heat Transfer Coefficient	71
5.3.3 Film Cooling Effectiveness	74
5.4 Conclusions of Film Cooling on the Rotor Blade Leading Edge.....	77
VI ROTOR BLADE PLATFORM FILM COOLING BY PURGE FLOW	79
6.1 Problem Definition and Computational Details	79
6.2 Flow Structure Study	84
6.3 Adiabatic Film Cooling Effectiveness Study	87
6.4 Heat Transfer Study	94
6.5 Turbine Work Process Impacting on Film Cooling Effectiveness.....	96
6.6 Conclusions of Platform Film Cooling	99
VII SUMMARY AND CONCLUSIONS	101
REFERENCES.....	104
VITA	110

LIST OF FIGURES

FIGURE	Page
3.1 Three tip configurations (top row), schematic of computational domain with different cross section planes (bottom left), and typical grid of squealer blade tip (bottom right)	11
3.2 Comparison of pressure ratio ($P_{in,t}/P$) distributions on pressure and suction sides of various blade tip configurations and flow conditions	14
3.3 Comparison of pressure ratio ($P_{in,t}/P$) distributions on the shroud of various blade tip configurations and flow conditions	17
3.4 Comparison of pathlines for flat tip, double squealer tip, and single suction side squealer tip configurations, as well as high parameter non-rotating and rotating cases	18
3.5 Comparison of streamlines and Mach number contours on mid-gap plane of various blade tip configurations and flow conditions	20
3.6 Comparison of streamlines and Mach number contours at pressure and suction side cross sections of different blade tip configurations for non-rotating and rotating cases	21
3.7 Comparison of heat transfer coefficient of single suction side squealer tip between experimental data and numerical predictions	22
3.8 Comparison of heat transfer coefficient of double squealer tip between experimental data and predictions	23
3.9 Comparison of Stanton number on the blade surface for various blade tip configurations	25
3.10 Comparison of the Stanton number on the shroud for various blade tip configurations	27
3.11 Comparison of Stanton number on the hub and root of blade	28
3.12 Heat transfer surface area of various tip configurations	29
3.13 Comparison of averaged heat transfer coefficient, heat load rate and Stanton number for various blade tip configurations	30
4.1 Film cooling effectiveness and heat transfer coefficient distribution of camber arrangement on the plane and squealer tips, Kwak and Han[18-19]	33
4.2 Various film hole arrangements on the plane and squealer tips	34
4.3 Comparison of tip leakage flow pathlines (colored by Mach number) between plane tip (a, Yang et al. [7]) and squealer tip (b, Yang et al.[8]) configurations	35
4.4 Geometry and numerical grids: (a) Schematic of typical film cooled GE-E3 blade with squealer tip and selected cross sections, and (b) detailed grid distribution of the film cooled squealer tip and film hole	36
4.5 Grid refinement study	38

FIGURE	Page
4.6 Comparison of the pressure ratio (P_t/P) distributions on the plane and squealer tips among various film hole arrangements with low parameter; $M = 1$ for camber and upstream configurations, $M=0.5$ for two-row configuration	40
4.7 Comparison of the pressure ratio (P_t/P) distributions on the plane and squealer tips among various film hole arrangements with low parameter; $M = 1$ for camber and upstream configurations, $M=0.5$ for two-row configuration	41
4.8 Comparison of film coolant pathlines (colored by dimensionless temperature) among various film hole arrangements with low parameter; $M = 1$ for camber and upstream configurations, $M=0.5$ for two-row configuration	43
4.9 Comparison of film cooling effectiveness on plane and squealer tips with various film hole arrangements and blowing ratios, low parameter.....	44
4.10 Comparison of film cooling effectiveness on the shroud for plane and squealer tip configurations with various film hole arrangements and blowing ratios, low parameter.....	47
4.11 Comparison of area averaged film cooling effectiveness on the blade tip with various tip configurations and film hole arrangements, low parameter, non-rotating	49
4.12 Comparison of coolant pathlines (colored by dimensionless temperature) for non-rotating and rotating cases, high parameter, $M = 1$	50
4.13 Comparison of (a) streamlines, Mach number contours on the mid-gap plane; and (b) tip leakage mass flow rate for non-rotating no film cooling (Yang et al.[22]), non-rotating film cooling, and rotating film cooling cases under high parameter conditions, $M=1$	52
4.14 Comparison of pathlines and dimensionless temperature contours at two stream wise cross sections, $M = 1$	53
4.15 Film cooling effectiveness comparison on the plane and squealer tips for $M=1$ under various flow conditions.....	55
4.16 Comparison of heat transfer coefficients on the plane tip (left) and squealer tip (right) of camber arrangement, low parameter, $M = 1$	57
4.17 Comparison of instantaneous Stanton number contours on the plane and squealer tips and shrouds for the high parameter, non-rotating and rotating cases.....	57
5.1 Computational domain and grids of a three-dimensional 1-½ turbine stage. (Passage was repeated three times).....	60
5.2 Film cooled leading edge of a rotor blade and grid structure.....	61
5.3 Grid independency study	62

FIGURE	Page
5.4 Velocity field of two-dimensional 3 turbine stage: a) instantaneous streamlines based on the absolute reference, b) instantaneous streamlines based on the relative reference, c) rotor inlet velocity triangle, and d) stagnation lines of various rotating speed on the leading edge of the three-dimensional rotor blade	64
5.5 Rotor unsteady heat transfer comparison between without and with film cooling, 2500 rpm condition, M=1: a) instantaneous and averaged heat transfer coefficient without film cooling, b) unsteady intensity of heat transfer without film cooling, c) instantaneous and averaged heat transfer coefficient with film cooling, and d) unsteady intensity of heat transfer with film cooling.....	66
5.6 Rotor unsteady film cooling effectiveness and intensity, 2550 rpm condition, M=1: a) instantaneous and averaged film cooling effectiveness, and b) unsteady intensity of the film cooling effectiveness.....	67
5.7 Stator 1 wake (colored by relative Ma number) and rotor relative positions for various time phases, 2550 rpm condition, M=1.....	68
5.8 Velocity contours comparison (colored by relative Mach number) at station 2 for various time phases, 2550 rpm condition, M=1.....	69
5.9 Static pressure distribution of 1-1/2 turbine stage for four time phases, 2550 rpm condition, M=1	70
5.10 Comparison of instantaneous coolant pathlines (colored by the particle number) at four time phases as well as three work conditions, M=1	72
5.11 Heat transfer coefficient comparison of stator and rotor blades in 1-1/2 stage turbine for four time phases, design condition, M=1.....	73
5.12 Heat transfer coefficient comparison at leading edge of rotor for four time phases with three working conditions, M=1	74
5.13 Film cooling effectiveness comparison on the rotor blade for four time phases with three working conditions, M=1	75
5.14 Comparison of the predicted (time phase 1) and measured film cooling effectiveness on the leading edge of rotor with three working conditions, M=1.....	76
5.15 Comparison of predicted (time phase 1) and measured film cooling effectiveness on the rotor blade for three blowing ratios, design condition	77
6.1 (a) Computational domain of slot film cooled platform in a 1-1/2 turbine stage, and (b) numerical grids (repeated two times and the cyan color is the cooled platform).....	79
6.2 Detailed grid distributions near the angled coolant slot.....	81
6.3 Grid refinement study for laterally averaged adiabatic temperature on rotating blade platform.....	82

FIGURE	Page
6.4 Scheme comparison for laterally averaged adiabatic film cooling effectiveness (a) and cooling effectiveness unsteady intensity, 2550 rpm, MFR=1% (M=0.24)	83
6.5 (a) Vertical cross section plane and (b) the corresponding dimensionless temperature contours and streamlines, 2550 rpm, MFR=0.5% (M=0.12)	84
6.6 (a) Conceptual rotor inlet velocity triangle and (b) relative velocity incidence angle to the rotor leading edge for various working conditions	85
6.7 Comparison of (a) pressure ratio and (b) streamlines and dimensionless temperature contour on the annular cross plane for various working conditions, time phase $\frac{1}{4}$	86
6.8 Comparison of static pressure contours on the rotor blade hub region: (a) without purge flow and (b) with purge flow; 2550 rpm, time phase $\frac{1}{4}$, MFR=1% (M=0.24).....	87
6.9 Adiabatic total wall temperature comparison with and without purge flow on the rotating blade platform, time phase $\frac{1}{4}$, MFR=1% (M=0.24).....	88
6.10 Comparison of adiabatic film cooling effectiveness on the rotating blade platform for various time phases and rpms, MFR=1%, (M=0.24)	89
6.11 (a) Laterally averaged adiabatic cooling effectiveness comparison for various rpms with MFR=1%; (b) Instantaneous and time averaged adiabatic film cooling effectiveness for 2550 rpm, MFR=1% (M=0.24); (c) Laterally averaged unsteady intensity of adiabatic cooling effectiveness for various rpms, MFR=1%,(M=0.24)	91
6.12 Adiabatic film cooling effectiveness comparison on the rotating blade platform between simulation and experiment for various MFRs, 2550 rpm	92
6.13 Laterally averaged adiabatic cooling effectiveness comparison between simulation and experiment for various MFRs, 2550 rpm.....	92
6.14 Laterally averaged adiabatic film cooling effectiveness comparison between simulation and experiment on the rotating blade platform for various rotating speeds, MFR=1%, (M=0.24)....	93
6.15 Adiabatic film cooling effectiveness comparison on the rotor blade suction side for various rotating speeds, time phase $\frac{1}{4}$, MFR=1% (M=0.24)	94
6.16 Overall heat transfer coefficient and heat transfer coefficient comparison on the rotating platform for various time phases, 2550 rpm, MFR=0.5% (M=0.12)	95
6.17 Overall heat transfer coefficient and heat transfer coefficient comparison for the whole turbine stage, 2550 rpm, time phase $\frac{1}{4}$, MFR=0.5% (M=0.12)	96
6.18 Area averaged total/static temperature for various stations in the turbine stage, 2550 rpm.....	97
6.19 Coolant 3-D image comparison contoured by the adiabatic film cooling effectiveness (a) and overall film cooling effectiveness (b) inside a rotor passage for various rotating speeds, time phase $\frac{1}{4}$, MFR=1% (M=0.24).....	98

FIGURE	Page
6.20 Overall film cooling effectiveness comparison on the rotating blade platform for various time phases, 2550 rpm, MFR=1%, ($M=0.24$)	99

LIST OF TABLES

TABLE		Page
3.1	Summary of simulated cases.....	13
4.1	Matrix of numerical simulations.....	39
5.1	Matrix of simulation cases.....	63

NOMENCLATURE

A	heat transfer area (m ²)
c	sound speed (m/s)
C	tip gap clearance (% of the blade span)
C _p	heat capacity at constant pressure (J/kg-K)
C _x	axial chord length of the rotor blade (m)
D	depth of the squealer cavity, or hydraulic diameter (m)
DR	density ratio = ρ_c/ρ_∞
E	total energy (J)
F	force vector (N)
g	gravity acceleration (m/s ²)
h	height of blade, or local convective heat transfer coefficient = $q_w/(T_w-T_{aw})$ (W/m ² K)
h _{overall}	local overall convective heat transfer coefficient = $q_w/(T_w-T_{in,o})$ (W/m ² K)
H	total enthalpy (W/m ² -K)
K	turbulence kinetic energy, or thermal conductivity (W/m ² -K)
m	mass (kg)
M	global film coolant blowing ratio = $(\rho_c V_c)/(\rho_{ave} V_{ave})$, or $(\rho_c V_c)/(\rho_\infty W_{D \text{ or Off}})$
Ma	Mach number, v/c
MFR	purge-to-mainstream mass flow ratio = $M_c/M_\infty = (A_c \rho_c V_c)/(A_\infty \rho_\infty V_\infty)$
Nu	Nusselt number = $h D / K$
P	local static pressure (pa)
Pr	Prandtl number = $\mu/\rho C_p$
PR	pressure ratio
q	heat flux (w/m ²)
Q	total heat flow (w)
Re	Reynolds number = uD/v
S	total entropy (J/kgmol-K)
St	Stanton number, $h/(\rho_{in} V_{in, relative} C_p)$
T	temperature (K)
Tu	inlet turbulence intensity level (%)
Tu _h	heat transfer coefficient unsteady intensity level (%)
Tu _{η}	unsteady intensity of cooling effectiveness = $\sqrt{\frac{\sum(\eta_i - \bar{\eta})^2}{N}} / \bar{\eta}$ (%)
U	rotor rotating speed (m/s)
V	absolute inlet velocity of rotor (m/s)

W	relative inlet velocity of rotor (m/s)
u,v,w	velocity vector component (m/s)
x,y,z	coordinate
y*	dimensionless distance of the first grid to the wall, $y^* = \rho C_{\mu}^{1/4} k_p^{1/2} y_p / \mu$

Greek Symbols

α	absolute flow angle
β	relative flow angle, or coefficient of thermal expansion (K^{-1})
η	overall film cooling effectiveness = $(T_{t\infty} - T_{aw, f}) / (T_{t\infty} - T_{tc})$
η_{aw}	adiabatic film cooling effectiveness = $(T_{aw, 0} - T_{aw, f}) / (T_{aw, 0} - T_{tc})$
i	flow incidence angle
ϕ	dimensionless temperature = $(T_{t\infty} - T_i) / (T_{t\infty} - T_{tc})$
ρ	density (kg/m^3)
ε	turbulent dissipation rate (m^2/s^3)
ν	kinematics viscosity (m^2/s)
ω	angular velocity (rpm)
μ	dynamic viscosity (Pa-s)
τ	shear stress (pa), or time scale (s)
Ω	angular speed (rpm)

Subscripts

0	without film cooling
2	station 2
3	station 3
ave	average of cascade inlet and outlet
a	adiabatic
c	coolant
f	with film cooling
t	stagnation flow condition or total value, or turbulence
out	outlet of the cascade
p	the first grid near the wall
i,j,k	index for tensor
in	inlet of the cascade
w	wall
∞	inlet stream of cascade

CHAPTER I

INTRODUCTION

1.1. Background of Turbine Blade Cooling

Gas turbines are widely used for aircraft propulsion and land-based power generation or industrial applications. Thermal efficiency and power output of gas turbine increase with increasing turbine rotor inlet temperatures. The operating temperatures are far above the permissible metal temperatures. Therefore, there is a need to cool the blades for safe operation. The blades are cooled by extracted air from the compressor of the engine. Since this extraction incurs a penalty to the thermal efficiency, it is necessary to understand and optimize the cooling technique. Han et al. [1] have made a good summary of heat transfer and cooling technology of gas turbines. The turbine blade edge regions include blade tip, leading edge, platform, and trailing edge. Most often these regions are critical due to the high heat load. In this study, the first three edge regions have been numerically and experimentally studied for the flow, film cooling and its heat transfer.

1.2. Flow and Film Cooling on Blade Tip Region

The turbine blade tip is directly exposed to the hot leakage flow driven by the pressure difference between the blade pressure and suction sides. The blade tip experiences a high heat load and it is one of the most difficult regions to be cooled effectively. In order to reduce the tip leakage flow and heat transfer, various squealer tip configurations are investigated. The squealer tip acts as a labyrinth seal and increases the flow resistance, consequently it leads to low leakage flow and low heat transfer rate

Many numerical studies have been conducted recently to investigate the blade tip heat transfer. Ameri et al.[2] used TRAF3D.MB code to study the effect of squealer tip on rotor blade heat transfer. Also Ameri et al.[3] studied the effects of tip gap clearance and casing recess on heat transfer and stage efficiency for several squealer blade tip geometries. Ameri and Bunker [4] performed a computational study to investigate the detailed heat transfer distributions on blade tip surfaces for a large power generation turbine and compared their result with the experimental data of Bunker et al.[5]. Ameri et al.[6] computed the flow and heat transfer of a blade tip with a mean-camberline strip tip. Yang et al.[7-8] numerically studied the flow and heat transfer around the GE-E³ blade with a flat tip and a squealer tip with various turbulence models. The predicted heat transfer coefficients are in reasonable agreement with the experimental results of Azad et al.[9-10].

Experimental studies have also been conducted to investigate the heat transfer and flow on the gas

The dissertation style and format follow that of the ASME Journal of Turbomachinery.

turbine blade tip. Azad et al.[9-10] studied the flow and heat transfer on the first stage blade tip of an aircraft engine turbine (GE-E3) by the thermo liquid crystal technique. The results show that the squealer tip can reduce the heat transfer coefficient compared with the flat tip configuration. Azad et al.[11] also studied the effect of squealer geometry arrangement on gas turbine blade tip heat transfer. Papa et al.[12] measured average and local mass transfer coefficients on a squealer tip and winglet-squealer tip using the naphthalene sublimation technique. They also presented the flow visualization on the tip surface using an oil dot technique. Kwak et al.[13] and Kwak and Han[14-15] measured heat transfer coefficients on the tip and near tip regions of both plane and squealer tip blades by transient liquid crystal technique. They showed that the heat transfer coefficient is higher on the tip than that of the near tip region. In addition, the heat transfer coefficient on the cavity floor will be reduced with increasing squealer rim. The single suction side squealer is the best configuration to reduce the heat transfer coefficient on the cavity floor.

A common way to provide adequate cooling of the blade tips is to extract some cooling air from the coolant passages, through the film holes to protect tip surface from the hot leakage gas. It is important to systematically study the arrangement of film holes, the associated blowing ratio, and the tip structure affecting the film cooling effectiveness and heat transfer coefficient. At present, most experiments of film cooling on the turbine blades can only be performed for the non-rotating cases with a relative low cascade inlet/outlet pressure ratio due to the limitation of test rigs. In order to use these experimental data for film cooling applications under real engine conditions, it is desirable to employ advanced numerical methods which are capable of simulating the effects of blade rotation and high cascade inlet/outlet pressure ratio for practical engine operation conditions.

There have been numerous studies that addressed the film cooling and heat transfer on the blade tip. Kim et al.[16] presented a summary of the heat transfer coefficient and film cooling on blade tip model studied by Dr. Metzger. Numerical studies to investigate blade tip film cooling have also been conducted. Ameri and Rigby [17] calculated heat transfer and film cooling effectiveness on film cooled turbine blade models. Kwak and Han[18-19] used the transient liquid crystal method to investigate the film cooling with thirteen (13) film holes located along the camber line of the GE-E³ blade tip. They concluded that: the coolant injection slightly reduces the heat transfer coefficient downstream of the film holes; film-cooling effectiveness increases with increasing blowing ratio for all cases; and the squealer tips have higher cooling effectiveness compared with plane tips. Most importantly, their study also indicated that the camber line film-hole arrangement does not provide adequate protection for the high heat transfer areas on either the plane or squealer blade tips since the film cooling are effective only on the downstream side of the tip leakage flow where the heat transfer coefficients are relatively low. Acharya et al.[20] performed numerical simulation of film cooling on GE-E³ plane and squealer tips for the same GE-E³ blade of Kwak and Han[18-19] but with only seven (7) film holes along the camber line of the blade tip. Their numerical studies indicated that: the film coolant acts as a blockage to the tip leakage flow due to the lower coolant

velocity compared to the tip leakage flow; the coolant trajectory is directed from the pressure side to the suction side for the plane tip, but it rolls inside the cavity from leading portion suction side to the trailing portion suction side for the squealer tip; the film cooling effectiveness of tip and shroud increases with increasing blowing ratio; the film cooling generally decrease the heat transfer downstream of the film holes instead of increasing it as observed in other film cooling applications. Hohlfeld et al.[21] predicted film cooling flow from dirt purge holes on the tip of a turbine blade using the Fluent CFD code. They found that the flow exiting the dirt purge holes act as a blockage for the leakage flow across the gap. As the blowing ratio increased for a large tip gap, the tip cooling increases only slightly while the cooling to the shroud increases significantly. Recently, Ahn et al. [22] have performed the film cooling study on the GE-E3 blade tip with pressure sensitive paint (PSP) technique. The technique employs mass transfer similarity, can isolate the heat conduction error near the film holes region, thus provide more accurate results compared with other thermo methods.

1.3. Film Cooling on the Blade Leading Edge

Besides the investigation of heat transfer and film cooling on the blade tip, several experiments have been carried out to study the heat transfer on the leading edge of the rotors. Dunn et al.[23-24] used a full stage rotating turbine of the Garrett TFE 731-2 engine in a shock-tunnel facility and thin-film heat flux gages to study heat transfer on the vane, end-walls and rotors. Abhari and Epstein[25] studied the time-resolved heat transfer for cooled and un-cooled rotors by thin heat flux gages. They found that the heat transfer was highly unsteady for transonic turbine rotors. Takeishi et al.[26] employed the CO₂ mass transfer analogy technique to measure the local film cooling effectiveness on a rotor blade, and found higher cooling effectiveness on the suction side compared to the pressure side of the blade. They believed that this phenomenon is caused by the effect of the radial flow and strong mixing on the pressure surface. Cameci and Arts[27-28] made high pressure rotor blade heat transfer measurements in a short duration wind tunnel facility. They found that the cooling efficiency increases with decreasing T_c/T_{in} (i.e., coolant temperature / inlet gas temperature). Mehendale et al.[29-30] studied the effect of high free stream turbulence and upstream wake on heat transfer and film cooling of a rotor blade in a low speed wind tunnel facility. They concluded that the high turbulence and wake increases the heat transfer slightly, but significantly reduces the film cooling effectiveness for lower blowing ratio conditions. Also, Du et al.[31] used the same facility to study the effect of a simulated unsteady wake on the detailed Nusselt number and film cooling effectiveness distribution of a rotor blade by the transient liquid crystal technique.

Before introduce a recent film cooling study, it is desirable to beriefly describe a high pressure three-stage research turbine facility at the Turbomachinery Performance and Flow Research Laboratory (TPFL) of Texas A&M University. This “state-of-the-art” facility was built by Schobeiri and his colleagues (references [32]-[33]), and produced a bunch of useful results for turbine aerodyanics and performance.

Schobeiri et al. [32] have used this facility to experimentally investigate aerodynamics and performance of three stage high pressure turbine with 3-D blade for both design and off-design conditions. In addition, Schobeiri et al. [33] systematically studied the three stages turbine aerodynamics and performance with 3-D bowed blades and 2-D cylindrical blades. They concluded that the 3-D bowed blades can improve the turbine performance and reduced the secondary flow. Recently, based on this “state-of-the-art” three-stage turbine rig, Ahn et al.[34] used a pressure sensitive paint (PSP) technique to study the detailed distribution of film cooling effectiveness on the leading edge of the first stage rotor blade. They concluded that the film cooling shifts with increasing rpm, the cooling effectiveness slightly decreases with increasing blowing ratio in the leading edge region of the rotating blade.

Numerical predictions of heat transfer and film cooling on rotor blades have been performed by many researchers. Abhari et al.[35] examined the time-resolved aerodynamics and heat transfer in a transonic turbine rotor. They concluded that there is relatively little difference between the steady state turbulent and the time averaged unsteady calculations. In general, the measured Nusselt number is either higher than or equal to the predicted Nusselt number. Dunn et al.[36] reported the time-averaged Stanton number and the surface pressure distribution for the first stage vane row and the first stage blade row. They found that the heat transfer shows small differences of prediction among different turbulence models. Leading edge film cooling with compound angle holes has also been numerically studied by Lin et al.[37] using CFL3D code. Compared to the experimental data, the numerical prediction shows a good agreement in the trend of the adiabatic film cooling effectiveness, but the value is over-predicted. Garg and Ameri[38] used $q-\omega$, $k-\epsilon$, and $k-\omega$ turbulence models to predict the heat transfer on a film cooled airfoil. Overall, the $q-\omega$ model and the $k-\epsilon$ model predict similar results, while the $k-\omega$ model predicts higher heat transfer coefficients.

1.4. Film Cooling and Heat Transfer on the Rotor Blade Platform

In addition to the film cooling research on the blade tip and leading edge regions mentioned before, the platform of a rotor blade has been studied to investigate the secondary flow effect on the film cooling and its heat transfer. More and more low-aspect ratio and low-solidity rotor have been used to improve the turbine performance; therefore the endwall-effect becomes significantly important. Harasgama and Burton [39-40] reported heat transfer measurements on film-cooled endwalls of an annular cascade of turbine nozzle guide vanes, and they found the Nu number gradually increases from the leading edge to the trailing edge on the endwall. Friedrichs et al. [41] presented adiabatic film cooling effectiveness distributions on the endwall of a large scale, low speed linear turbine cascade using the ammonia-diazo technique. They reported that the horseshoe vortex from the pressure side moving across the passage pushes most of the coolant from the middle of the passage toward to the suction surface. Recently, Roy et al. [42] used experimental and numerical methods to study the flow and heat transfer on the vane hub.

They found that the flow field predicted by the Fluent CFD code is in good agreement with the experimental data. Burd and Simon [43-44] experimentally studied the effects of slot bleed injection on a contoured end-wall of nozzle guide vane, and found that the coolant accumulates near the suction surface for the low bleed flow rate. Radomsky and Thole [45] employed Laser Doppler Velocimeter (LDV) and infrared (IR) camera to study the effect of turbulence intensity on the end-wall heat transfer. They concluded that the leading edge horseshoe vortices are similar for low and high turbulence intensity conditions, and the high turbulence intensity produces high St number. Lin and Shih [46] used CFL3D (version 5) code with the shear-stress-transport (SST) $k-\omega$ turbulence model to study the gap leakage flow on contouring endwall. They found that all types of the contour end-walls will reduce the secondary flow, but only the through blade contour endwall increases the film cooling effectiveness. Nicklas [47] used an IR camera to study the film-cooled turbine endwall in a transonic cascade, and suggested to shift the slot upstream of the rotor leading edge to avoid increasing the horseshoe vortex. Knost and Thole [48] used the Fluent CFD code to predict the endwall film cooling for a first stage vane, and indicated that the superposition overpredict the film cooling effectiveness along the endwall for the combined endwall film cooling and slot cooling configurations. Zhang and Moon [49] used the Pressure Sensitive Paint (PSP) technique to study the effect of back-facing step on the endwall film cooling, and found that the back-facing step causes an unstable boundary layer and damages the film coverage. Han and Goldstein [50] used mass transfer technique to study the leading edge fillet effect on the endwall heat transfer, and summarized that the fillet significantly reduce the horseshoe vortex for the low turbulence intensity conditions, but increases the leading edge corner vortices. Cardwell et al. [51] measured the endwall film cooling adiabatic effectiveness with realistic features including a combustor to turbine interface gap, a vane to vane mid-passage gap, and a platform misalignment and surface roughness.

Most recently, Suryanarayanan et al. [52] employed the PSP technique to measure the film cooling on the rotating platform in a complete turbine stage, which is closer to the real engine working conditions. Again, their experiment has been carried out in the high pressure three-stage research turbine facility at the Turbomachinery Performance and Flow Research Laboratory (TPFL) of Texas A&M University. In addition, the more detailed information regarding this test rig can be referred in Schobeiri et al. [32-33]. PSP is a mass transfer technique which reduces the heat conduction error near the film holes and eliminates the turbine work effect in the measurement of film cooling effectiveness. They found that the film cooling effectiveness on the rotating blade platform increases with increasing coolant purge rate. In addition, increasing rotating speed also enhanced the film cooling effectiveness for the range of rotating speeds (1500, 2000 and 2550 rpm) considered in their study. Until now, very few researches were reported in the literature to study the stator-rotor interaction on the detailed film cooling effectiveness and the associated heat transfer coefficient on the rotating platform in a complete turbine stage. In the present study, numerical simulations were performed to investigate film cooling and heat transfer on the rotating

platform in a 1-½ turbine stage for various working conditions. The geometry considered in the present numerical simulations is similar to the turbine stage studied experimentally by Suryanarayanan et al. [52].

1.5. Objective

As mentioned previously, the blade edge regions are critical in durability due to high heat load. In spite of the extensive studies dedicated on them, most of the previous work was far away from the real turbine working conditions.

For the blade tip, due to the limitations in experimental facilities, most of the experimental studies were performed under relatively low inlet/outlet pressure ratio and non-rotating conditions, which are far from the real turbine operating conditions. It is, therefore, desirable to investigate the effects of high pressure ratio and high rotating speed on blade tip film cooling and heat transfer under more realistic engine conditions. The proposed study focuses on the numerical prediction of film cooling and heat transfer of GE-E³ blade with various blade tip configurations, including a flat tip, a double squealer tip, and a single suction-side squealer tip as tested in Kwak et al.[14]. The numerical results for the non-rotating, low temperature and low pressure ratio cases were compared with the experimental data of Kwak et al.[14]. Calculations were also performed for both the non-rotating and rotating blades at high total temperature, high Mach number, and high pressure ratio conditions to provide a detailed understanding of the blade tip leakage flow and heat transfer characteristics under more realistic engine conditions.

For the blade leading edge, most of the former studies are performed on a single non-rotating rotor blade, while a real engine turbine stage includes several rows of stators and rotors. The presented work aims to enhance the understanding the turbine flow physics under more realistic working conditions by considering a whole turbine stage, i.e., including stator-rotor interaction. The unsteady characters of film cooling effectiveness and its heat transfer coefficient caused by the stator-rotor interaction, and the effect of turbine work process on film cooling, have been studied to facility a better understanding. Also the effects of design and off-design conditions on film cooling, such as low RPM and high RPM, have been investigated.

For the rotor blade platform, most of the previous studies isolate the rotor platform from the turbine stage, and do not consider the upstream stator effects and turbine work process. This study includes upstream stator 1, rotor and its platform, downstream stator 2, which consider the effect of stator-rotor interaction on the platform film cooling and the associated heat transfer coefficient, as well as the turbine work process. Therefore, it can investigate the detailed unsteady flow physics of film cooling caused by the stator-rotor interaction. In addition, the effects of off-design conditions and purge flow rate on film cooling have been studied. The impact of turbine work process on film cooling effectiveness and heat transfer coefficient has been investigated. These proposed studies are unique in its nature, and no similar work has ever been reported on the open literature.

CHAPTER II

NUMERICAL METHODOLOGY

2.1. Description of Conservation Equations

All the simulations were performed by using the CFD software package Fluent [53] (Version 6). The solutions were obtained by solving the compressible Reynolds-Averaged Navier-Stokes (RANS) equations using a finite volume method to discretize the continuity, momentum and energy equations; and SIMPLEC algorithm is used to couple the pressure and velocity.

The continuity equation is:

$$\frac{\partial \rho}{\partial t} + \nabla \cdot (\rho \vec{v}) = S_m \quad (2.1)$$

where S_m is the source term for combustion or mass transfer simulation.

The Reynolds-Averaged Navier-Stokes equation is:

$$\frac{\partial}{\partial t}(\rho u_i) + \frac{\partial}{\partial x_j}(\rho u_i u_j) = -\frac{\partial p}{\partial x_i} + \frac{\partial}{\partial x_j} \left[\mu \left(\frac{\partial u_i}{\partial x_j} + \frac{\partial u_j}{\partial x_i} - \frac{2}{3} \delta_{ij} \frac{\partial u_l}{\partial x_l} \right) \right] + \frac{\partial}{\partial x_j} (-\rho \overline{u_i' u_j'}) \quad (2.2)$$

The last term, i.e., Reynolds stress, is solved by Reynolds stress model.

The energy equation is:

$$\frac{\partial}{\partial t}(\rho E) + \frac{\partial}{\partial x_i} [u_i(\rho E + p)] = \frac{\partial}{\partial x_j} \left[\left(k + \frac{C_p \mu_t}{Pr_t} \right) \frac{\partial T}{\partial x_j} + u_i(\tau_{ij})_{eff} \right] + s_h \quad (2.3)$$

where Pr_t is turbulent Pr number, and the default value is 0.85. Source term S_h is the energy contributed by chemical reaction or radiation.

2.2. Reynolds Stress Turbulence Model

The Reynolds stress model involves calculation of the individual Reynolds stresses by using differential transport equations. The individual Reynolds stresses are then used to obtain closure of the Reynolds-averaged momentum equation.

The exact form of the Reynolds stress transport equations can be derived by taking moments of the exact momentum equation. This is a process wherein the exact momentum equations are multiplied by a fluctuating property, the product then being Reynolds-averaged. However, several of the terms in the exact equation are unknown and modeling assumptions are required in order to close the equations.

The Reynolds stress transport equations are presented together with the modeling assumptions required to attain closure. Details can be obtained in a review by Hanjalic [54]

The exact transport equations for the transport of the Reynolds stresses, $\overline{\rho u'_i u'_j}$, can be written as follows:

$$\begin{aligned}
& \underbrace{\frac{\partial}{\partial t}(\overline{\rho u'_i u'_j})}_{\text{Local_Time_Derivative}} + \underbrace{\frac{\partial}{\partial x_k}(\overline{\rho u'_k u'_i u'_j})}_{C_{ij}=\text{Convection}} = \\
& - \underbrace{\frac{\partial}{\partial x_k}[\overline{\rho u'_i u'_j u'_k} + \rho(\delta_{kj} u'_i + \delta_{ik} u'_j)]}_{D_{T,ij}=\text{Turbulent_Diffusion}} + \underbrace{\frac{\partial}{\partial x_k}[\mu \frac{\partial}{\partial x_k}(\overline{u'_i u'_j})]}_{D_{L,ij}=\text{Molecular_Diffusion}} \\
& - \underbrace{\rho \overline{u'_i u'_k} \frac{\partial u'_j}{\partial x_k} + \overline{u'_j u'_k} \frac{\partial u'_i}{\partial x_k}}_{P_{ij}=\text{Stress_Production}} - \underbrace{\rho \beta (\overline{g_i u'_j \theta} + \overline{g_j u'_i \theta})}_{G_{ij}=\text{Buoyancy_Production}} \\
& + \underbrace{\rho \left(\frac{\partial u'_i}{\partial x_j} + \frac{\partial u'_j}{\partial x_i} \right)}_{\phi_{ij}=\text{Pressure_Strain}} - \underbrace{2\mu \frac{\partial u'_i}{\partial x_k} \frac{\partial u'_j}{\partial x_k}}_{\varepsilon_{ij}=\text{Dissipation}} \\
& - \underbrace{2\rho \Omega_k (\overline{u'_j u'_m} \varepsilon_{ikm} + \overline{u'_i u'_m} \varepsilon_{jkm})}_{F_{ij}=\text{Production_by_System_Rotation}} + \underbrace{S_{user}}_{\text{User-Defined_Source_Term}} \quad (2.4)
\end{aligned}$$

Of the various terms in these exact equations, convection term C_{ij} , molecular diffusion term $D_{L,ij}$, stress production term P_{ij} , and rotation production term F_{ij} do not require any modeling. However, turbulent diffusion term $D_{T,ij}$, buoyancy production term G_{ij} , pressure strain term ϕ_{ij} , and dissipation term ε_{ij} need to be modeled to close the equations. The following sections describe the modeling assumptions required to close the equation set.

$D_{T,ij}$ can be modeled by using a scalar turbulent diffusivity as follows:

$$D_{T,ij} = \frac{\partial}{\partial x_k} \left(\frac{\mu_t}{\sigma_k} \frac{\partial \overline{u'_i u'_j}}{\partial x_k} \right) \quad (2.5)$$

The classical approach to modeling ϕ_{ij} uses the following decomposition:

$$\phi_{ij} = \phi_{ij,1} + \phi_{ij,2} + \phi_{ij,w} \quad (2.6)$$

where $\phi_{ij,1}$ is the slow pressure-strain term, also known as the return-to-isotropy term, $\phi_{ij,2}$ is called the rapid pressure-strain term, and $\phi_{ij,w}$ is the wall-reflection term.

The slow pressure-strain term, $\phi_{ij,1}$, is modeled as

$$\phi_{ij,1} = -c_1 \rho \frac{\varepsilon}{k} [\overline{u'_i u'_j} - \frac{2}{3} \delta_{ij} k] \quad (2.7)$$

with $C_1 = 1.8$.

The rapid pressure-strain term, $\phi_{ij,2}$, is modeled as

$$\phi_{ij,2} \equiv -c_2[(P_{ij} + F_{ij} + G_{ij} - C_{ij}) - \frac{2}{3}\delta_{ij}(P + G - C)] \quad (2.8)$$

where $C_2 = 0.60$, P_{ij} , F_{ij} , G_{ij} , and C_{ij} are defined as in Equation (2.4), $P = \frac{1}{2}P_{kk}$, $G = \frac{1}{2}G_{kk}$, and $C = \frac{1}{2}C_{kk}$.

The wall-reflection term, $\phi_{ij,w}$, is responsible for the redistribution of normal stresses near the wall. It tends to damp the normal stress perpendicular to the wall, while enhancing the stresses parallel to the wall. This term is modeled as

$$\begin{aligned} \phi_{ij,w} = & c_1' \frac{\varepsilon}{k} (\overline{u'_k u'_m n_k n_m} \delta_{ij} - \frac{3}{2} \overline{u'_i u'_k n_j n_k} - \frac{3}{2} \overline{u'_j u'_k n_i n_k}) \frac{k^{3/2}}{c_i \varepsilon d} \\ & + c_2' (\phi_{km,2} n_k n_m \delta_{ij} - \frac{3}{2} \phi_{ik,2} n_j n_k - \frac{3}{2} \phi_{jk,2} n_i n_k) \frac{k^{3/2}}{c_i \varepsilon d} \end{aligned} \quad (2.9)$$

where $C_1 = 0.5$, $C_2 = 0.3$, n_k is the x_k component of the unit normal to the wall, d is the normal distance to the wall, and $c_i = c_\mu^{3/4} / k$, where $c_\mu = 0.09$ and k is the von Kármán constant ($= 0.4187$). $\phi_{ij,w}$ is included by default in the Reynolds stress model.

2.3. Near Wall Treatment

The non-equilibrium wall function is widely used for these engineering simulations, because this near wall treatment can dramatically save computer resource and yield reasonable good results. The two key elements in the non-equilibrium wall functions are as follows:

- 1) Launder and Spalding's [55] log-law for mean velocity is sensitized to pressure-gradient effects, therefore the standard wall function can not handle complicated flow involved in the present studies.
- 2) The two-layer-based concept (by Chen and Patel, [56]) is adopted to compute the budget of turbulence kinetic energy (G_k , $\bar{\varepsilon}$) in the wall-neighboring cells.

The log-law for mean velocity sensitized to pressure gradients is

$$\frac{\tilde{U} C_\mu^{1/4} k^{1/2}}{\tau_w / \rho} = \frac{1}{k} \ln \left(E \frac{\rho C_\mu^{1/4} k^{1/2} y}{\mu} \right) \quad (2.10)$$

where

$$\tilde{U} = U - \frac{1}{2} \frac{dp}{dx} \left[-\frac{y_v}{\rho k \sqrt{k}} \ln \left(\frac{y}{y_v} \right) + \frac{y - y_v}{\rho k \sqrt{k}} + \frac{y_v^2}{\mu} \right] \quad (2.11)$$

The non-equilibrium wall function employs the two-layer concept in computing the budget of turbulence kinetic energy at the wall-adjacent cells, which is needed to solve the k equation at the wall-

neighboring cells. The wall-neighboring cells are assumed to consist of a viscous sublayer and a fully turbulent layer. The following profile assumptions for turbulence quantities are made:

$$\tau_t = \begin{cases} 0, & y < y_v \\ \tau_w, & y > y_v \end{cases} \quad k = \begin{cases} \left(\frac{y}{y_v}\right)^2 k_p, & y < y_v \\ k_p, & y > y_v \end{cases} \quad \varepsilon = \begin{cases} \frac{2\nu k}{y^2}, & y < y_v \\ \frac{k^{3/2}}{c_\mu y}, & y > y_v \end{cases} \quad (2.12)$$

Using these profiles, the cell-averaged production of k , G_k , and the cell-averaged dissipation rate, $\bar{\varepsilon}$, can be computed from the volume average of G_k and ε of the wall-adjacent cells. It effectively relaxes the local equilibrium assumption (production = dissipation) that is adopted by the standard wall function in computing the budget of the turbulence kinetic energy at wall-neighboring cells. Thus, the non-equilibrium wall functions, in effect, partly account for non-equilibrium effects neglected in the standard wall function.

Because of the capability to partly account for the effects of pressure gradients and departure from equilibrium, the non-equilibrium wall functions are recommended by Fluent for use in complex flows involving separation, reattachment, and impingement where the mean flow and turbulence are subjected to severe pressure gradients and change rapidly. In such flows, improvements can be obtained, particularly in the prediction of wall shear (skin-friction coefficient) and heat transfer (Nusselt or Stanton number).

2.4. General Procedures of Numerical Simulation

The computational fluid dynamics process includes three parts, such as pre-process, process, and post-process. Firstly, a CAD software, such as AutoCAD or SolidWorks, is employed to build geometry according to the physical model of the projects; Some unnecessary part, including fillets, screw holes, need to be neglected or simplified. Then the solid geometry is exported to the Gambit, a mesh building software, to generate grids. Note that the grid of some critical regions, such as interested region, near wall region, high gradient of pressure and velocity region, need to be refined to achieve the accurate numerical resolution. This process is called pre-process. The Fluent reads this grid file, sets up boundary conditions based on the physical model, to calculate the conservation equations by iteration. Also some techniques, such as multi grid, are applied to speed up the convergence. This process is named as process. Finally, a photographic software, TecPlot, is employed to read the result files exported by Fluent and to plot simulated results. Analysis should be made based on these results. This is called post-process. For most of these cases, Reynolds stress turbulence model together with non-equilibrium wall function is applied to solve the turbulence flow.

CHAPTER III

BLADE TIP LEAKAGE FLOW AND HEAT TRANSFER

3.1. Problem Definition, Computational Domain and Boundary Conditions

The blade tip is a critical region due to high tip leakage flow and thin thermo boundary layer, which has been fully discussed in chapter I. The most recent review regarding the blade tip heat transfer has been made by Bunker [57]. It is, therefore, desirable to study the tip configurations to reduce the tip leakage flow and the heat load. Computations were performed for the GE-E³ blade tip flow and heat transfer with Fluent by solving compressible Reynolds-Averaged Navier-Stokes equations using the finite volume method to discretize the equations. The GAMBIT grid generation software was used to generate unstructured grids, with fine grid clustering in the near wall and tip regions.

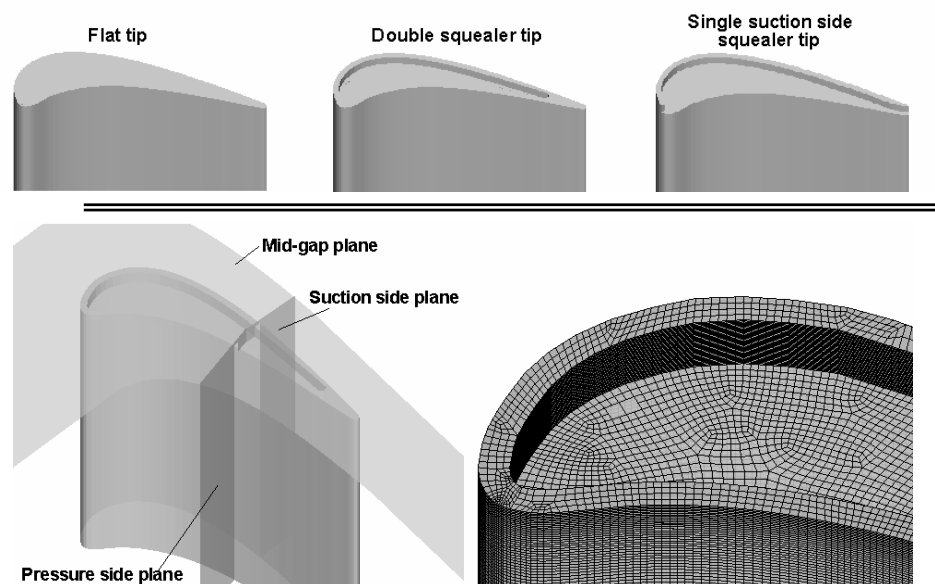


Figure 3.1 Three tip configurations (top row), schematic of computational domain with different cross section planes (bottom left), and typical grid of squealer blade tip (bottom right).

In order to facilitate a direct comparison with the experimental data of Kawak et al.[13], the present calculations were performed for a 3X scaled up model of the GE-E³ blade. Figure 3.1 shows the geometry and numerical grids for the GE-E³ blade with various blade tip configurations. It should be remarked that the blade geometry used in Kwak et al.[13] and the present study is a two-dimensional blade with the same blade profile in the spanwise direction from the blade root to tip. Furthermore, the present 2D blade profile and the inlet flow angle are identical to those at the tip section of the actual GE-E³ blade since Kwak et

al.[13] and the present study are concerned with the heat transfer characteristics in the blade tip region. The top row of Figure 3.1 shows the three tip configurations including the flat tip, double squealer tip and single suction side squealer tip. The left side bottom of Figure 3.1 illustrates the schematic of the double squealer blade tip geometry with selected cross sectional planes which will be used later to show the flow structures around the blade tip region. Also the detailed grid distribution has been plotted in the right side bottom of Figure 3.1. The scaled up blade has a constant axial chord length of 8.61 cm, and an aspect ratio (span to the chord) of 1.4. The blade leading edge pitch is 9.15 cm. The depths (D) of the squealer cavity are 0.254 cm, 0.508 cm, and 0.762 cm, which are 2.1 %, 4.2 % and 6.3 % of the blade span, respectively. In the present simulations, the blade tip clearance is kept constant with a tip gap of 1.97 mm or 1.5% of the blade span height (H). The effect of different tip gap clearances on the blade tip heat transfer has been investigated experimentally by Azad et al. [9,10], and numerically by Yang et al. [7,8], and will not be repeated here.

The computational domain consists of a single blade with periodic conditions imposed along the boundaries in the circumferential (pitch) direction. The inlet boundary is placed at one-half chord length upstream of the blade so that the simple uniform inflow boundary conditions can be employed. Calculations were performed first for the non-rotating case using the experimental conditions of Kwak et al.[13]. The total temperature (300K) and total pressure (130.0 kPa) are specified along with the inlet flow angle (32 degree) and turbulence intensity level (9.7%). The corresponding Mach number at the inlet is 0.25. The exit boundary is located at one chord length downstream of the blade trailing edge to provide appropriate resolution of the tip leakage flow and passage vortices. The static pressure is specified as 108.3 kPa at the exit. Therefore, the inlet total pressure to the outlet static pressure ratio ($PR=P_{in,t}/P_{out}$) is 1.2. On the blade surface, the no-slip condition and uniform wall temperature conditions were specified.

For completeness, simulations were also performed for the same 3X scaled up GE-E³ blade using typical operating conditions for a real turbine with a blade tip radius of 35.56 cm (14 in.ch) under both non-rotating and rotating conditions. This enables us to evaluate the effects of rotation, high temperature, high Mach number, and high inlet/outlet pressure ratio on the overall heat transfer in the blade tip region. A rotating speed of 9,600 rpm is used in the present rotating blade simulation. The inlet total temperature is specified at 1479 K (2662°R) and the blade surface temperature is 1035 K. The inlet turbulence intensity is 9.7%, and the inlet flow angle is 32 degree. The total pressure at the inlet is 1.675 MPa and the static pressure at the exit is 1.027 MPa. This gives a inlet/outlet pressure ratio (PR), $P_{in,t}/P_{out}$, of 1.63, which is significantly higher than the 1.20 used in the experiments of Kwak et al.[13]. For convenience, the simulations at high total temperature and high inlet/outlet pressure ratio cases are denoted as “high parameter”, while the low inlet/outlet pressure ratio and low total temperature cases corresponding to the experimental conditions are denoted as “low parameter” in the following discussions. For the rotating cases, the blade domain is rotating with a relative inlet flow angle equal to 32 degree, while the shroud

remains stationary. All other conditions are kept the same as the high parameter stationary case to facilitate a detailed understanding of the effects of blade rotation under realistic turbine working conditions.

For blade tip leakage flow and heat transfer simulations, Yang et al.[7,8] showed that the Reynolds Stress Model (RSM) of Hanjalic [54] performs slightly better than the high Reynolds number k- ϵ model and RNG k- ϵ model. In all cases, non-equilibrium wall function is employed to handle the near wall turbulence. The y^* value is adjusted iteratively to about 30 by splitting or merging the near wall grids to satisfy the requirement of non-equilibrium wall function. Unless otherwise indicated, the results presented in this paper are based on the RSM model, the tip clearance is 1.5% of the blade span and the depth of the squealer cavity is 4.2% of the blade span. A total of 13 simulations were performed for the non-rotating and rotating blades with various blade tip configurations as shown in Table 3.1.

Table 3.1 Summary of simulated cases.

	Flat tip	Double squealer			Single suction side squealer		
		2.1%	4.2%	6.3%	2.1%	4.2%	6.3%
Non-rotating, low parameters	X	X	X	X	X	X	X
Non-rotating, high parameters	X		X			X	
Rotating, high parameters	X		X			X	

All the cases presented are converged to residual levels of the order of 10^{-5} , and to less than 0.01% error in the mass flow rate between the inlet and exit of the computational domain. Typically, 800 iterations are required for the convergence. For the squealer tip configuration considered here, typically the calculation is performed with about 1 million nodes, with the grid point distribution outside the squealer tip region being similar to that in the flat tip study. The grid independency has been studied by Yang et al [7].

3.2. Results and Discussion

3.2.1. Pressure and velocity

Figure 3.2 shows a comparison of the pressure ratio ($P_{in,t}/P$) distributions for both the non-rotating and rotating cases with three blade tip configurations including the flat tip, double squealer tip and single suction-side squealer tip. For completeness, the corresponding pressure ratio ($P_{in,t}/P$) distributions on the shroud of all three tip configurations are also shown in Figure 3.3 to facilitate a more detailed understanding of the flow in the blade tip region. In both Figures, generally the high value of $P_{in,t}/P$ ratio corresponds to low static pressure and high velocity. The pressure pattern on the shroud matches the corresponding pressure ratios on the blade tip since the pressure variation across the narrow tip gap

clearance is relatively small. Noted that the pressure ratio is quite low on the pressure side, but becomes significantly higher on the suction side. Due to the favorable pressure gradient between the pressure and suction sides of the blade, the flow is accelerated through the gap between the blade tip and the shroud. For the non-rotating cases, it is clearly seen that the effect of tip leakage flow is confined to a small region near the blade tip, and the pressure ratio on the other portions of the blade side shows two-dimensional distribution. Under the rotating conditions, however, the pressure contours becomes highly three-dimensional on the blade suction side due to the migration of blade passage vortex towards the blade tip region as a result of the rotation-induced centrifugal and Coriolis forces. On the blade pressure side, the pressure ratio is only slightly affected by the blade rotation. On the other hand, the high pressure ratio (i.e., high velocity) region on the blade suction side was pushed downstream towards the trailing edge and also radially outward to the blade tip region. Moreover, the overall pressure ratio increases significantly on both the blade suction side and tip region in comparison with the stationary case. It is quite clear that the centrifugal and Coriolis forces tend to increase the blade tip leakage flow and produce stronger leakage vortices on the suction side of the blade tip region for both the flat tip and squealer tip configurations.

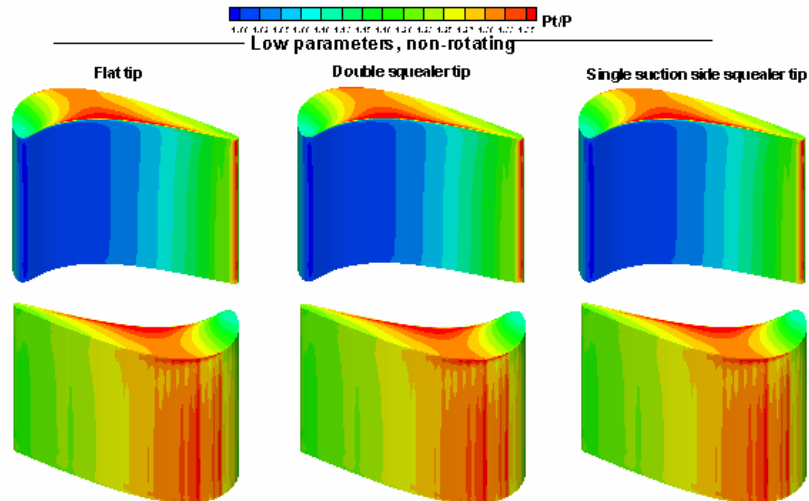


Figure 3.2 Comparison of pressure ratio ($P_{in,t}/P$) distributions on pressure and suction sides of various blade tip configurations, and flow conditions.

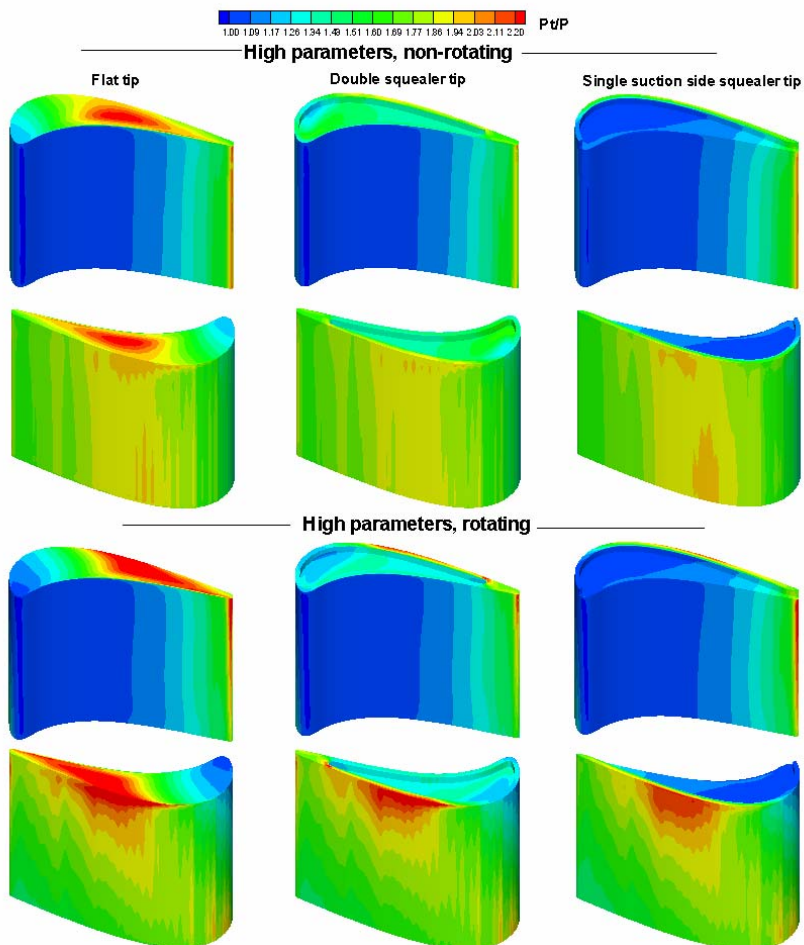


Figure 3.2 Continued.

For the non-rotating flat tip configuration under experimental conditions (i.e., low $T_{in,t}$ and $P_{in,t}/P_{out}$), high pressure ratios were observed in the mid-chord region and along the edge of the pressure side blade tip, indicating the presence of strong leakage flow through the mid-chord section of the blade tip gap clearance. For the double squealer tip configuration, the pressure ratio is high on the squealer rim due to local flow acceleration in the narrow gap on the top of the squealer rim, but drops significantly inside the squealer cavity due to flow separation behind the pressure side squealer rim. The pressure ratio inside the squealer cavity is much lower than that observed in the flat tip case, indicating that the tip leakage flow is significantly reduced in the double squealer tip configuration. For the single suction-side squealer tip configuration, a high pressure ratio region is again observed on top of the squealer rim. However, the low pressure ratio region on the pressure side was extended over most of the blade tip surface with a drastic reduction of the tip leakage flow across the suction side squealer rim. Based on the pressure ratio distributions on the blade tip and shroud, it is quite clear that the single suction side squealer tip is the

most effective configuration for the reduction of the tip leakage flow among the three different blade tip configurations considered in the present study.

For the non-rotating cases with high inlet/outlet pressure ratio and high total temperature (i.e., high parameters) conditions, the overall pressure ratio level is significantly higher than the corresponding low parameter cases. Furthermore, the high pressure ratio regions on the suction side and the blade tip were shifted downstream for both the flat and squealer tip configurations as seen in Figures 3.2 and 3.3. Consequently, the strongest tip leakage flow was observed in the downstream section of the blade where the blade thickness is relatively small. For the rotating case, the blade tip velocity is 357.5 m/s (i.e., 9,600 rpm) is nearly twice of the blade inlet velocity of 183 m/s but the inlet/outlet pressure ratio, total temperature, and the relative inlet flow angle are kept the same as the non-rotating high-parameter case. It is clearly seen from Figure 3.2 that the blade rotation results in a significant increase of pressure ratio in the blade tip gap region and on the blade suction side. In general, the rotation tends to increase the leakage flow and produce a large leakage vortex on the suction side for both the flat and squealer tip configurations. Furthermore, the leakage flow was observed to shift towards the trailing edge where the blade is relatively thin and harder to cool. Similar pressure ratio patterns were also observed on the shroud as shown in Figure 3.3. Details of the leakage vortices and their effects on the blade tip and shroud heat transfer will be discussed later.

Figure 3.4 shows the pathlines around three blade tip configurations under various flow conditions. For completeness, the pathlines and Mach number contours at the mid-gap between the blade tip and shroud are also shown in Figure 3.5 to facilitate a detailed understanding of the blade tip leakage flow for both the non-rotating and rotating cases. For the flat tip configuration, the fluid accelerates through the tip gap and combines with the mainstream flow on the suction side to form a tip leakage vortex. The velocity of tip leakage vortex is slower than the flow in other regions. For the double squealer tip, the flow structure around the tip is more complicated than the other two cases. In addition to the tip leakage vortex near the blade suction side, another vortex was formed inside the squealer cavity when the fluid enters the squealer cavity from the leading edge and pressure side of the blade tip. The vortex rolls down the pressure side squealer rim to form a large recirculation flow region inside the squealer cavity. It then rolls up across the suction side squealer rim and merges into the suction side tip leakage vortex. Also it is found that the velocity of vortex inside the squealer cavity decreases from the leading edge to the trailing edge. For the single suction-side squealer tip configuration, a leakage vortex was formed along the junction of the blade tip and the squealer rim. The vortex rolls up across the squealer rim and merged into the tip leakage vortex on the blade suction side. It is worthwhile to note that the structure of the tip leakage flow for the non-rotating cases does not change significantly between the low parameter and high parameter conditions.

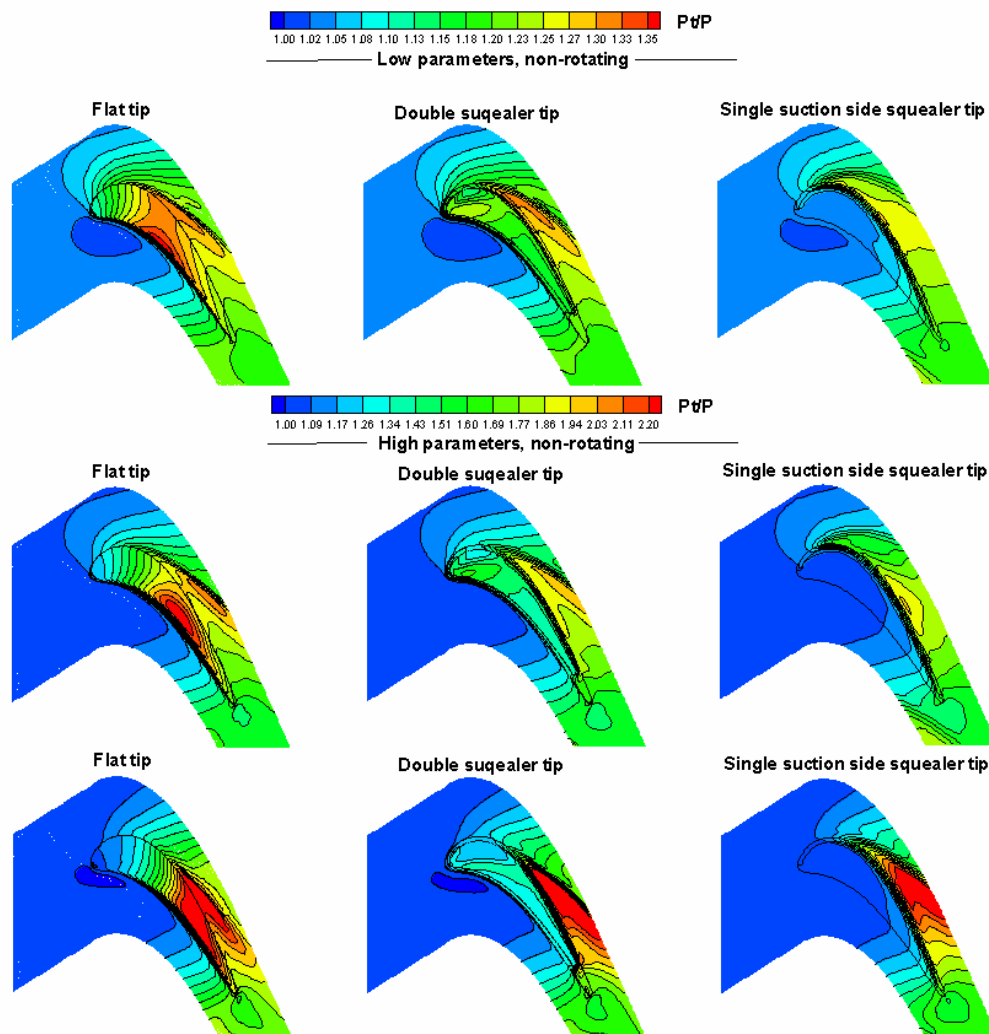


Figure 3.3 Comparison of pressure ratio ($P_{in,t}/P$) distributions on the shroud of various blade tip configurations and flow conditions.

For the rotating cases, the pathlines are plotted using the relative velocity in a rotating reference frame. In order to facilitate a more detailed understanding of the flow pattern in the blade tip region, two different sets of pathlines were released at the cascade inlet. The first set of pathlines was released at the same location as the non-rotating cases while a second layer of pathlines was released inside the shroud boundary layer. In general, the tip leakage flow in the blade tip gap region is still driven by the pressure gradient between the pressure and suction sides of the blade similar to that observed for the non-rotating cases. However, the tip leakage flow pattern is significantly modified by the rotation-induced centrifugal and Coriolis forces. Furthermore, the pathlines near the stationary shroud wall are deflected toward the pressure side of the blade since the flow inside the shroud boundary layer lags behind the rotating blade

due to the viscous effects. The centrifugal force, however, did not drive the leakage vortex in the radial outside direction. Because this force is a body force, and builds up a pressure gradient based on the shroud, which balances the centrifugal force. In the body force field, only the buoyancy force caused by the temperature gradient is net force and moves the fluid.

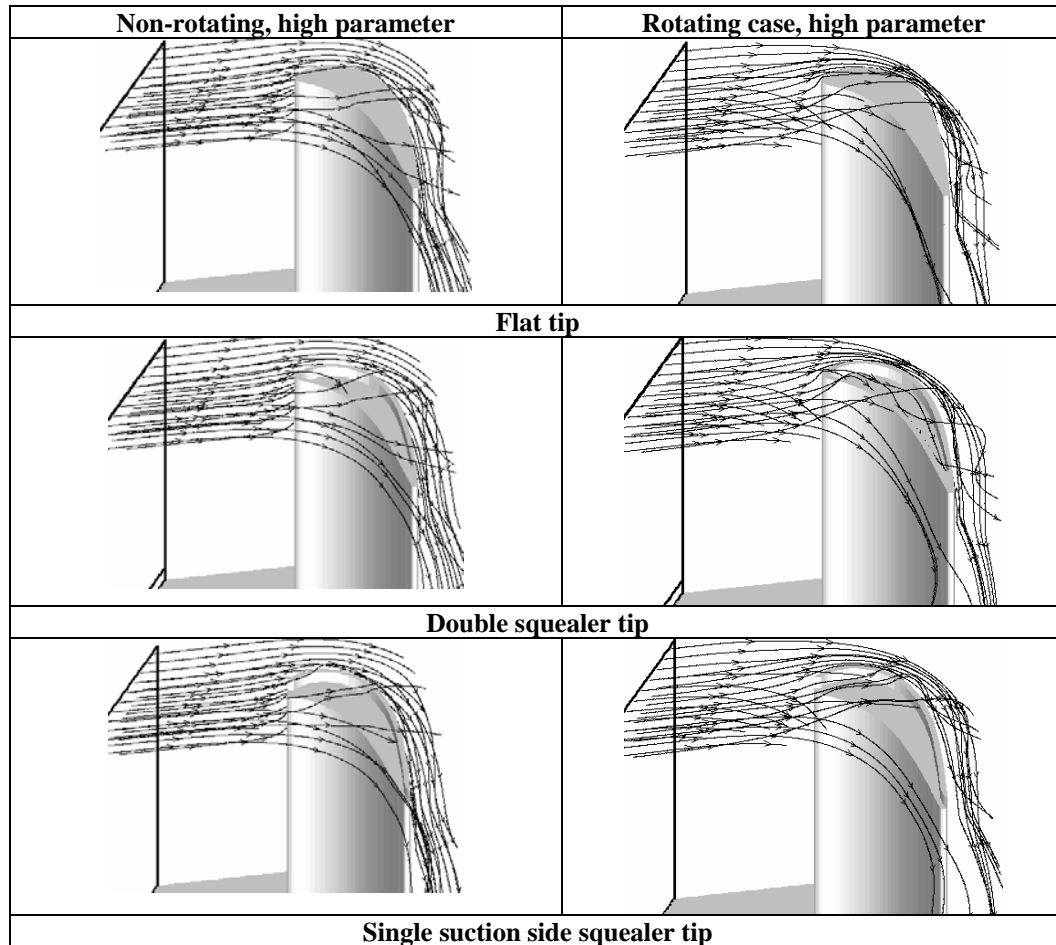


Figure 3.4 Comparison of pathlines for flat tip, double squealer tip, and single suction side squealer tip configurations, as well as high parameter non-rotating and rotating cases.

Figure 3.5 shows a comparison of the pathlines and Mach number contours for both the non-rotating and rotating high parameter cases to provide a more detailed understanding of the effects of rotation on the tip leakage flow patterns. This study only focuses on the heat transfer on the tip region, the grid resolution, or scheme of pressure based arithmetic can not catch the shock accurately. For the non-rotating cases shown in the first column of Figure 3.5, the tip leakage flow at the mid-gap plane is driven from the pressure side to the suction side, and the pathlines converge to form a leakage vortex in the suction side blade passage. When the blade is rotating at the designed speed of 9,600 rpm, the absolute flow velocity

and the approach angle were adjusted so that the inflow angle relative to the rotating blade remains the same at 32 degree. The second and third columns of Figure 3.5 show the pathlines and Mach number contours at the mid-gap plane for the rotating cases in the earth-fixed (i.e., absolute velocity) and rotating (i.e., relative velocity) reference frames, respectively. For completeness, the pathlines and Mach number contours at mid-span plane is also shown in the last column of Figure 3.5 to illustrate the three-dimensional flow pattern under rotating conditions. It is quite clear that the pathlines at the mid-span plane for the rotating cases have the same relative inlet flow angle as that observed for the non-rotating cases since the flow in the mid-span is not directly affected by the blade tip leakage flow. In the mid-gap plane, however, the flow at the turbine inlet was deflected towards the pressure side (see column 3) since the approach flow inside the shroud boundary layer lags behind the rotating blade due to the viscous shear stress exerted by the stationary shroud. In the mid-gap between the blade tip and the shroud, the leakage flow is subjected to the combined effect of shroud viscous force and the pressure gradients between the pressure and suction sides of the rotating blade. It is quite clear that the pressure gradient across the tip gap is strong enough to overcome the viscous resistance of the stationary shroud and push the tip leakage flow from the pressure side to suction side. It should be noted that the absolute velocity of the tip leakage flow must be faster than the rotating blade in order to push the fluid from the pressure side to the suction side of the rotating blade. In general, the flow pathlines are quite similar between the non-rotating and rotating cases, indicating that the tip leakage flow is still dominated by the pressure gradients across the tip gap under the rotating conditions.

Figure 3.6 shows the comparison of streamlines and Mach number contours at two streamwise cross sections (i.e., the pressure side and suction side planes in Figure 3.1) for the flat tip, double squealer tip, and single suction side squealer tip for both the non-rotating and rotating cases with 4.2% tip clearance. In order to facilitate a detailed understanding of the secondary flow patterns induced by the pressure gradient and blade rotation for different blade tip configurations, the pressure side and suction side planes were chosen to be perpendicular to blade pressure and suction sides, respectively, and intersect at the camber line. For all three different blade tip configurations, low velocity exists on the pressure side while the velocity on the suction side is significantly higher. Fluid is driven by the pressure difference between the pressure and suction sides of the blade and accelerates through the blade tip region. The tip leakage flow is combined with the inlet passage flow to form the leakage vortex in the suction side as seen in the pathlines shown earlier in Figure 3.4. For the double squealer tip, a recirculation flow region was observed inside the squealer cavity due to flow separation behind the pressure side squealer rim. For single suction side squealer tip, a large recirculation region is observed in front of the rim.

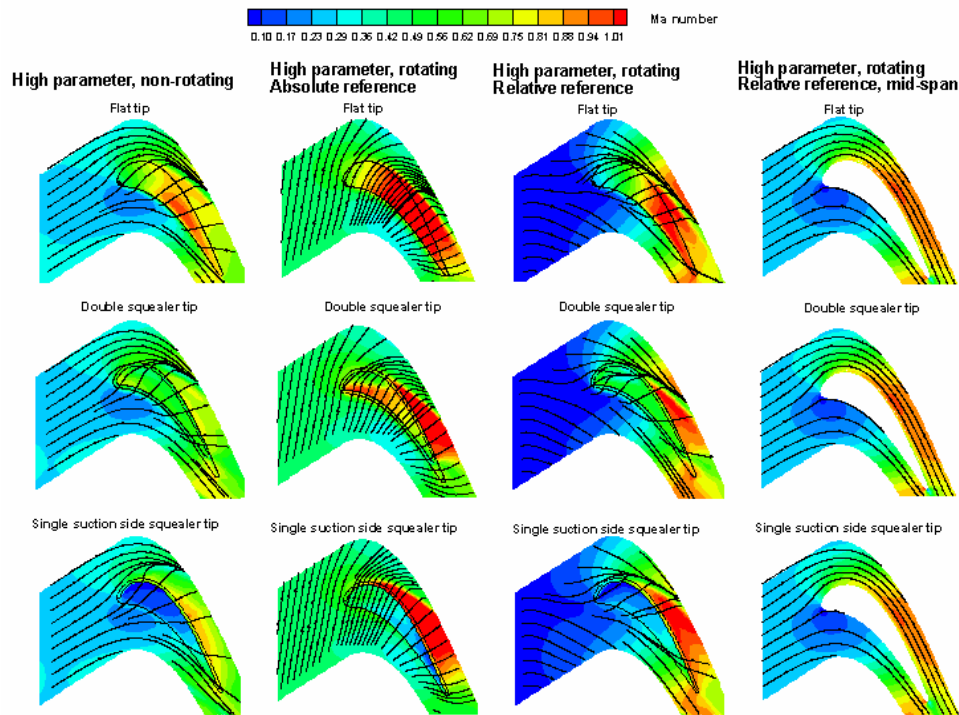


Figure 3.5 Comparison of streamlines and Mach number contours on mid-gap plane of various blade tip configurations and flow conditions.

For the non-rotating cases, the leakage flow structures for the high parameter cases are similar to those for the low parameter cases on the pressure suction and in the squealer cavities although the Mach number is significantly higher for the high parameter cases. As noted earlier in Figure 3.3, the tip leakage flow increases for the high parameter cases and the location of the maximum tip leakage was pushed towards the trailing edge. Consequently, the location and shape of the leakage vortex changed significantly at the suction side plane for both the double and single suction side squealer tip configurations.

For the rotating cases, the absolute velocity of the leakage flow is very high near the stationary shroud as seen from the earth-fixed reference frame. However, it is not possible to see the recirculation region inside the squealer cavity in earth-fixed frame since the fluid moves together with the blade at a very high absolute velocity. For completeness, the pathlines and Mach number contours are also plotted in a blade-fixed reference frame using relative velocities as shown in the bottom row of Figure 3.6 to facilitate a better understanding of the tip leakage flow under rotating conditions. It is clearly seen that the blade rotation has significantly changed the size and shape of the leakage vortices for both the flat and squealer tip configurations. Due to the rotation-induced centrifugal force, the passage flow is pushed outward in the radial direction. The effect of rotation on passage flow migration is most noticeable on the pressure side of shroud boundary layer since the passage flow in that region has relatively low momentum and can

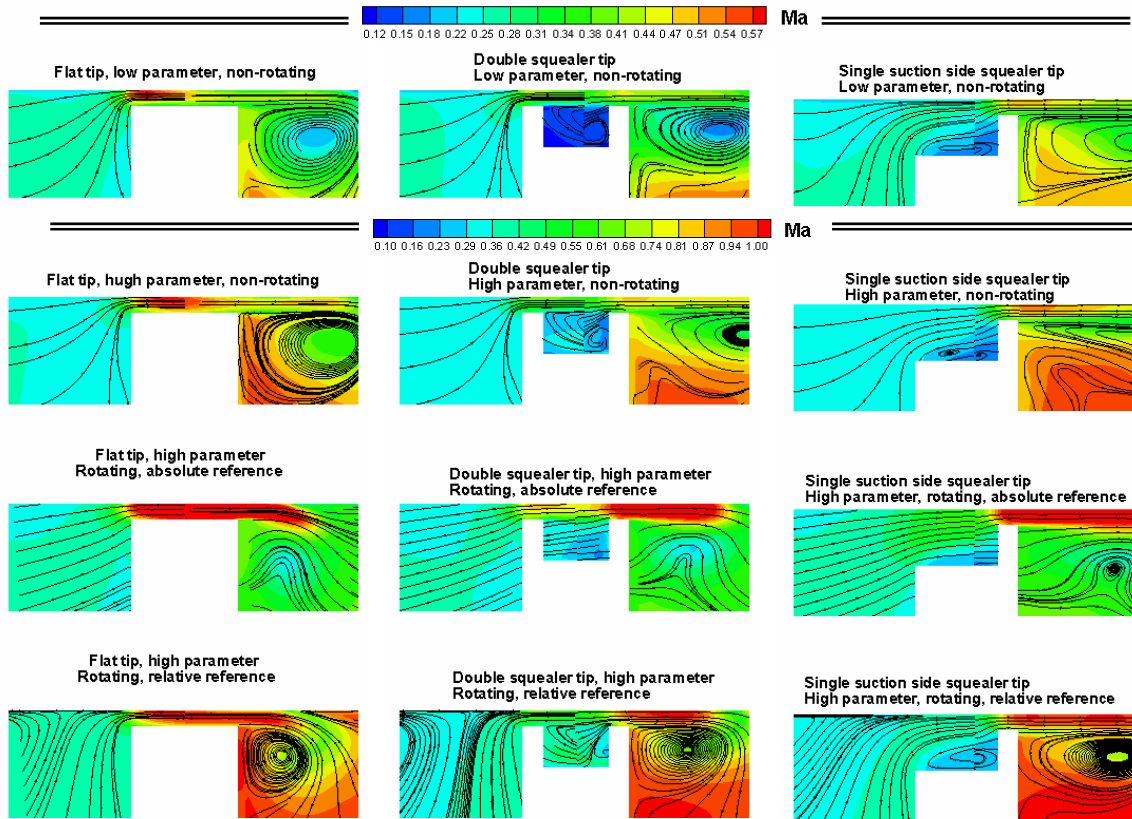


Figure 3.6 Comparison of streamlines and Mach number contours at pressure and suction side cross sections of different blade tip configurations for non-rotating and rotating cases.

therefore be easily deflected by the centrifugal force. When the radially outward passage flow impinges on the stationary shroud surface, a portion of the flow is pushed from the pressure side through the blade tip gap towards the suction side. The remaining passage flow is pushed away from the rotating blade since it has a slower absolute velocity due to the viscous effects inside the shroud boundary layer. On the suction side, the blade rotation also induced radially outward flow which tends to reduce the size of the tip leakage vortex and push it closer to the suction side rim. However, the rotation effect is less obvious since the suction side passage flow possesses significantly higher momentum and the centrifugal force is not strong enough to produce appreciable changes in the suction side flow pattern.

3.2.2 Heat Transfer Distribution

Figure 3.7 shows a comparison of the predicted and measured heat transfer coefficients on the blade tip for double squealer tip configuration with three different cavity recesses. For simplicity, the simulation results were presented using two sets of contour levels which is identical to that used in the tip and suction side measurements. Both the experiment and simulation show high heat transfer coefficients on the

squealer rims due to flow acceleration on the top of the rims. On the bottom of the squealer cavity, the heat transfer coefficient is significantly lower due to the low speed separation inside the squealer cavity. In general, the heat transfer coefficient inside the squealer cavity reduces as the cavity depth increases. This can be attributed to the increase of flow recirculation zone and the reduction of the tip leakage flow rate for deeper cavity cases as shown in Figure 3.6.

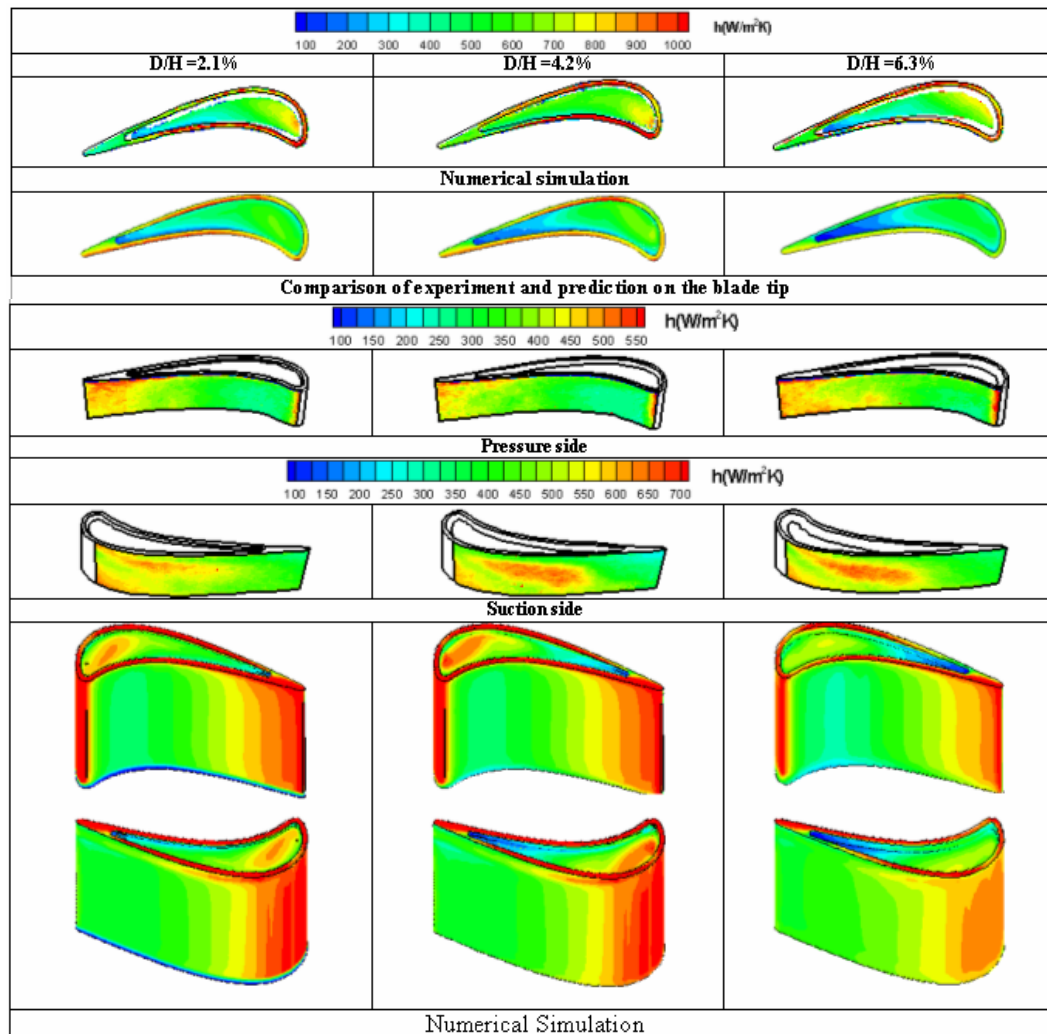


Figure 3.7 Comparison of heat transfer coefficient of double squealer tip between experimental data and numerical predictions.

On the pressure side of the near tip region, the numerical simulations predicted similar heat transfer pattern as those observed in the experiment. However, the predicted level of heat transfer coefficients on the pressure side is about 25% higher than the corresponding measurements, and shares the same level as

suction side. Note that there is no experimental data around the leading edge due to the limitation on the view angle of the camera. Both the numerical and experimental results show that the heat transfer coefficient is higher near the trailing edge in comparison with that observed near the mid-chord region. Also, the heat transfer coefficient around the blade tip is higher than that far below the blade tip.

On the suction side of the near tip region, the predicted heat transfer level is similar to the measured value. Both the experiments and simulations show a high heat transfer coefficient region along the suction side blade tip. The high heat transfer coefficient in this region is clearly caused by the tip leakage vortices shown earlier in Figures 3.4 and 3.6. However, the numerical simulations predicted somewhat smaller tip leakage vortices which did not extend as far downward as those observed in the corresponding experiments. It is also noted that the heat transfer coefficients on the blade suction side is lower for the deepest cavity in comparison with other shallower cavity cases. This decrease of heat transfer coefficients with increasing cavity depth can be attributed to the reduction of tip leakage vortex strength in deeper cavities as seen in Figure 3.6.

Figure 3.8 shows the measured and predicted heat transfer coefficients for the single suction-side squealer tip configuration. It is seen that the heat transfer coefficient is high near the pressure side edge of the blade tip, but decreases gradually along the flow direction toward the suction side squealer rim. The lowest heat transfer coefficient is observed in the stagnation flow region near the root of the squealer rim due to the deceleration of leakage flow along the junction of the squealer rim and blade tip surface. Both the measurements and calculations indicate that the heat transfer coefficient on the blade tip decreases as the cavity depth was increased from 2.1% to 6.3%. This can clearly be attributed to the reduction of tip leakage flow with increasing cavity depth as shown earlier in Figure 3.6. On the other hand, the heat transfer coefficient on the blade suction side is fairly insensitive to the change in cavity depth. In general, the numerical simulations predicted similar level of heat transfer on the blade tip and suction side as was also the observation in the experimental data. However, the heat transfer coefficient on the pressure side is over-predicted.

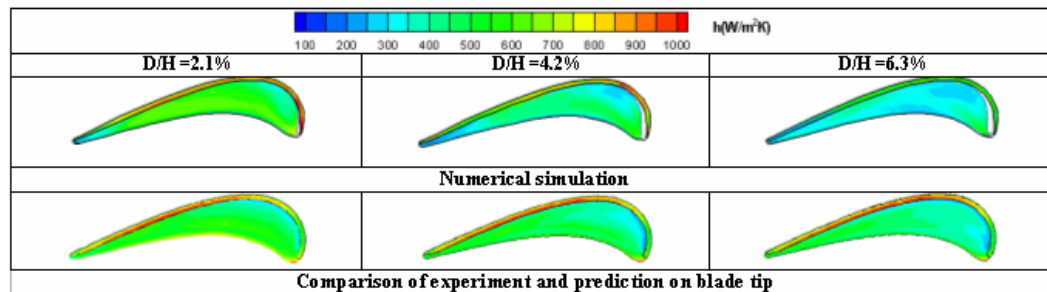


Figure 3.8 Comparison of heat transfer coefficient of single suction side squealer tip between experimental data and numerical predictions.

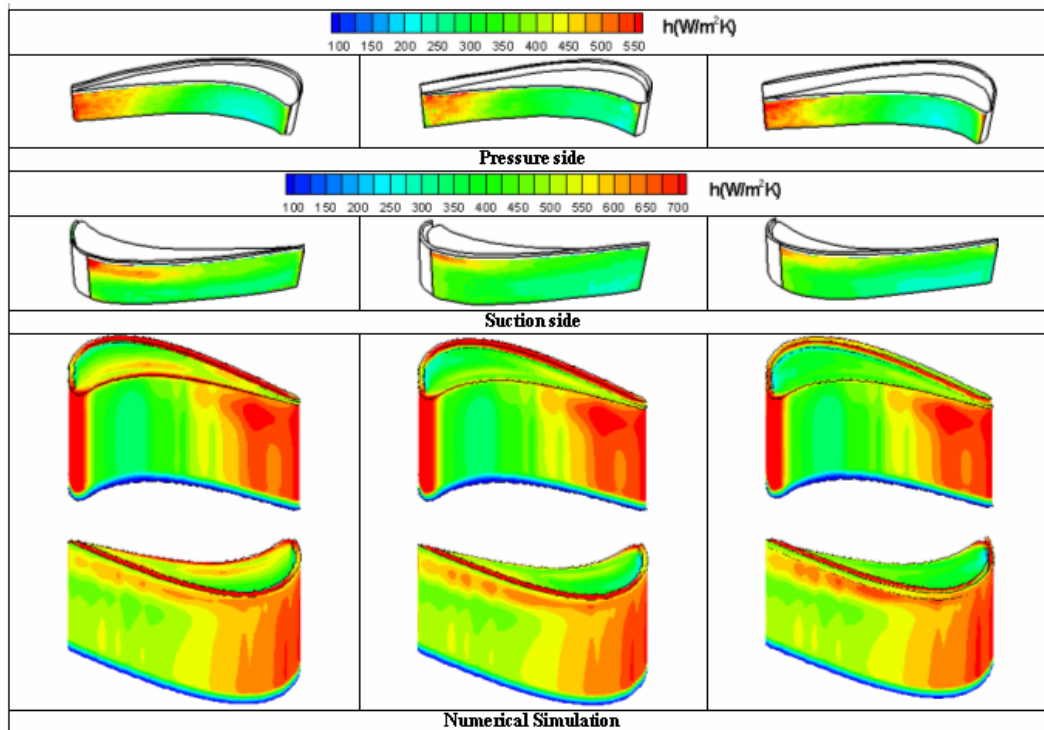


Figure 3.8 Continued

Figure 3.9 shows a comparison of Stanton (St) number distributions on the rotor blade surface for various blade tip configurations under both the non-rotating and rotating conditions. It should be noted that the inflow velocity (183 m/s) and density (3.8 kg/m^3) for the high parameter cases are about 2.12 and 2.60 times of the corresponding velocity (86.27 m/s) and density (1.46 kg/m^3) for the low parameter cases. This implies that the actual heat transfer coefficient for the high parameter case will be 5.5 times of that of the low parameter case if the Stanton number is the same for both cases. It should also be remarked here that the Stanton number distributions for the low parameter cases are simply the dimensionless form of the heat transfer coefficient distributions shown earlier in Figures 3.7 and 3.8. Therefore, we will focus on the effects of high parameter (i.e., high total temperature and high pressure ratio) and rotation in this section. For all three blade tip configurations, it is clearly seen that the Stanton number for the high parameter cases are considerably lower than those observed for the low parameter cases. However, the actual heat transfer coefficient is significantly higher for the high parameter cases since the reference heat transfer coefficient ($\rho_{in} C_p V_{in}$) for high parameter cases is about 5.5 times of that of the low parameter cases.

As noted earlier, the effect of rotation tends to increase the tip leakage flow and push the location of maximum leakage flow towards the trailing edge. However, the tip leakage flow is still dominated by the pressure gradients across the blade tip gap for all three different blade tip configurations considered in the present study. Consequently, the overall heat transfer pattern and the average level of the Stanton number

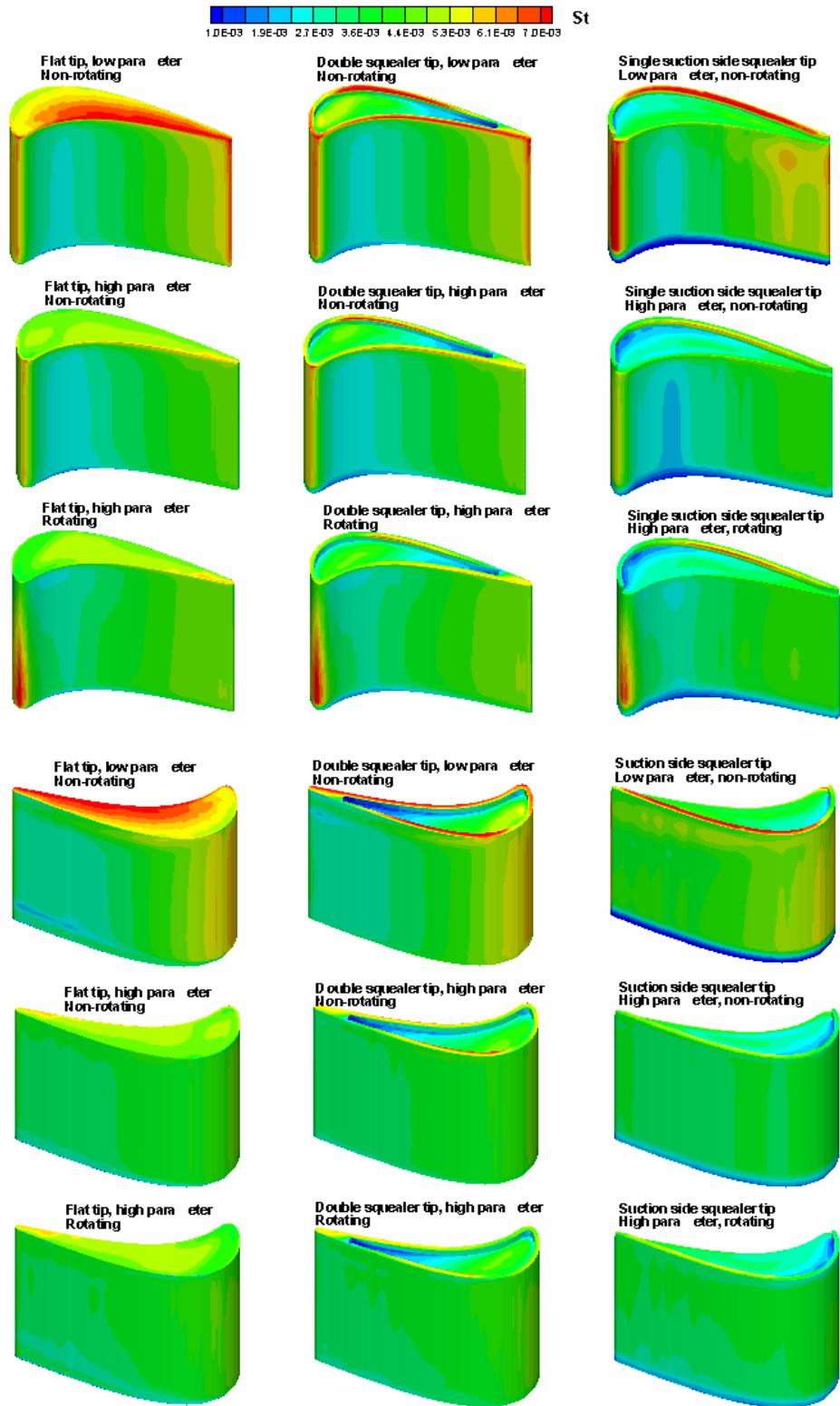


Figure 3. 9 Comparison of Stanton number on the blade surface for various blade tip configurations.

for the rotating and non-rotating cases are quite similar even though the local Stanton number distributions are affected by the blade rotation. As mentioned earlier, Ameri et al.¹ also studied the blade tip heat transfer on the rotating GE-E³ blade with flat and double squealer tips using slightly different boundary conditions and rotating speed. They used the exact GE-E³ blade geometry with three-dimensional twisted blade sections, which is different from the 3 times scaled up blade with two-dimensional GE-E³ tip profile considered in the present study. In general, the Stanton number distributions in the tip region of the present two-dimensional blade are in reasonable agreement with those obtained by Ameri et al.¹ for the exact GE-E³ blade. It is worthwhile to note that the present simulations predicted a higher Stanton number on the squealer rim than the cavity flow, which is consistent with the experimental data of Kwak et al.[13].

For the non-rotating cases, the Stanton numbers are nearly two-dimensional except near the blade root and tip regions where the heat transfer coefficients are affected by the horseshoe vortex and blade tip leakage vortex, respectively. Under the rotating conditions, however, the Stanton number distributions on both the pressure and suction sides of the blade become three-dimensional due to the migration of blade passage vortex under the action of centrifugal and Coriolis forces. The Stanton number increases significantly at the blade leading edge and on the pressure side around the blade-hub junction. On the blade suction side, the Stanton number increases near the blade tip region, but reduces significantly along the blade-hub junction towards the trailing edge. It is quite clear that the rotation-induced centrifugal and Coriolis forces significantly changed the horseshoe vortex along the blade-hub junction as well as the blade tip leakage flow.

Figure 3.10 shows the Stanton number distributions on the stationary shroud surface for both the non-rotating and rotating cases. For all three different blade tip configurations, the Stanton number is found to increase dramatically under rotating conditions. The high heat transfer coefficients on the stationary shroud can be attributed to the sharp increase of velocity and temperature gradients in the shroud boundary layer. In addition to the blade tip and shroud heat transfers, it is also worthwhile to examine the predicted heat transfer coefficients around the blade root and hub junction for high parameter non-rotating and rotating cases as shown in Figure 3.11. Along the blade-hub junction, the flow is highly three-dimensional due to the presence of horseshoe vortices in the corner region. In general, the swirling motion of the horseshoe vortex produces higher velocity and temperature gradients and increases the heat transfer coefficients along the blade-hub junction. For the rotating case, the size of the horseshoe vortex on the pressure side is significantly reduced. On the suction side, a low heat transfer strip is extended from the leading edge of the blade-hub junction towards the trailing edge as a result of the passage vortex migration under the rotating conditions.

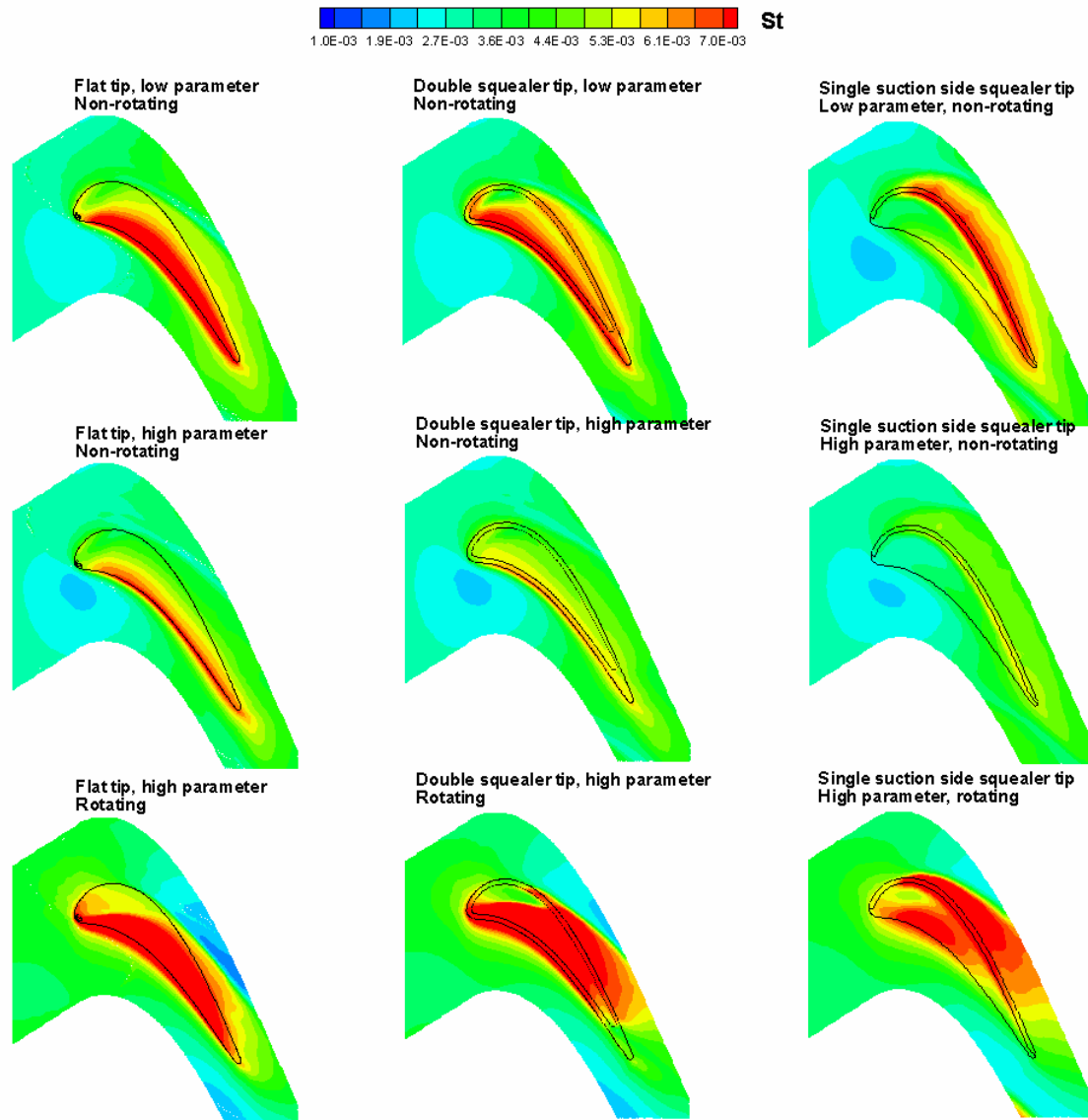


Figure 3.10 Comparison of the Stanton number on the shroud for various blade tip configurations.

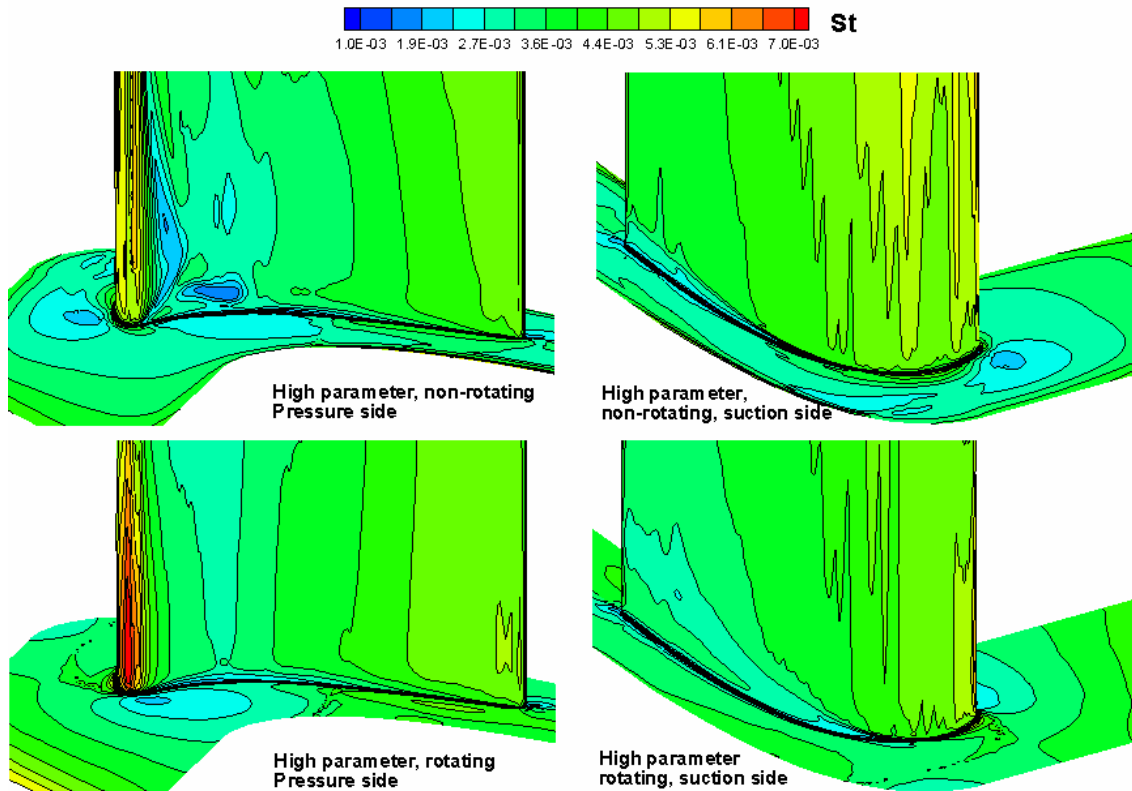


Figure 3.11 Comparison of Stanton number on the hub and root of blade.

3.2.3 Heat Load of the Various Blade Tips

In order to evaluate the performance of various blade tip configurations for heat load reduction, it is desirable to compare the total heat flux $Q = h \times A \times \Delta T$ for each case. Under the same temperature difference (which is reasonable assumption for the large amount of tip leakage flow), the heat load rate can be defined as $h \times A$ where A is the total surface area of the blade tip region including the cavity wall as shown in Figure 3.12 marked by bold line.

Figure 3.13 (a) shows the area averaged heat transfer coefficients for various tip configurations under low parameter condition. It is clearly seen that the squealer tip configurations is quite effective in reducing the heat transfer coefficients. It should also be noted that the area averaged heat transfer coefficients decreases with increasing squealer cavity depth for both the double squealer and single suction-side squealer tips. In general, the double squealer tip is more effective than the single suction-side

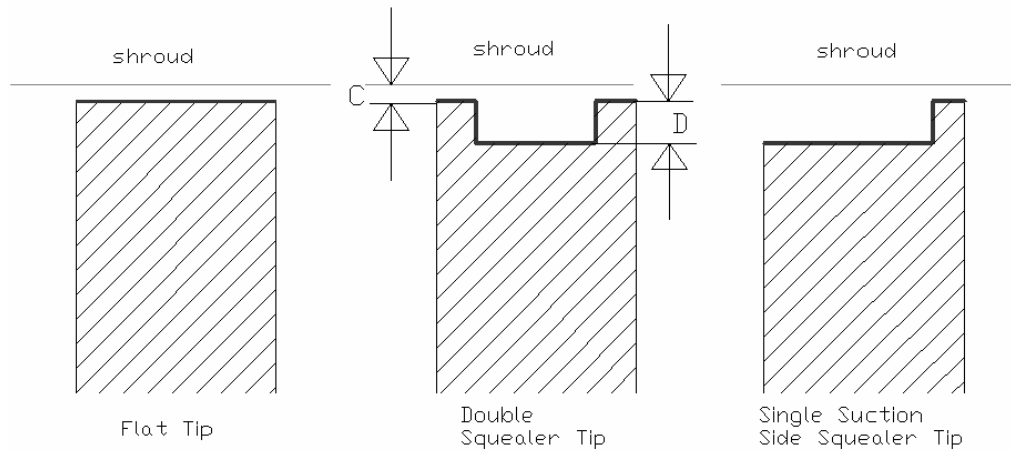
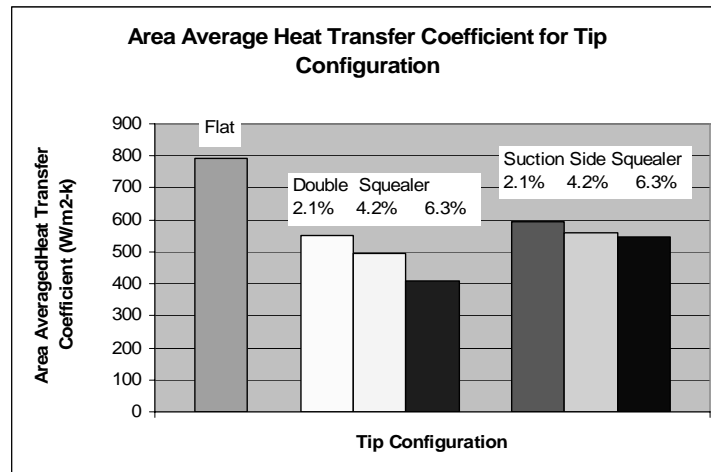


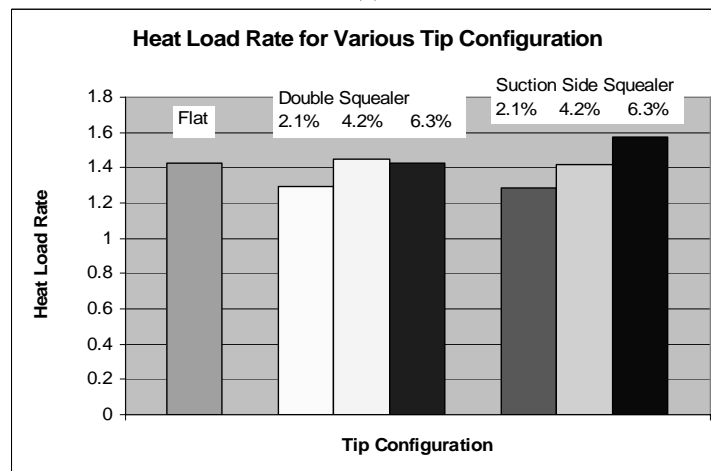
Figure 3.12 Heat transfer surface area of various tip configurations.

squealer tip in terms of the reduction of area averaged heat transfer coefficients. However, the surface area of the double squealer tip configuration is also considerably larger than the other two configurations as seen in Figure 3.12. In order to obtain a more meaningful comparison of the heat transfer characteristics, it is desirable to compare the total heat flux or the heat load rate for various blade tip configurations as shown in Figure 3.13(b). Comparing to the flat tip case, the shallow cavity with 2.1% cavity depth was found to be most effective for both the double and single suction-side squealer configurations. For deeper cavity depths, the reduction in heat transfer coefficient is completely offset by the increase of the blade tip surface area with very little additional benefit in the heat load reduction.

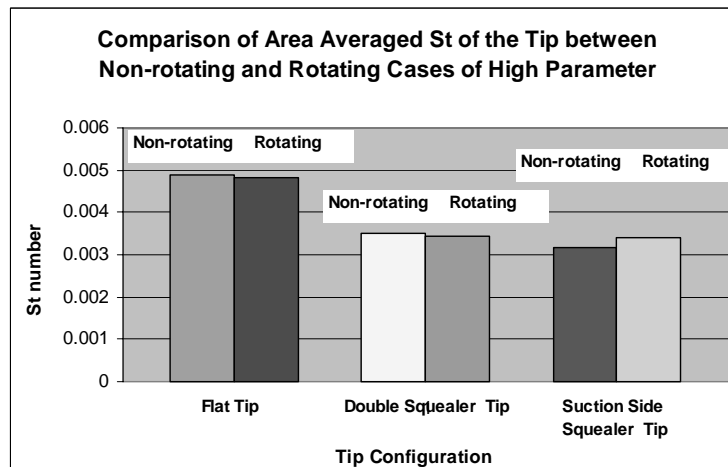
For completeness, the area averaged Stanton number for high parameter cases with 4.2% cavity depth are also shown in Figure 3.13(c) for various blade tip configurations under non-rotating and rotating conditions. As noted earlier, the rotation-induced centrifugal buoyancy and Coriolis forces significantly changed the blade tip leakage flow and local heat transfer coefficient distributions. However, the area averaged Stanton numbers shown in Figure 3.13(c) are only slightly affected by the blade rotation for the three different blade tip configurations considered in the present study. This suggests that the primary influence of the blade rotation is to redistribute the blade tip leakage flow and local heat transfer coefficients. Since the overall heat load is relatively insensitive to the effects of the blade rotation, it is possible to obtain the area average heat transfer coefficients for real engine conditions (with 1.5% tip clearance) based on non-rotating experiments at the same high parameter operation conditions.



(a)



(b)



(c)

Figure 3.13 Comparison of averaged heat transfer coefficient, heat load rate and Stanton number for various blade tip configurations.

3.3. Conclusions of Blade Tip Leakage Flow and Heat Transfer

Numerical simulations of flow and heat transfer were performed for three different blade tip configurations including a flat tip, a double squealer tip, and a single suction-side squealer tip. Major conclusions are listed below:

- 1) The predicted heat transfer coefficients on the blade tip and suction side compared reasonably well with the experimental data but the heat transfer coefficients in the near tip region of pressure side were overpredicted.
- 2) Both the experimental and numerical results show that the single suction side squealer tip is the best configuration to reduce the tip leakage flow and lower the heat transfer coefficient on the squealer cavity floor on the blade tip.
- 3) For both the double squealer tip and single suction-side squealer tip, the heat transfer coefficient on the cavity floor also decreases with increasing cavity depth. However, the heat load rate was found to increase with increasing cavity depth since the available heat transfer area increases at a faster rate than the reduction in heat transfer coefficient. Therefore, it is desirable to use the tip configuration with shallow squealer cavity to reduce the overall heat load.
- 4) For the 1.5% tip clearance cases considered here, the area averaged Stanton number and the heat load rate are only slightly affected by the blade rotation. However, the heat transfer coefficient on the stationary shroud is significantly higher under the rotating conditions due to dramatic increases of the velocity and temperature gradients in the shroud boundary layer. The heat transfer coefficients on the pressure and suction sides of the blade are also significantly changed due to the passage vortex migration induced by the blade rotation.

CHAPTER IV

BLADE TIP FILM COOLING

4.1. Arrangements of Film Holes on Blade Tip

For the gas turbine external heat load, the film cooling is one of the most widely used techniques to protect the hot surface by the coolant layer to separate the solid wall from the hot gas. Bogard and Thole [58] have summarized the most recent development of gas turbine film cooling. The chapter III has discussed the leakage flow and heat transfer on the blade tips with various configurations, this chapter focuses on the optimization of film-hole arrangements on both the plane and squealer tips of the GE-E³ blade using the Fluent CFD code with Reynolds stress turbulence model and non-equilibrium wall function. Detailed validations of the present numerical method and turbulence model for blade tip leakage flow were presented in Yang et al.[7-8]. In general, the predicted heat transfer coefficients are in good agreement with the experimental data of Azad et al.[9-10] and Kwak and Han [14-15]. For the film cooling effectiveness on the blade tip, however, no direct comparisons of the simulation results with the experiment have been reported in the open literature so far. In this paper, numerical simulations are performed and compared with the experimental data obtained using pressure sensitive paint (PSP) technique by Ahn et al.[22]. The previous studies by Yang et al.[7-8] showed that the Reynolds stress turbulence model provides somewhat more accurate resolution of the complex flow inside the squealer cavity. Therefore, this Reynolds stress model is used together with the non-equilibrium wall function for the near wall region. There were only a few studies addressing film cooling and the associated heat transfer coefficient on blade tips, and the effects of film-hole locations and blade rotation have not been systematically studied. Therefore, the work presented here is unique to the literature.

The original design of the holes on the blade tip is used to purge dirt from the coolant by centrifugal force, such that these dirt particles will not block the small diameter film holes. Most often, these holes are arranged on the mid camber line of the tips due to manufacturing reasons. However, this simple camber line film-hole arrangement may not yield a good design for blade tip film cooling applications since the film cooling jets do not provide adequate coverage for the high heat transfer regions on either the plane or squealer blade tips. For example, Figure 4.1 shows the measured film cooling effectiveness and heat transfer coefficients for the camber line film-hole arrangements on plane and squealer tips as tested by Kwak and Han[18-19]. For the plane tip case, the high heat transfer region was observed on the pressure side of the blade tip. However, the film coolant jets were bent toward the suction portion of the blade tip and did not provide good protection on the pressure side high heat transfer region. For the squealer tip case, the high heat transfer region is located near the leading edge and along the suction side of the squealer cavity floor. However, the coolant jet was pushed toward the pressure side of the cavity with poor

protection on the suction side high heat transfer region. In both the plane and squealer tips, the film coolant covers only one half of the blade tip downstream path of the film coolant jets. The portion upstream path of the film-holes does not benefit from the film cooling.

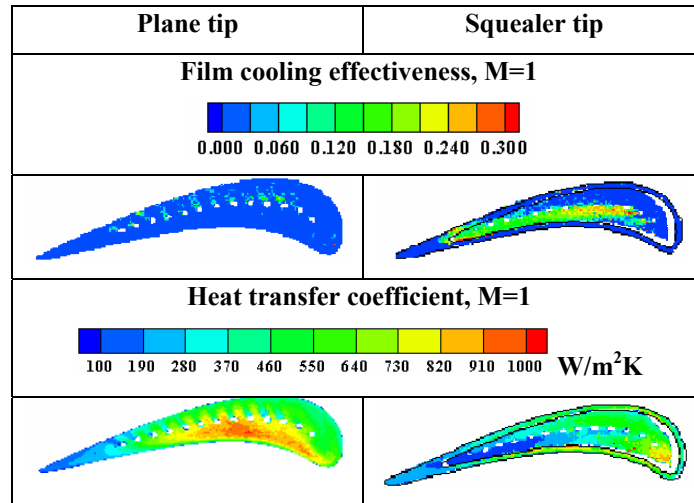


Figure 4.1 Film cooling effectiveness and heat transfer coefficient distribution of camber arrangement on the plane and squealer tips, Kwak and Han[18-19].

To compare film cooling performance on the blade tip, three different film-hole arrangements were investigated in the present study as shown in Figure 4.2. Figure 4.2(a)-(b) for the plane and squealer tips, denoted as camber arrangement, serve as a baseline for comparison. These film hole geometry and camber arrangement are identical to the experimental geometry reported by Ahn et al.[22]. The locations of the film holes shown in Figure 4.2(c)-(d) were selected based on the implication of the film cooling and heat transfer results presented in Figure 4.1 by Kwak and Han [18-19], and the blade tip leakage flow patterns obtained from previous numerical studies by Yang et al.[7-8]. For example, Figure 4.3 shows the predicted pathlines of tip leakage flow for both the plane and squealer blade tips. For the plane tip in Figure 4.3(a), the tip leakage flow is driven by the pressure gradients from the pressure side to the suction side and the high heat transfer region is located near the pressure side on the blade tip. The predicted tip leakage flow pathlines explained fairly well on the local heat transfer data presented by Azad et al. [9-10] and Kwak and Han [14]. An effective way to improve the film cooling effectiveness is to locate the film holes on the plane tip near the pressure side to provide more coverage of the blade tip region, as shown in Figure 4.2(c). For the squealer tip, the leakage flow is much more complex compared to the plane tip case, especially inside the squealer cavity. The computed pathlines in Figure 4.3(b) show that the squealer tip leakage flow moves over the squealer rim on the pressure side, rolls down inside the cavity, then rolls up again to leave the cavity over the suction side of the squealer rim near the trailing edge. Consequently, a

high heat transfer region was observed along the suction side of the squealer cavity. In addition, another high heat transfer region was dictated near the leading edge inside the squealer cavity due to the reattachment of the blade tip leakage flow. This leakage flow pattern also provides a good explanation of the local heat transfer data presented by Azad et al.[9] and Kwak and Han[14] for the squealer tip configuration. Based on the above observations for squealer tip leakage flow and heat transfer coefficient distributions, it is proposed to place three film holes near the leading edge of the blade tip inside the cavity to provide better protection for the high heat transfer region around the blade leading edge. And the other four holes are located near the suction side to provide better film cooling coverage for the other high heat transfer region along the suction side of the blade tip, as shown in Figure 4.2(d). The above two film hole arrangements for the plane and squealer tips are denoted as upstream arrangements as shown in Figure 4.2(c)-2(d) since the film holes were placed strategically on the upstream of the tip leakage flow and the high heat transfer areas.

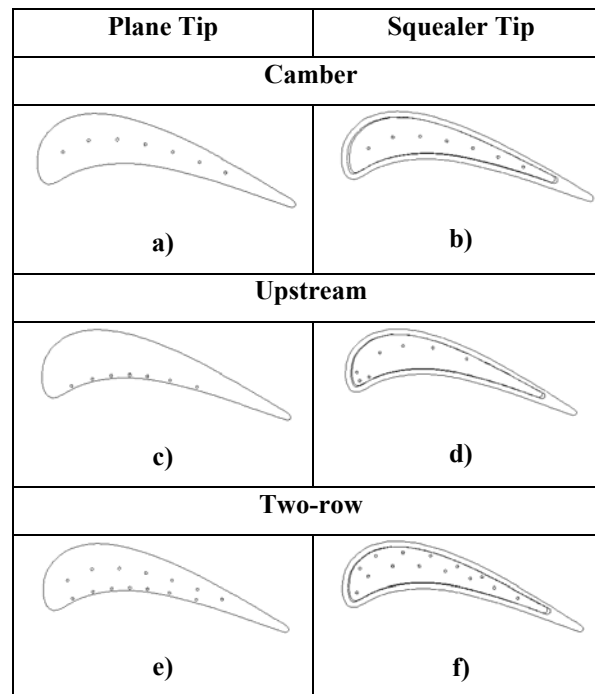


Figure 4.2 Various film hole arrangements on the plane and squealer tips.

In addition, it is desirable to investigate whether one row or two rows of film holes will provide better film cooling for the same amount of given coolant flow rate. In the present study, two different kinds of two-row film hole arrangements were investigated for the plane and squealer tips, respectively. For the plane tip case, one row of seven film holes was located on the camber line while another row of seven holes was placed near the pressure side as shown in Figure 4.2(e). This is essentially a combination of the

camber line and upstream arrangements to provide better film cooling coverage for the entire blade tip. A different two-row arrangement was proposed for the squealer tip case as shown in Figure 4.2(f). In this arrangement, one row with seven film holes was located along the suction side of the squealer cavity upstream of the leakage flow inside the cavity while the other row of seven holes was placed along the camber line. In order to provide a fair comparison of the film cooling effectiveness, the total amount of coolant is maintained the same for all film hole arrangements considered in the present study. This implies that the averaged local blowing ratio for the two-row configurations is only one-half of those considered in the camber and upstream film hole configurations.

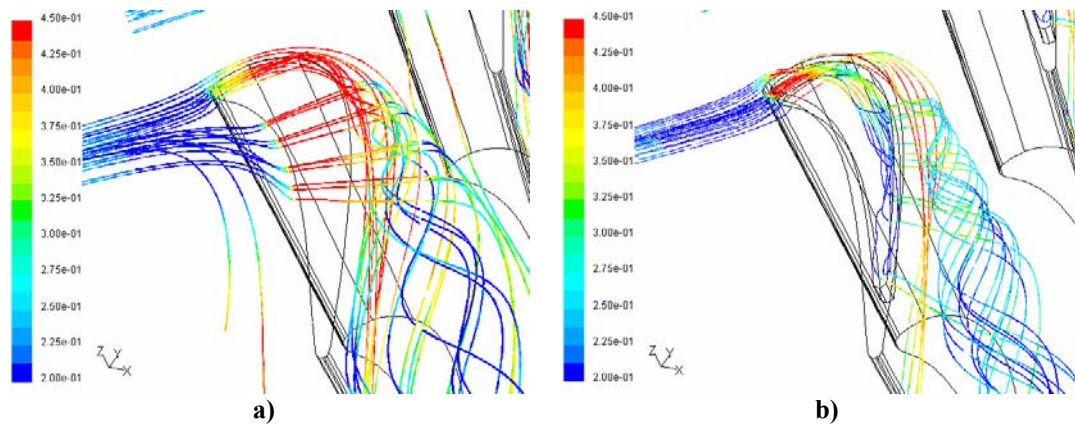


Figure 4.3 Comparison of tip leakage flow pathlines (colored by Mach number) between plane tip (a, Yang et al. [7]) and squealer tip (b, Yang et al.[8]) configurations.

4.2. Computational Details

The simulations were performed using the CFD software Fluent [53] (Version 6). The solutions were obtained by solving the compressible Reynolds-Averaged Navier-Stokes (RANS) equations using a finite volume method to discretize the continuity, momentum and energy equations. The GAMBIT software was used to generate the unstructured hexahedron grids, with fine grid clustering inside the blade boundary layer and the blade tip region. Figure 4.4(a) shows a typical film cooled squealer tip blade with selected cross sectional planes which will be used later to show the secondary flow structures around the blade tip region. Unlike the earlier study of Acharya et al.[20] which used long cylindrical tubes to represent the film holes, a coolant plenum and two coolant passages are included in the present simulations to provide a more realistic representation of the blade tip film cooling configuration.

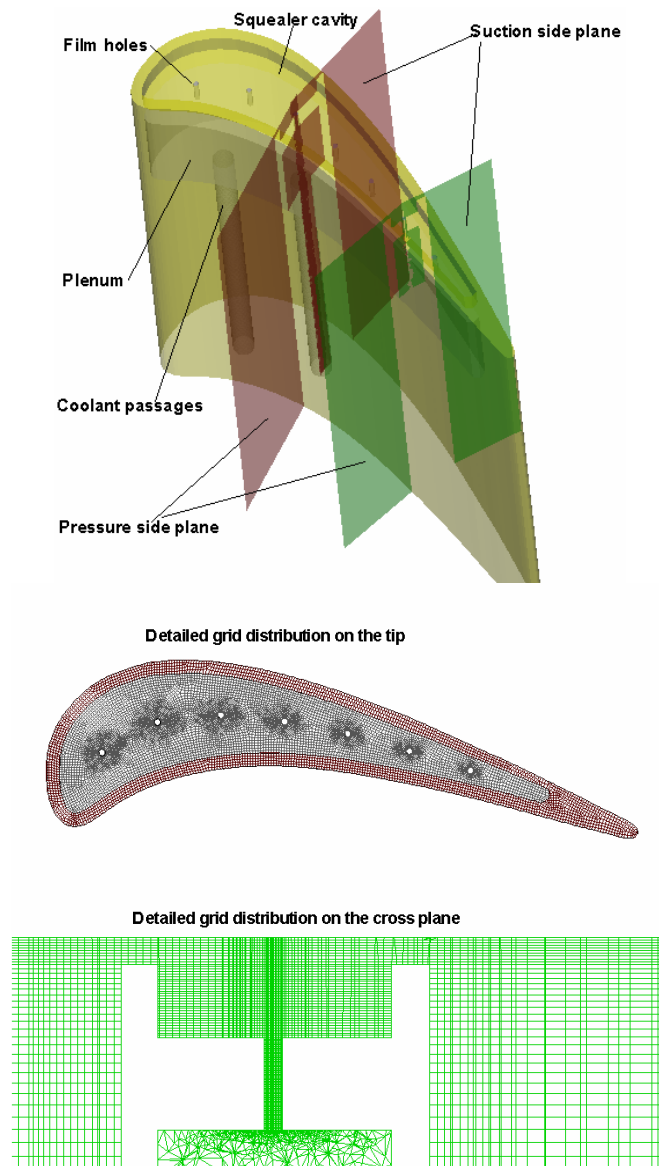


Figure 4.4 Geometry and numerical grids: (top) Schematic of typical film cooled GE-E³ blade with squealer tip and selected cross sections, and (bottom) detailed grid distribution of the film cooled squealer tip and film hole.

Relatively coarse grids are used inside the coolant passages and the plenum, while the film-holes and squealer tip regions are covered with much finer grids for accurate resolution of the film cooling jets and tip leakage flows. The value of $y^* (= C_{\mu}^{1/4} k_p^{1/2} y_p / \nu)$ for the non-equilibrium wall function falls between 25 and 100 for most of the blade tip region, where k is the turbulent kinetic energy and the subscript p denotes the near-wall grid point. The geometry and detailed numerical grids around a typical film cooled

squealer tip is shown in Figure 4.4(b). Similar grid structures were used for the other film hole arrangements.

The present calculations were carried out for a three times scaled up model of the GE-E³ blade. This blade configuration is identical to that used in the experimental study of Kwak and Han[18-19]. The scaled up blade has an axial chord length of 8.61 cm, and the aspect ratio of the span to the chord is 1.4. The blade leading edge pitch is 9.15 cm, The tip clearance studied here is 1.97 mm, i.e., 1.5% of the blade span. For the squealer tip, the depth of the cavity is 4.6 mm which is 3.77% of the blade span, and the cavity rim width is 2.54 mm. The diameter of the film-holes is 0.127 cm.

The computational domain consists of a single blade with periodic boundary conditions imposed in the circumferential direction. At the inlet, the total temperature (300 K), total pressure (129.96 kPa) and static pressure (124.43 kPa) are specified with an inlet flow angle of 32°. The inlet turbulence intensity is taken as 9.7%. At the exit, the static pressure is specified as 108.3 kPa. All these flow conditions are identical to Kawk and Han [18-19] and Ahn et al.[22] experimental setup. Three global blowing ratios of $M = 0.5, 1.0$ and 2 have been studied with a fixed mass flux boundary conditions. To calculate the film cooling effectiveness, the coolant temperature is taken as 350 K and the turbulence intensity is $Tu = 3\%$, the same as those given in Kwak and Han [18-19], and the adiabatic boundary condition is used on the blade and shroud surfaces. To calculate the heat transfer, a different thermal boundary condition is used with the wall temperature fixed at 350 K and the inlet coolant temperature is maintained the same as the cascade inlet temperature.

For completeness, simulations were also performed for the same 3X scaled up GE-E³ blade using typical operating conditions for a real turbine with a blade tip radius of 35.56 cm (14 inch) under both non-rotating and rotating conditions. This enables us to evaluate the effects of rotation, high temperature, high Mach number, and high cascade inlet/outlet pressure ratio on the film cooling effectiveness and heat transfer in the blade tip region. A rotating speed of 9,600 rpm is used in the present rotating blade simulation. The inlet total temperature is specified at 1,700 K and the coolant temperature is 923 K for the film cooling effectiveness calculation. To calculate the heat transfer coefficient, the coolant temperature is kept the same as the cascade inlet temperature of 1,700 K, while the blade surface temperature is specified at 1,190 K. The inlet turbulence intensity is 9.7%, and the inlet flow angle is 32 degree. The total pressure at the inlet is 1.675 MPa and the static pressure at the exit is 1.03 MPa. This gives an inlet/outlet pressure ratio, $P_{in,t}/P_{out,s}$ of 1.63, which is significantly higher than the 1.2 used in the experiments of Kwak et al.[18-19]. For convenience, the simulations at high total temperature and high inlet/outlet pressure ratio cases are denoted as “high parameter”, while the low inlet/outlet pressure ratio and low total temperature cases corresponding to the experimental conditions are denoted as “low parameter” in the following discussions. For the rotating cases, the whole blade domain is rotating with a relative inlet flow angle equal to 32 degree, while the shroud remains stationary. All other conditions are kept the same as the high

parameter stationary case to facilitate a detailed understanding of the effects of blade rotation under realistic turbine working conditions.

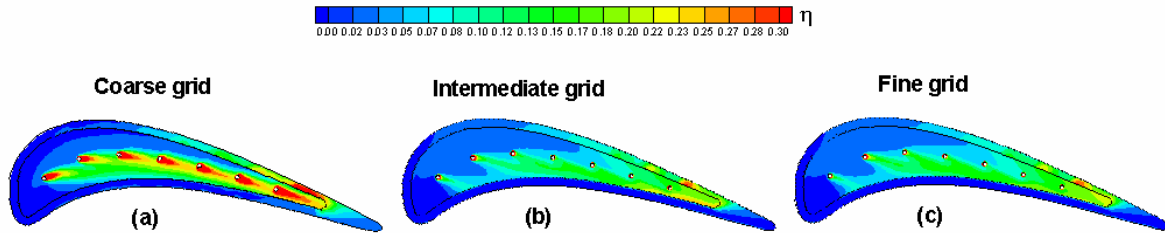


Figure 4.5 Grid refinement study.

All calculations are converged to residual levels of the order of 10^{-5} , and to less than 0.1% error in the mass flow rate between the cascade mainstream flow and film coolant inlet and outlet of the computational domain. Typically, 800 iterations are needed to achieve the desirable convergence. Grid refinement studies have been performed for all cases using at least two different grid densities. Figure 4.5 shows the cooling effectiveness on the squealer tip for three different grids with 0.74, 1.1, and 1.5 million grid points, respectively. The change of the film cooling effectiveness between the intermediate and fine grid solutions is fairly small, indicating that the finest grid solution is nearly grid independent. As shown in Table 4.1, a total of twenty (20) simulations were performed for the non-rotating low parameter cases with various combinations of blade tip geometry, film hole arrangement and blowing ratio. In addition, eight (8) high parameter cases were also investigated for the plane and squealer tip configurations blade tip cooling configurations under non-rotating as well as rotating conditions. A systematic grid refinement study was performed for all cases, but only the finest grid results are presented in this paper.

4.3. Results And Discussion

4.3.1. Distribution of Pressure Ratio

Figure 4.6 shows a comparison of the predicted pressure ratio (P_t/P) distribution for camber line, upstream, and two-row film hole arrangements. Generally speaking, the high pressure ratio means low local static pressure and high velocity. For the plane tip configurations, it is clearly seen that the pressure ratio is relatively low (i.e., low velocity) upstream of the coolant jet, while high pressure ratio were observed downstream of the coolant jet. This indicates that the coolant velocity is slower than the surrounding fluid and acts as an obstacle to the surrounding tip leakage flow. The effect of jet blockage on the tip leakage flow is considerably weaker for the squealer tip due to the large squealer cavity depth. The simulation results show that the pressure ratio on the plane tip is strongly affected by different film hole arrangements. In particular, the upstream arrangement produced a significantly higher pressure ratio than the other two film hole arrangements. On the other hand, the effect of film cooling on the squealer tip is

considerably weaker than that of the plane tip because the cavity depth is much larger than the plane tip clearance. It should also be noted that the computed leakage flow velocity in the tip clearance is significantly higher than the cascade average velocity for both the plane and squealer tip configurations since the leakage flow is driven by strong pressure gradients across the tip clearance.

Table 4.1 Matrix of numerical simulations.

			Plane tip			Squealer tip		
			camber	upstream	2 rows	camber	upstream	2 rows
Approximate grid number (million)			0.9	1	1.3	1.5	1.6	1.7
Film cooling effectiveness	Low parameter, non-rotating	M=0.5	X	X	X	X	X	X
		M=1	X	X	X	X	X	X
		M=2	X	X	X	X	X	X
	High parameter, non-rotating	M=1	X			X		
	High parameter, rotating	M=1	X			X		
Heat transfer coefficient	Low parameter, non-rotating	M=1	X			X		
	High parameter, non-rotating	M=1	X			X		
	High parameter, rotating	M=1	X			X		

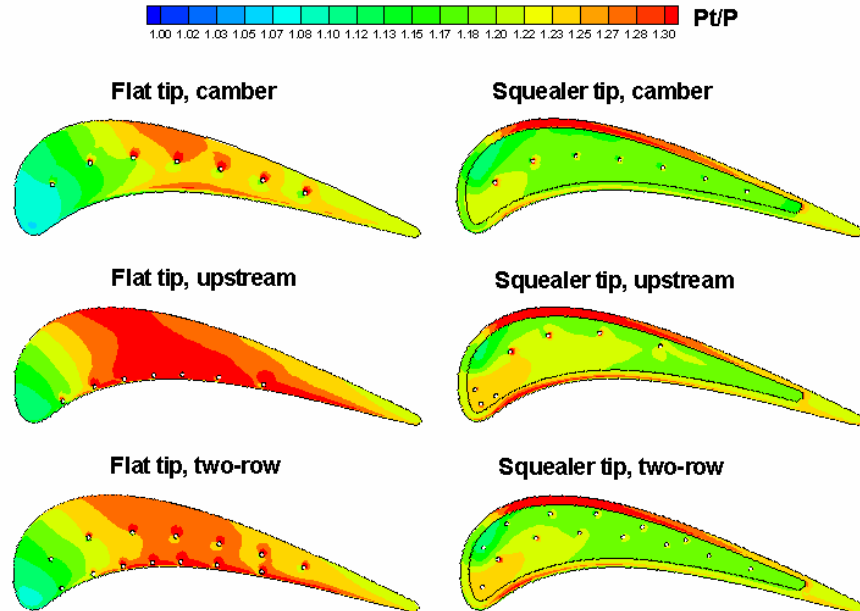


Figure 4.6 Comparison of the pressure ratio (P_t/P) distributions on the plane and squealer tips among various film hole arrangements with low parameter; $M = 1$ for camber and upstream configurations, $M=0.5$ for two-row configuration.

Figure 4.7 compares the computed pressure ratio contours with the PSP data of Ahn et al.[22] on the shrouds for the blowing ratio $M = 1$ cases. In general, the predicted trends of pressure ratio match well with the corresponding measurement. The highest pressure ratio value measured by the PSP is about 1.25 in the plane tip region, while the predicted maximum pressure ratio is slightly higher at 1.3. For the squealer tips, the highest pressure ratio above the cavity is about 1.19, while the predicted value is about 1.2 at the same location. Experimental PSP data shows that the effect of film cooling is negligible on the shroud, while the simulations indicated the presence of strong film cooling effects on the shroud for the plane tip cases. Both the experiments and simulations show that the squealer tips reduce the tip leakage flow velocity significantly due to flow separation and recirculation in the squealer cavity, Since the plane tip clearance is much smaller than the depth of the squealer cavity, the effect of plane tip film cooling on the shroud is stronger than that observed for the squealer tip cases. In addition, the tip leakage vortex is affected by different film hole arrangements, especially for the plane tip due to the small tip gap. Note that the trajectory of the tip leakage vortex can be traced by the shape of the pressure ratio contours near the blade suction side of the shroud surface, which is dictated by both experiment and numerical simulations.

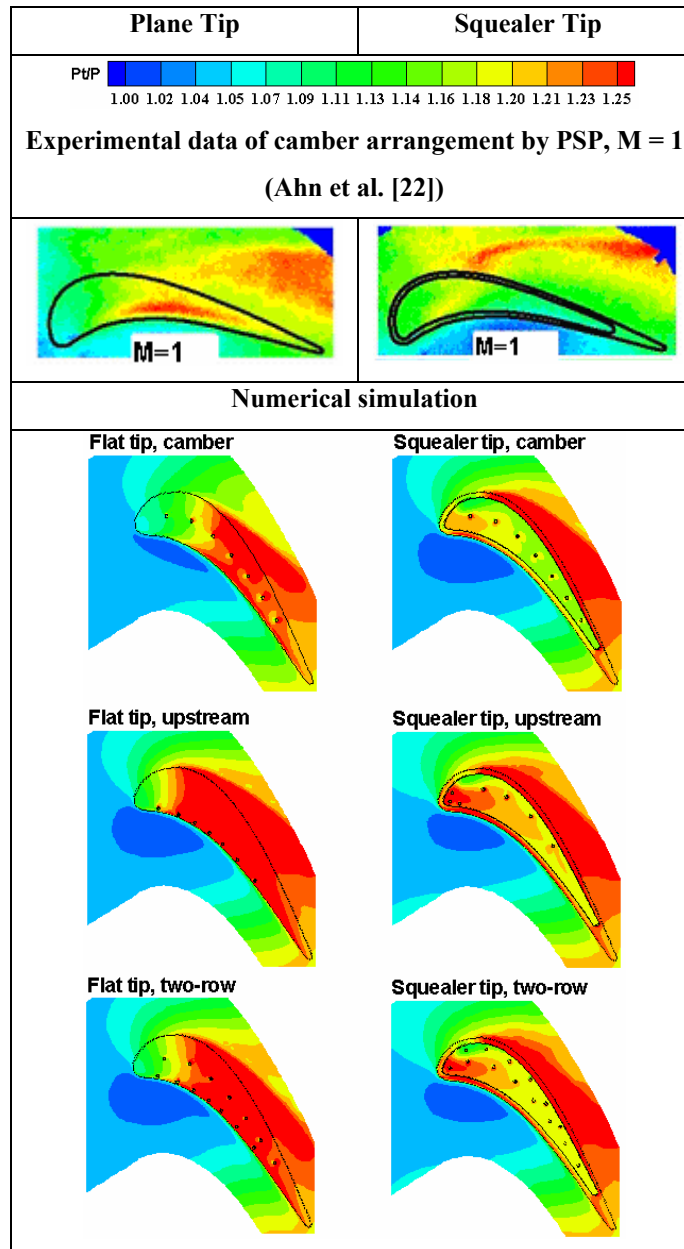


Figure 4.7 Comparison of pressure ratio (P_t/P_0) distributions on the shrouds among various blade tip configurations and film hole arrangements with low parameter; M=1 for camber and upstream configurations, M=0.5 for two-row configuration.

4.3.2. The Film Coolant Pathlines

The film coolant pathlines colored by the dimensionless temperature (ϕ) are depicted in Figure 4.8 for various film hole arrangements with a blowing ratio M=1. For the plane tips, the camber arrangement shows the coolant rolls around inside the plenum before exiting from the film holes located on the middle

camber line of the blade tip. The coolant then mixes with the tip leakage flow by exchanging momentum and energy, travels across the suction side portion of the blade tip, and rolls away from the suction side of the tip to form a leakage vortex in the cascade passage. On the other hand, the coolant jets in the upstream film hole arrangement travel across the entire blade tip width before roll down the suction side. It is quite clear that the upstream film hole arrangement is able to provide complete coverage of the entire blade tip from the pressure side to the suction side. The two-row arrangement is a combination of the camber and upstream arrangements which splits the same amount of coolant into two parts. Some coolant was delivered from the film holes near the pressure side to cover the whole width of the blade tip, while the others were delivered from the middle camber line to cover only the suction side portion of the blade tip.

For the squealer tip cases, the coolant flow structures are more complex in comparison with the plane tip cases. For the camber arrangement, the coolant rolls around inside the plenum similar to those observed earlier for the plane tip case. The coolant then exits from the film holes at the bottom of the cavity, and mixed with the tip leakage flows inside the squealer cavity. Some coolant near the trailing edge portion rolls away from the suction rim directly, the remaining coolant travels downstream along the trailing direction and leaves the squealer tip to form a leakage vortex in the cascade passage. The upstream film-hole arrangement shows that more coolant are trapped in the leading edge portion of the squealer cavity, and the coolant jets in the trailing edge region tend to cover a wider area of the blade tip and provide a better overall film cooling effectiveness in comparison with the camber arrangement. For the two rows film-hole arrangement, the pathlines are basically a combination of those generated by the camber and upstream arrangements with more balanced coverage between the leading edge and trailing edge portions of the blade tip.

It should also be noted that the coolant jet pathlines for all three different film-hole arrangements roll away from the blade tip without touching the blade suction side when forming the leakage vortex in the cascade passage. This implies that film coolant jets protect only the blade tip and shroud regions, while the suction side of the blade surface below the blade tip does not benefit from the film cooling in these studies.

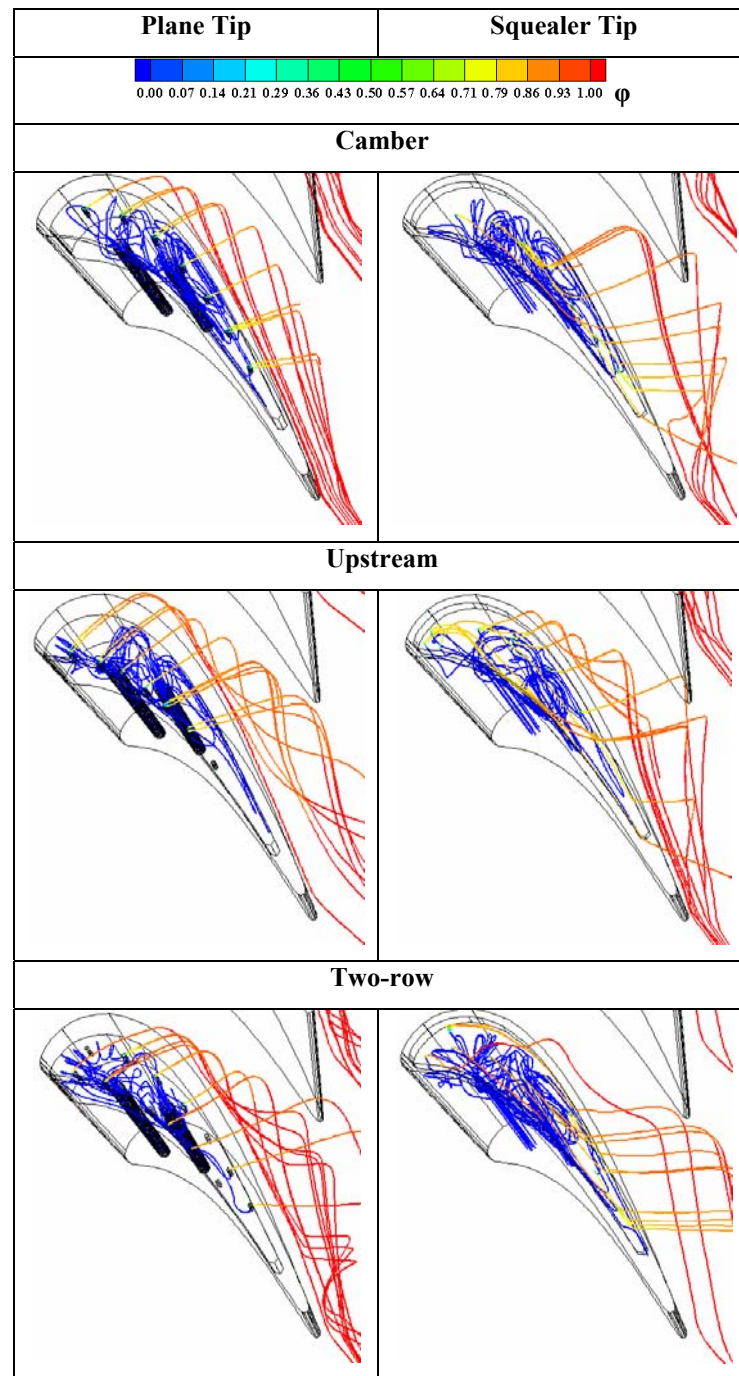


Figure 4.8 Comparison of film coolant pathlines (colored by dimensionless temperature ϕ) among various film hole arrangements with low parameter; $M = 1$ for camber and upstream configurations, $M=0.5$ for two-row configuration.

4.3.3. Film Cooling Effectiveness

Figure 4.9 compares the calculated film cooling effectiveness on the plane and squealer tips for different tip configurations with the measured PSP data of Ahn et al.[22]. In general, the numerical results tend to overpredict the film cooling effectiveness, especially for the squealer tip, but the effectiveness patterns match fairly well with the PSP data for both the plane and squealer tip cases. For camber arrangement, the area protected by the film cooling begins from the camber line towards the suction side edge on the plane tip. On the squealer tip, however, the film coolant jets move from the camber line toward the pressure side and trailing edges with high film cooling effectiveness on the pressure side downstream of the film holes. In general, the numerical results are closer to the PSP data of Ahn et al.[22] than the transient liquid crystal experimental data of Kwak and Han[18-19] shown in Figure 4.1. It should be noted that there are 13 film holes in the experimental study of Kwak and Han [18-19], while the present film hole configuration is identical to that used by Ahn et al.[22] with only 7 film holes.

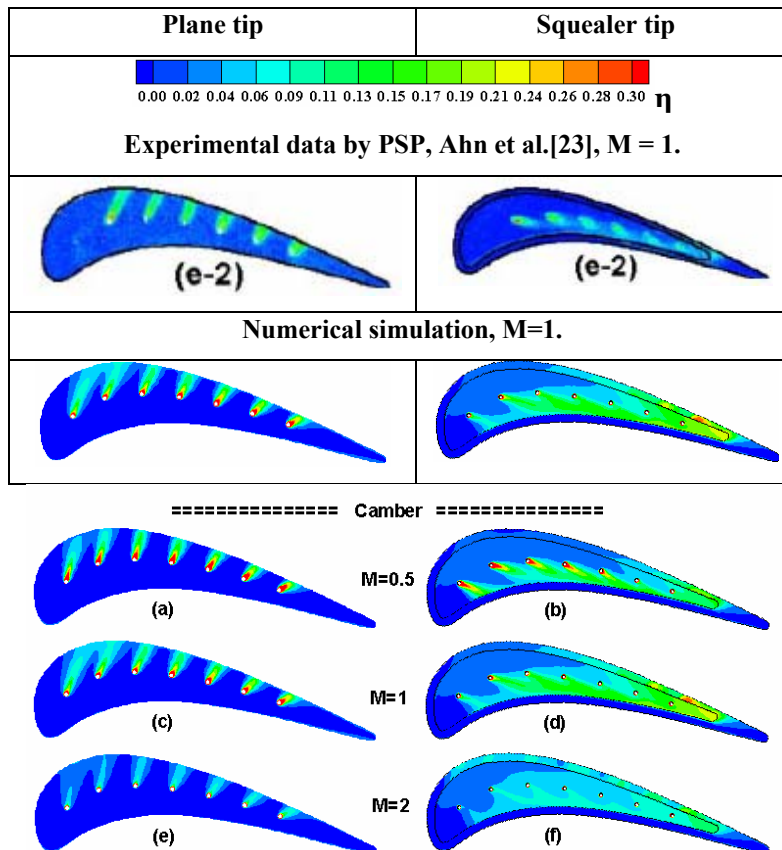


Figure 4.9 Comparison of film cooling effectiveness on plane and squealer tips with various film hole arrangements and blowing ratios, low parameter.

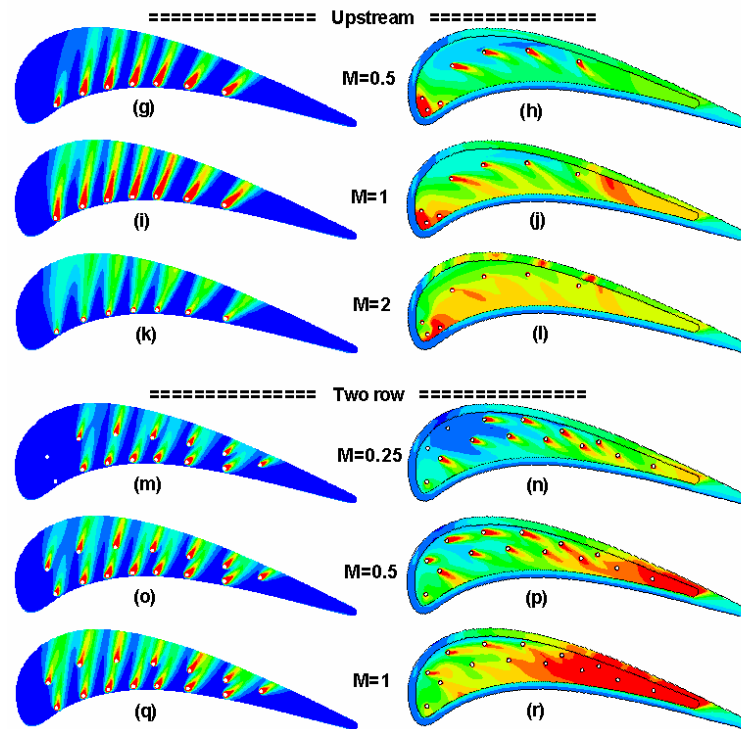


Figure 4.9 Continued.

For completeness, the predicted film cooling effectiveness on the plane and squealer tips with different film hole arrangements and three blowing ratios of $M = 0.5, 1$ and 2 ($M=0.25, 0.5$ and 1 , respectively, for two-row configurations) are also shown in the lower part of Figure 4.9. For plane tips, the patterns of film cooling effectiveness match the trajectories of the tip leakage flow, developing from the pressure side edge and ending at the suction side edge. It can be clearly seen that the upstream film hole arrangement covers a wider area of the blade tip than the camber arrangement. For the squealer tips, the film cooling effectiveness pattern at the bottom of the cavity develops from the camber line to the pressure side, which also matches the tip leakage flow inside the squealer cavity. As noted in earlier discussions, the camber arrangement only covers one half of the blade tip portion. On the other hand, the upstream film hole arrangement produced a better film cooling effectiveness since the film holes are located on the upstream side of the leakage flow to protect more blade tip area. The two-row film hole arrangement also provides better overall protection than the camber arrangement since some of the film holes were placed upstream of the leakage flow for more balanced coverage of the high heat transfer regions on the squealer tip.

For the range of blowing ratios considered here, the film cooling effectiveness generally increases with increasing blowing ratio. However, as the blowing ratio increases for the camber arrangement on the plane and squealer tips, the coolant may separate from the blade tip surface and penetrate through the tip

leakage flow rather than adhere to the blade tip. This results in a reduction of film cooling effectiveness downstream of the film holes as shown in Figures 4.9(e) and 9(f) for the $M = 2$ cases. It is also important to note from Figure 4.9(m) that there is no film cooling protection on the leading edge portion of the plane tip for the two-row arrangement under a low blowing ratio $M = 0.25$. This suggests that the hot gas may enter the first two film holes under low blowing ratio conditions. To prevent this failure, it is desirable to use a higher blowing ratio for the two-row arrangement on the plane tip.

Figure 4.10 compares the predicted film cooling effectiveness on the shroud for the plane and squealer tip cases with camber, upstream, and two-row film hole arrangements under three different blowing ratios of $M = 0.5$, 1, and 2 ($M = 0.25$, 0.5 and 1, respectively, for two-row configurations). For both the plane and squealer tip configurations, the film cooling effectiveness on the shroud increases with increasing blowing ratio. This is different from the film cooling on the blade tip, since the coolant penetrates the tip leakage flow and impinges directly on the shroud when the blowing ratio is high. For the plain tip configuration, the coolant traces on the shroud match closely with those observed on the blade tip but the level of film cooling effectiveness is directly opposite to that observed on the blade tip. More specifically, the low film cooling effectiveness on the shroud corresponds to high cooling effectiveness on the blade tip and vice versa. For low blowing ratio cases, the film cooling effectiveness on the shroud is lower than that observed on the blade tip since the coolant jets remain attached on the blade tip surface. With increasing blowing ratio, there is a drastic increase of the film cooling effectiveness on the shroud since the coolant can easily penetrate the narrow tip gap. On the other hand, the film cooling effectiveness on the shroud of the squealer tip is much lower than that on the blade tip because the cavity depth is relatively large. The coolant traces can no longer be seen since the coolant mixed well with the leakage flow inside squealer cavity before reaching the shroud. It is also worthwhile to note that some regions of the shroud around the blade trailing edge and suction side also benefit from the coolant leakage vortices.

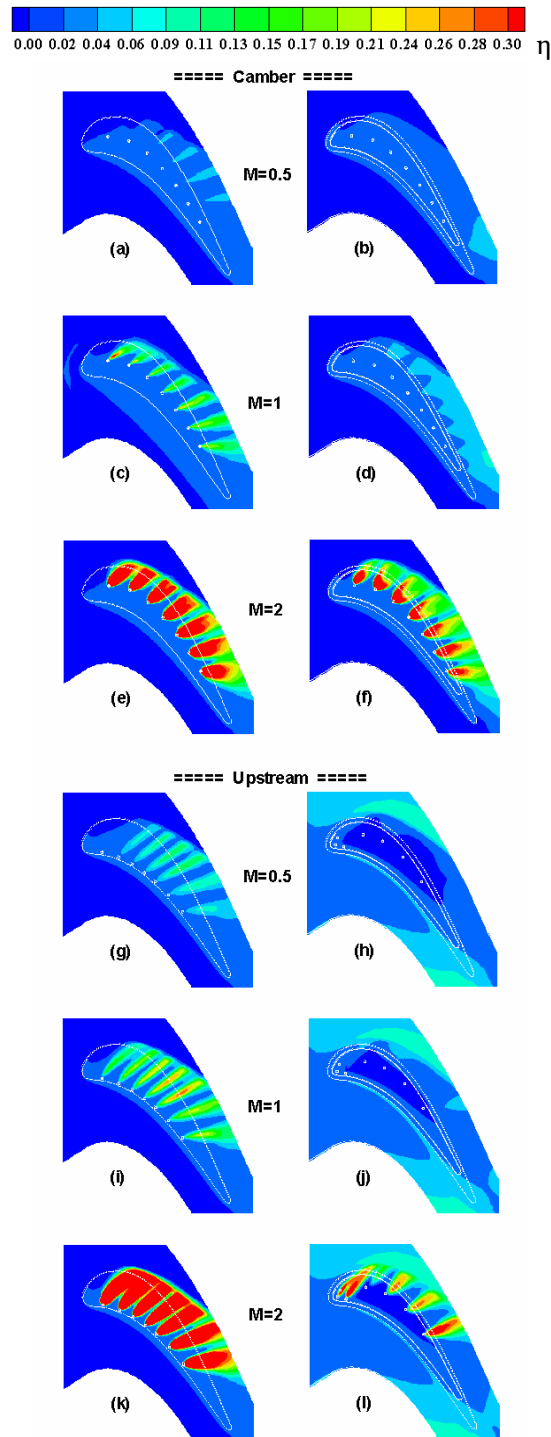


Figure 4.10 Comparison of film cooling effectiveness on the shroud for plane and squealer tip configurations with various film hole arrangements and blowing ratios, low parameter.

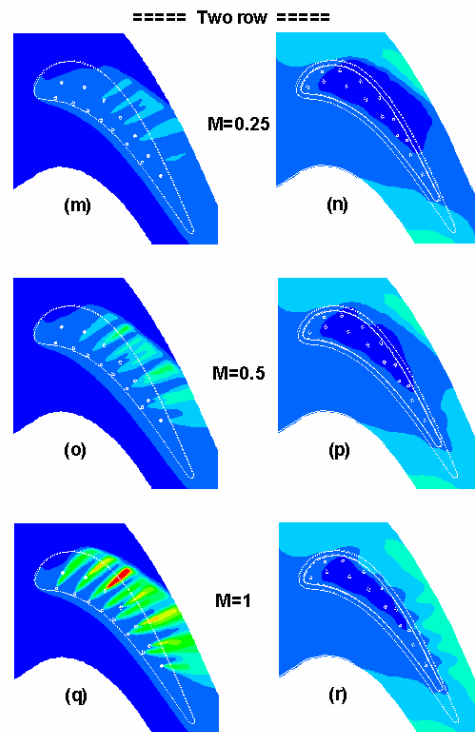


Figure 4.10 Continued

A detailed comparison of the area-averaged film cooling effectiveness on the blade tip is made in Figure 4.11 to evaluate the overall performance of various film hole arrangements. In general, the upstream and two-row film hole arrangements provide higher cooling effectiveness on blade tips than the camber arrangement for both the plane and squealer tips, especially for the high blowing ratio conditions. For the same amount of coolant usage, the squealer tip provides a better cooling effectiveness than the plane tip due to two reasons: 1) lower tip leakage velocity for the squealer tip; and 2) a large portion of the coolant are trapped in the squealer cavity as seen from the pathlines shown in Figure 4.8.

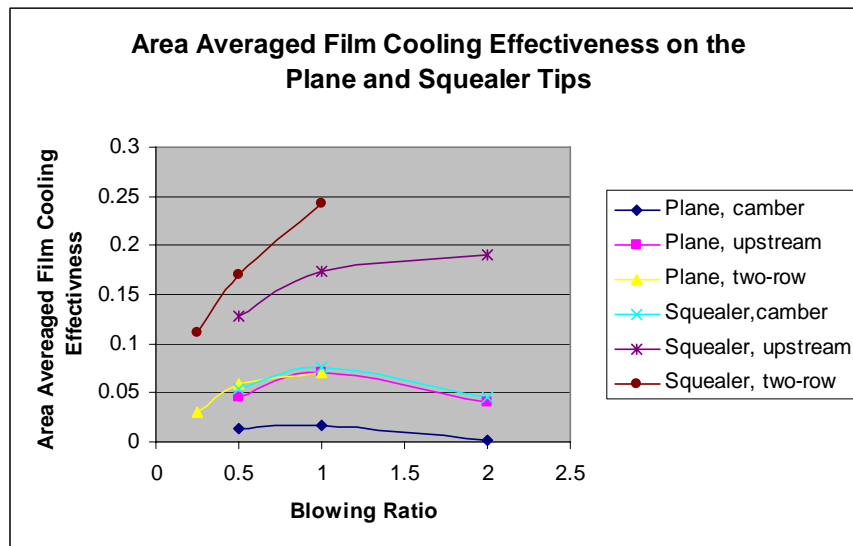


Figure 4.11 Comparison of area averaged film cooling effectiveness on the blade tip with various tip configurations and film hole arrangements, low parameter, non-rotating.

Figure 4.11 compares the area averaged film cooling effectiveness on the tips for various working conditions. As mentioned before, the blowing ratios for the two-row configurations are only one-half of the one-row configurations for the same amount of coolant. Generally speaking, the film cooling effectiveness increases with increasing blowing ratio, the three exceptions are the camber arrangements for both the plane and squealer tip cases, and the plane tip upstream arrangement at the highest blowing ratio of $M = 2$. For the camber arrangement of plane and squealer tip cases, the cooling effectiveness on the tips decreases after reaching a maximum value at around $M = 1$. At $M = 2$, the coolant jet lifts off from the blade tip and penetrates into the tip leakage flow with streamwise flow separation behind the coolant jets. It is worthwhile to note that the two-row arrangement provides the highest film cooling effectiveness at the highest blowing ratio (i.e., $M = 1$) for both the plane and squealer tip configurations. This can be attributed to the fact that the two-row coolant holes split the coolant and reduce the local blowing ratio, so the coolant tends to remain attached rather than penetrating the leakage flow for the range of blowing ratio considered. It is also interesting to note that the squealer tip upstream arrangement also provides the highest cooling effectiveness at the highest blowing ratio (i.e., $M = 2$) since the squealer tip is able to trap more coolant when the film holes are located in the upstream section of the squealer cavity.

4.3.4. Effect of Rotation on Film Cooling Effectiveness

Figure 4.12 compares the coolant pathlines of camber configurations under non-rotating and rotating conditions for both the plane and squealer tip configurations at a blowing ratio of $M = 1$. In general, the rotation tends to reduce the size of the coolant leakage vortex in the suction side passage since the blade is moving in the same direction as the tip leakage flow. As noted in our previous study for blade tip heat

transfer without film cooling, the rotating effect is confined to the shroud region and has relatively minor influence on the blade tips. Under the rotating conditions, the location of highest leakage flow shifts slightly downstream towards the trailing edge. However, the tip leakage flow is still dominated by the pressure gradient between the blade pressure and suction sides and the coolant traces are only slightly affected by the blade rotation.

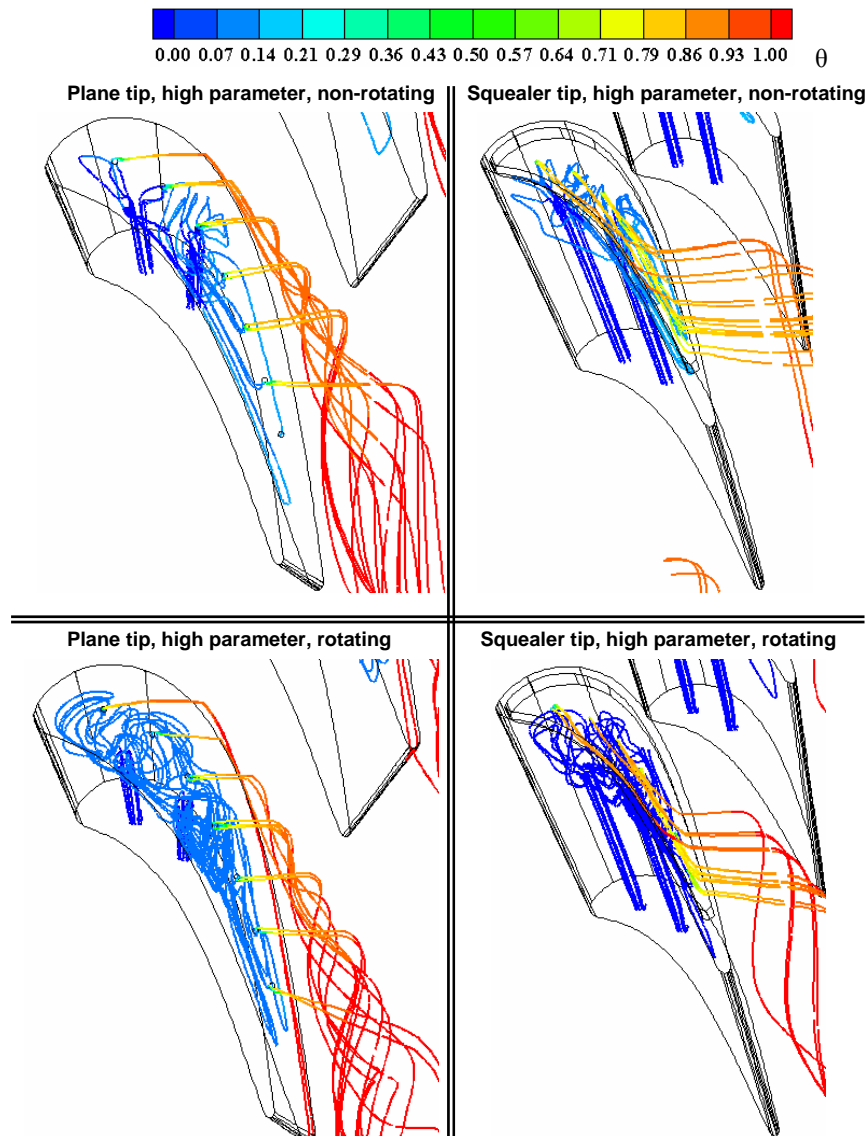
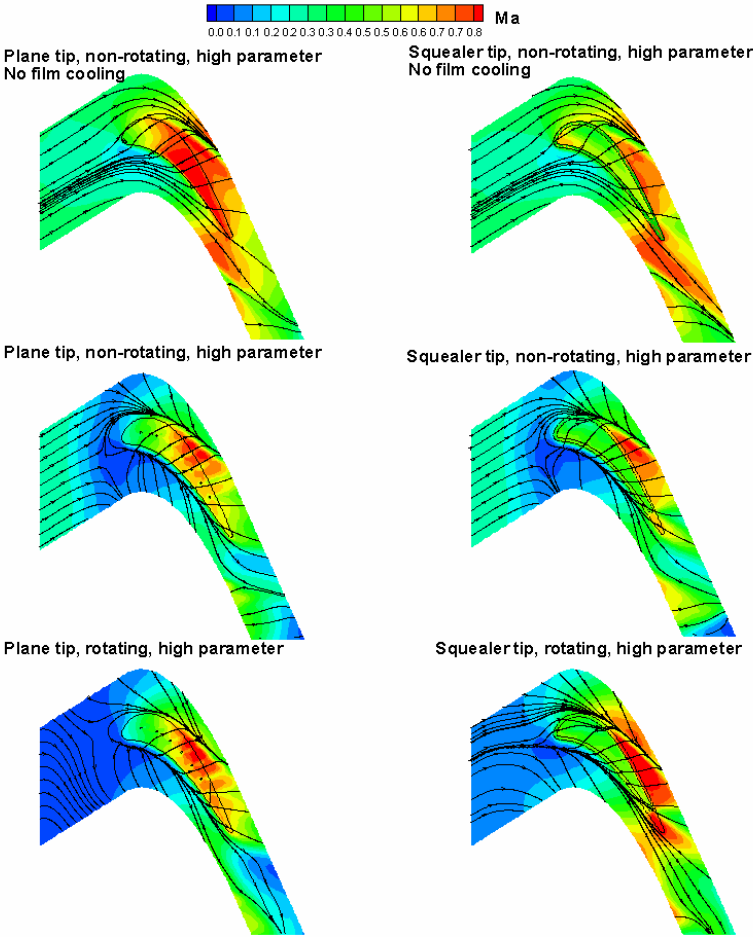


Figure 4.12 Comparison of coolant pathlines (colored by dimensionless temperature ϕ) for non-rotating and rotating cases, high parameter, $M = 1$.

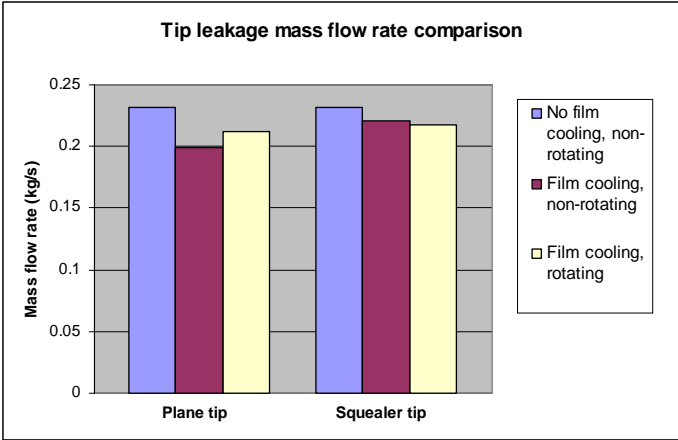
Figure 4.13 shows the effect of blade rotation on the streamlines and Mach number contours at the mid-gap plane and tip leakage flow rate for both the plane and squealer tip configurations. For

completeness, calculations were also performed for the non-film-cooled plane and squealer tip configurations under the same flow conditions to facilitate a detailed comparison of the film cooling effects. It is seen that the tip leakage flow is driven from the pressure side to the suction side for both the plane and squealer tip configurations. The Mach number contours indicate that the squealer tip reduces the tip leakage flow compared to the plane tip in the mid-gap plane. For the film cooling cases, the flow velocity reduces significantly at the mid-gap plane due to the blockage of the coolant jets. Furthermore, a portion of the mid-gap flow was deflected back to the pressure side as indicated by the streamline convergence pattern in the pressure side of the turbine blade. For the plane tip configuration, the effects of film cooling can be clearly observed from the low speed coolant traces at the mid-gap plane. On the other hand, the coolant traces are no longer visible for the squealer tip cases since the squealer cavity depth is considerably larger than the tip gap. This explains the difference of cooling effectiveness between plane and squealer tips shown as shown earlier in Figure 4.10. The bottom row of Figure 4.13(a) shows the streamlines for the rotating cases in a blade-fixed frame. The streamlines outside the blade tip region are turning toward the pressure side relative to the rotating blade. However, the streamlines in the tip gap region are still moving from the pressure side to suction side since the leakage flow for rotating cases is still dominated by the pressure gradients. It is further noted that the blade rotation tends to increase the tip leakage flow near the blade trailing edge for both the plane and squealer tip configurations. A more detailed discussion of the rotating effects on the tip leakage flow is given in chapter III.

Figure 4.13(b) compares the tip leakage flow rate for the plane and squealer tip configurations under various flow conditions. It is seen that the leakage mass flow rates are nearly identical for the non-film-cooled plane and squealer tips. Although the squealer tip reduces the leakage flow velocity in the squealer cavity, the overall leakage mass flow rate stays about the same due to increased cross-sectional area for the squealer tip configuration. It is also noted that the film cooling tends to reduce the leakage mass flow rates for both the plane and squealer tip configurations since the slower coolant jet act as a blockage to the tip leakage flow. For the film-cooled plane tip configuration, the blade rotation produced a significant increase of the leakage mass flow rate. On the other hand, the leakage flow rate for the squealer tip configuration is only slightly affected by the blade rotation at $M = 1$ since the coolant is not strong enough to penetrate the tip leakage flow at this blowing ratio.



(a)



(b)

Figure 4.13 Comparison of (a) streamlines, Mach number contours on the mid-gap plane; and (b) tip leakage mass flow rate for non-rotating no film cooling, non-rotating film cooling, and rotating film cooling cases under high parameter conditions, $M = 1$.

Figure 4.14 shows the streamlines and dimensionless temperature contours at two streamwise cross sections for the plane and squealer tips under various flow conditions. Each cross section consists of two separate planes (i.e., the pressure side plane and suction side plane as shown in Figure 4.4) which are perpendicular to the pressure side and suction side of the blade surface, respectively, and intersect at the camber line. It can be seen from Figure 4.1 that the first cross section cut through the center of the third film hole, the plenum, and the second coolant passage, while the second cross section cut through the center of the sixth film hole and the tail end of the plenum. In general, all tip leakage flows were driven from the pressure side to the suction side by the blade pressure gradient between two pressure side and suction side of the blade. The squealer tip is found to reduce the leakage vortex due to flow separation and recirculation inside the squealer cavity.

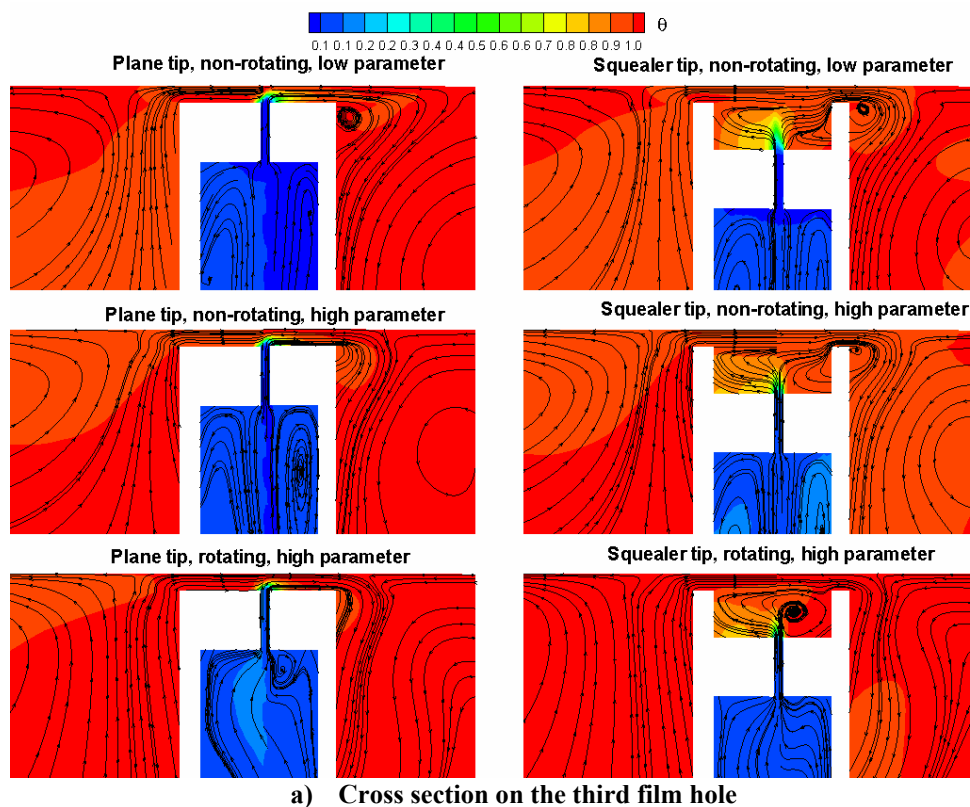
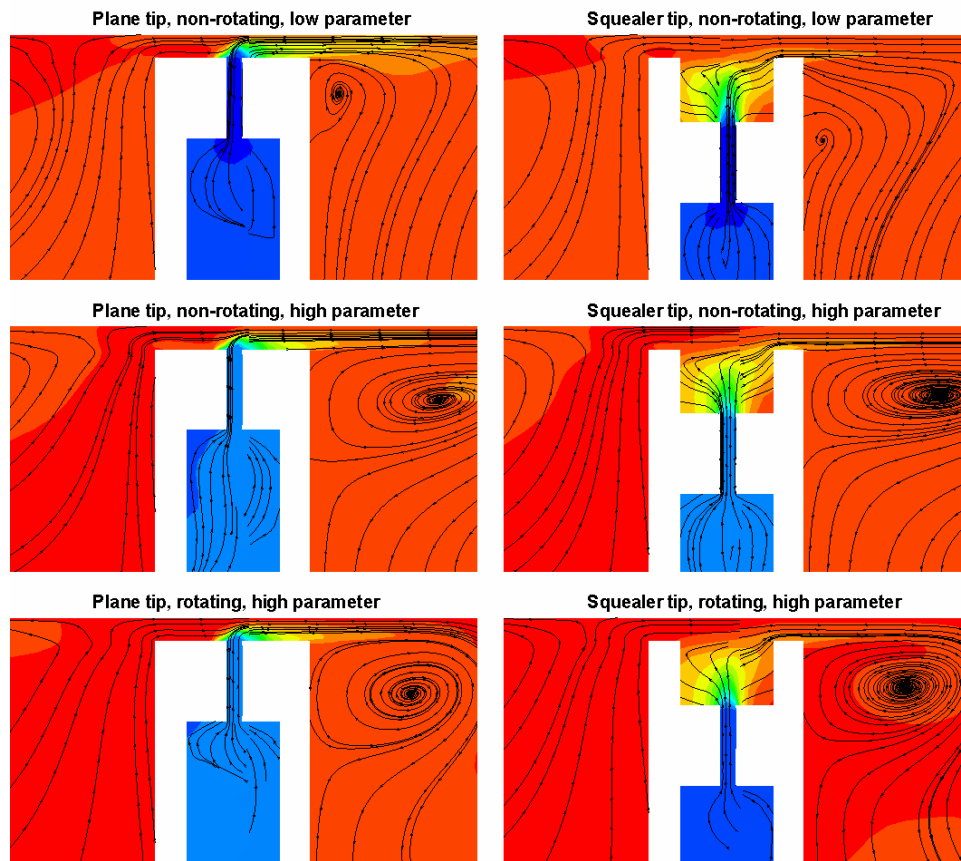


Figure 4.14 Comparison of pathlines and dimensionless temperature contours at two stream wise cross sections, $M = 1$.



b) Cross section on the sixth film hole

Figure 4.14 Continued.

As noted in Chapter III, for the non-film-cooled blade simulations, the location of the strongest tip leakage flow shifts downstream under high parameter conditions. This results in a somewhat weaker vortex at the location of the third film hole and a much stronger and larger leakage vortex at the sixth film hole. It is also interesting to note that the plenum flow patterns are drastically different between the third and sixth film holes. At the location of the third film hole, a large recirculation region is observed inside the plenum since the coolant exiting from the second coolant passage impinges directly on the top surface of the plenum. On the other hand, the plenum flow leaves the sixth film hole smoothly because the flow from the coolant passages must travel horizontally towards the tail end of the plenum before exiting the sixth film hole.

Comparing the non-rotating and rotating tip leakage flow rate in Figure 4.13 and flow pattern in Figure 4.14, it is quite clear that the blade rotation does not affect the tip leakage flow significantly since the leakage flow is still dominated by the blade pressure gradient under rotating conditions. At the location of the third film hole as shown in Figure 4.14(a), the size of the leakage vortex reduces slightly for both the plane and squealer tip configurations. However, the secondary flow inside the squealer cavity

is significantly altered with the formation of additional vortex around the coolant jet exiting from the third film hole. At the second cross section around the sixth film hole in Figure 4.14(b), a somewhat stronger leakage vortex is observed for both the plane and squealer tip configurations due to an increase of tip leakage velocity near the trailing edge as shown earlier in Figure 4.13. It is also worthwhile to note that the squealer cavity width is considerably narrower at the sixth film hole in comparison with that at the third film hole. Consequently, the effect of coolant jet on the squealer cavity temperature distribution is more pronounced near the blade trailing edge as seen in the cooling effectiveness contours shown in Figure 4.15.

Figure 4.15 shows a detailed comparison of the film cooling effectiveness on the blade tips under various flow conditions. It is seen that the high parameter condition produces a slight increase of the film cooling effectiveness on the blade tips for both the plane and squealer configurations due to the flow compressibility and viscous heating. As shown earlier in Figure 4.13, the blade rotation shifts the location of the strongest tip leakage flow downstream towards the trailing edge. This leads to an increase of film cooling effectiveness near the trailing edge and a significant reduction of the cooling effectiveness in the leading edge and mid-chord sections for the plane tip configuration. On the other hand, the rotating effect for the squealer tip configuration is confined to the trailing edge. The film cooling effectiveness on the floor of the squealer cavity is only slightly affected by the blade rotation since the tip leakage flow is relatively weak for the large cavity depth considered in the present study.

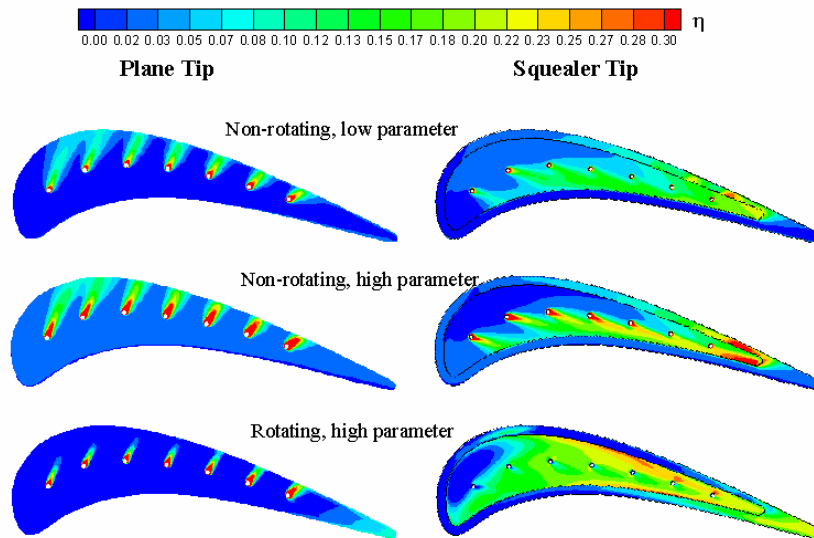


Figure 4.15 Film cooling effectiveness comparison on the plane and squealer tips for $M=1$ under various flow conditions.

4.3.5. The Heat Transfer Coefficient of Film Cooling

Figure 4.16 compares the predicted heat transfer coefficients for the camber line arrangement to the corresponding transient liquid crystal experimental data of Kwak et al.[18-19] for a blowing ratio of $M = 1$.

As noted earlier, there are thirteen film holes in the experimental configuration of Kwak et al.[18-19] but only seven film holes were considered in the present simulations while the blowing ratio is maintained the same. It is seen that the numerical simulation results are in good agreement in the pattern with the measured data for both the plane and squealer tips although the numbers of film holes are different. Both the measurement and simulation results exhibit a low heat transfer coefficient downstream of the film holes, which is different from most of the other film cooling applications with an increase of heat transfer coefficient as a result of film cooling. As shown earlier in Figure 4.13, the tip leakage velocity in the narrow tip gap is significantly higher than the mainstream flow in the cascade. Therefore, the coolant velocity is considerably slower than the tip leakage flow velocity even at a blowing ratio of $M = 1$. Furthermore, the coolant jets are issued into the tip gap normal to the tip leakage flow instead of at an inclined angle to the blade tip. Consequently, the low-speed coolant jets act as a blockage instead of a turbulator to the tip leakage flow even at $M = 1$. This leads to a reduction of heat transfer coefficient downstream of the film holes for the plane tip configurations shown in the left column of Figure 4.16. For the squealer tip configurations, the coolant blockage is not as strong as that for the plane tips because squealer cavity acts as a labyrinth seal to reduce the tip leakage flow. Therefore, the heat transfer coefficients on the squealer tip configurations do not clearly show a low heat transfer region downstream of the film holes.

Figure 4.17 shows a comparison of the Stanton number contours on the plane tip, squealer tip, and shroud for the non-rotating and rotating high parameter cases. In general, the blade rotation only slightly affects the heat transfer on both the plane and squealer tips. As noted earlier, the location of strongest tip leakage flow shifts toward the trailing edge under rotating conditions. A similar shift of the high heat transfer region is also observed in the Stanton number contours shown in Figure 4.17. There is a minor reduction of Stanton number near the leading edge, while the St value increases slightly in the mid-chord and trailing edge sections for both the plane and squealer tip configurations.

Unlike the blade tips which are fairly insensitive to the blade rotation, the instantaneous Stanton number on the shroud is strongly affected by the blade rotation. For the plane tip configuration, the Stanton number increases due to a sharp increase of the velocity and temperature gradients inside the shroud boundary as a result of the blade rotation. On the shroud wall directly opposite to the plane tip, however, the Stanton number patterns are very similar to those observed on the blade tip since the tip leakage flow is nearly two-dimensional in the narrow tip gap.

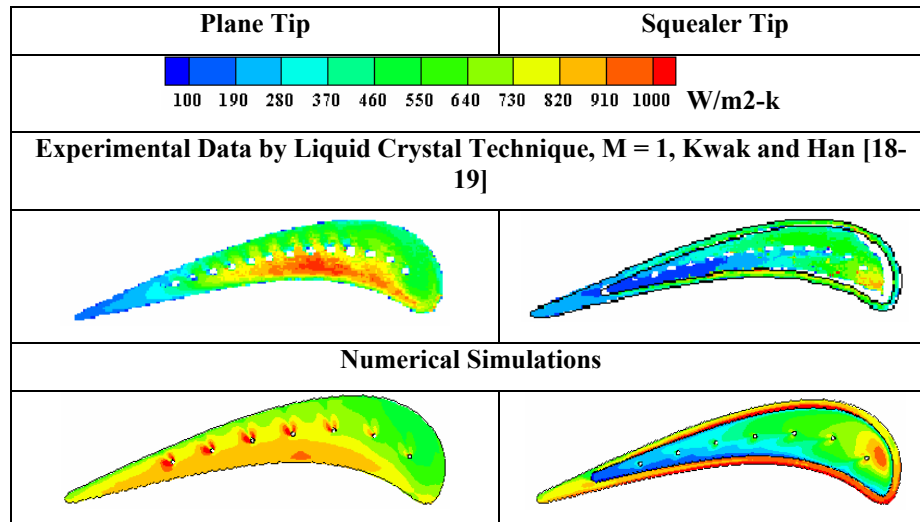


Figure 4.16 Comparison of heat transfer coefficients on the plane tip (left) and squealer tip (right) of camber arrangement, low parameter, M = 1.

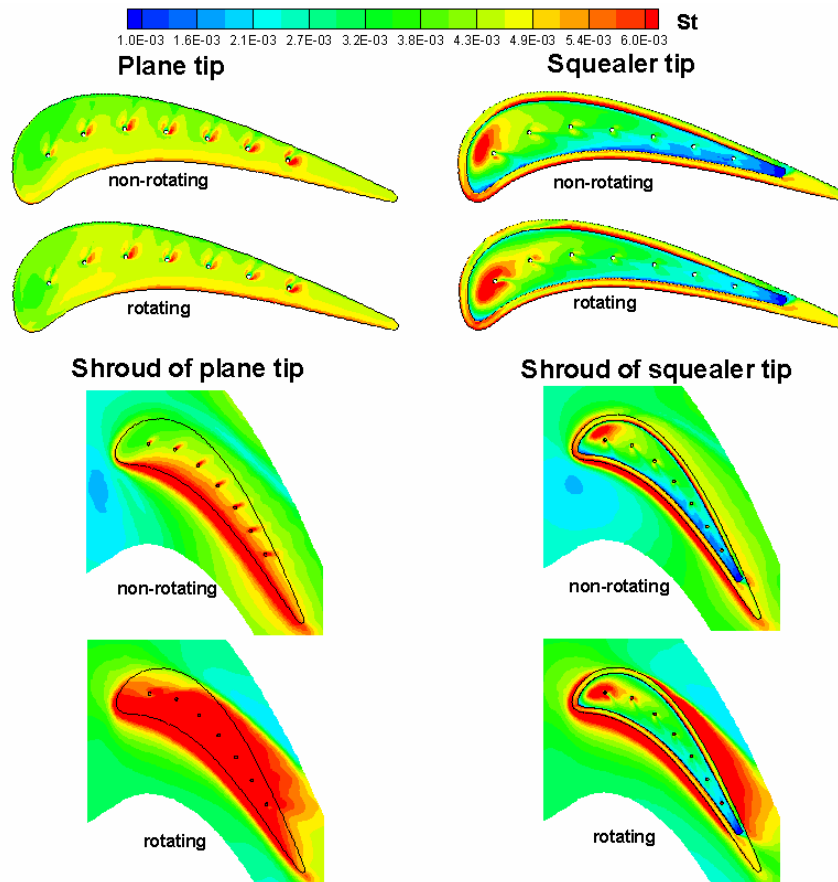


Figure 4.17 Comparison of instantaneous Stanton number contours on the plane and squealer tips and shrouds for the high parameter, non-rotating and rotating cases.

4.4. Conclusions of Blade Tip Film Cooling

Three different film hole arrangements including camber (holes located at mid-camber line), upstream (holes located upstream of the tip leakage flow and high heat transfer region) and two-row (combining upstream and camber arrangements) arrangements on the plane and squealer tips have been systematically investigated for both the low and high parameter, non-rotating and rotating conditions in this paper. Several major conclusions are listed in the follows:

- 1) The blade tip film cooling does not affect the overall blade pressure ratio distribution significantly, except for the region downstream of the film holes.
- 2) The upstream and two-row arrangements provide better film cooling performance on both the plane and squealer blade tips than the camber arrangement, especially at the high blowing ratios.
- 3) When the blowing ratio M reaches 1, the film cooling effectiveness cease to increase for the camber arrangement on both the plane and squealer tips due to the coolant separation from the blade tip. However, the film cooling effectiveness in the upstream and the two-row arrangements still tend to increase with higher blowing ratios.
- 4) The film cooling effectiveness on the shroud depends mostly on the blowing ratio, and is only slightly affected by the film-hole arrangements. The higher blowing ratio produces higher cooling effectiveness on the shroud for all cases considered.
- 5) For the range of blowing ratio considered in the present study, the coolant jets act as a blockage to the tip leakage flow. Therefore, low heat transfer coefficient is dictated downstream of the film holes on plane, squealer tips, and squealer shroud.
- 6) The rotation reduces the film cooling effectiveness on the plane tip significantly, while the film cooling effectiveness on the squealer tip is only slightly affected due to the large cavity depth.
- 7) The rotation significantly increases the heat transfer coefficient on the shrouds due to the increasing velocity and temperature gradient inside the shroud boundary layer.
- 8) The simulation shows that the blade suction side does not benefit from the tip film cooling for all cases considered.
- 9) The film cooling reduces the tip leakage mass flow rate for both the plane and squealer tip configurations. The squealer tip reduces the leakage flow velocity, but the overall leakage mass flow rate increases for the film-cooled cases due to increased flow area in the squealer cavity.

CHAPTER V

FILM COOLING ON THE BLADE LEADING EDGE

5.1. Problem Definition and Computational Details

The previous chapters have studied the heat transfer and film cooling on the blade tip region, this chapter has numerically investigated the film cooling on the leading edge. As indicated in the chapter I, the corresponding experimental study (Ahn et al. [34]) has been carried out on the “state-of-the-art” three stage research turbine facility at the Turbomachinery Performance and Flow Research Laboratory (TPFL) of Texas A&M University. Due to the limitation of the computational resource, the present three-dimensional calculations only includes the first 1-½ turbine stage, which contains the first-stage stator (stator 1), the first-stage rotor (rotor), and the second-stage stator (stator 2), as shown in Figure 5.1. Only the rotor blade is film cooled in the present study. The blade height is 63.5 mm, the root diameter is 558.8 mm, and the shroud diameter is 685.8 mm. Both the stator and rotor blades are two-dimensional with the same blade profiles in the span-wise direction, which is exactly the same as the experimental blade used by Ahn et al.[34]. In Ahn et al.[34] experiment, there are 58 stator 1 blades, 46 rotor blades and 52 stator 2 blades. To simulate the experimental conditions exactly, it is necessary to use 29 stator 1 blades, 23 rotor blades and 26 stator 2 blades with periodic boundary conditions along the circumferential direction. In order to significantly reduce the computer memory and CPU time requirements, it is desirable to use the same number of blades for both the rotor and stators in the 1- ½ turbine stage. This enables the authors to simulate only one flow passage with periodic boundary conditions in the circumferential direction. Since this paper focuses on the leading edge film cooling of the rotor blade, it is reasonable to simplify the turbine stage by using 46 blades for both the first- and second-stage stators while maintaining the correct number of rotor blades. For the film cooled rotor blade, there are 16 film cooling holes in the leading edge region arranged in two rows: pressure side row and suction side row. Each row has eight film cooling holes, the film cooling hole diameter is 1.19 mm and the distance between the film cooling holes is 9.5 mm in the span-wise direction, which gives a pitch-to-diameter ratio of 7.95. The pressure and suction side rows are located at $\pm 23.58^\circ$ from the stagnation line. The film cooling holes were oriented to the span-wise radial direction and inclined to the blade surface by 30° . Also the film cooled rotor blade is the same as that used in the experiment. More detailed geometries of the stator and the film cooled rotor blades are given by Ahn et al.[32]. Other information of that turbine rig with two-dimensional blades can be found in Schobeiri et al.[32-33]. Calculations were performed with three different rotating speeds: 1800, 2550 and 3000 rpm, where the 1800 rpm is defined as low-rpm condition, 2550 rpm is the design condition (which means the flow stagnation line matches the rotor blade geometry leading edge at the mid-span), and 3000

rpm is high-rpm condition, respectively. The numerical low-rpm condition, 1800 rpm, is different from the experimental data of 2400 rpm by Ahn et al.[34], since the experimental turbine rig can not reach such low rotating speed by its limitation. The inlet total and exit pressures of the turbine stage are $P_{in} = 101,356$ Pa and $P_{ex} = 85$ kPa, respectively, with a pressure ratio of 1.19. At the inlet of the first stage stator, the total temperature (323 K), turbulence intensity (5%) are specified with an inlet flow angle of 0 degree.

As mentioned in the introduction, the simulations were performed using the CFD software package Fluent (version 6). The solutions are obtained by solving the compressible Reynolds-Averaged Navier-Stokes (RANS) equations using a finite volume method to discretize the continuity, momentum and energy equations. The GAMBIT software was used to generate the unstructured grids, with a fine grid clustering around the blade boundary layer. The computational domain consists of fluid around the first stage stator blade, a film cooled rotor blade, and second stage stator blade with periodic boundary conditions imposed in the circumferential direction as shown in Figure 5.1. To facilitate a better understanding of the real turbine stage, the periodic grid has been repeated three times in the circumferential direction in Figure 5.1. The domain is divided into two regions with different grid structures to ensure adequate resolution of the complex three-dimensional flow and heat transfer in the film cooled leading edge of the rotor blade. The domain of the 1-½ turbine stage is composed entirely of the hexahedral cells. The second domain consists of two rows of film-hole tubes connected with a semi-circular plenum. Tetrahedral cells are used in the film coolant domain since they are very flexible to construct. An interface technique was used to handle the two different types of grids. Relatively coarse grids are used for the majority of the 1-½ turbine stage, while the film-holes tubes, the leading edge region of the rotor and the boundary layer of the blades consist of much finer grids for accurate resolution of the film cooling effectiveness and heat transfer. In the leading edge region of the rotor and the boundary layers of the stator and rotor blades, most of the y^* value for the near-wall grids falls between 30-100. The geometry and detailed numerical grids around a typical film cooled leading edge are shown in Figure 5.2.

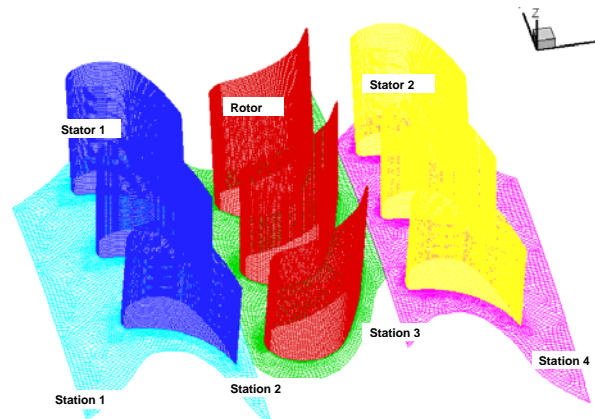


Figure 5.1 Computational domain and grids of a three-dimensional 1-½ turbine stage. (Passage was repeated three times)

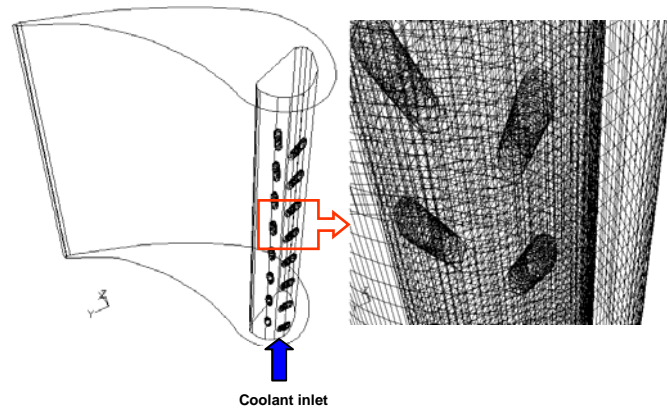


Figure 5.2 Film cooled leading edge of a rotor blade and grid structure.

The absolute inlet velocity of the rotor blade is 107 m/s. Three overall blowing ratios of the coolant jets ($M = 0.5, 1$ and 2) with density ratio 1 are studied. A fixed mass flow rate boundary condition is specified at the inlet of the coolant plenum as shown in Figure 5.2, with temperature equal to 300K. The adiabatic wall boundary condition is used on the blades and end wall for the calculation of the film cooling effectiveness. On the other hand, different thermal boundary conditions are used for the calculation of heat transfer coefficients, such as the wall temperature is fixed at 300 K, while the inlet coolant total temperature is maintained the same as the turbine stage inlet total temperature of 323 K.

All calculations are converged to residual levels of the order of 10^{-5} , and to less than 0.1% error in the mass flow rate between the main stream and coolant inlet and outlet of the computational domain. The selection of the time step is critical for accurate time-dependent flow predictions. Here, 100 time steps are used in calculating one passing period of the rotor blade. The passing period, T , is defined as the time it takes for the rotor blade to move from one stator row to another. The computed results are recorded and analyzed once every 25 time steps (i.e., every $1/4$ passing period). To achieve good periodic results, simulations were performed for 10 passing periods and the numerical results are presented at four different time phases with $t/T = 9^{1/4}, 9^{1/2}, 9^{3/4}$, and 10 respectively.

The grid independency study has been carried out with three sets of grid. The stator 1 and stator 2 computational domains consist of 0.3 million cells respectively, and do not change since this study mainly focus on the film cooled rotor. For the coarse set of grid, the rotor domain has about 0.5 million cells, the intermediate set is about 1 million cells; while for fine set grid, the rotor domain has about 1.5 million cells. Note that the near wall grid distance does not change for these three sets grid to keep y^* falling between 30-100. The overall film cooling effectiveness on the rotor has been compared in Figure 5.3. The difference between intermediate and fine grid is small, thus the fine grid can reach the grid independency. Since this study involves the unsteady three dimensional calculation with sliding mesh, it is very

computational intensive. Each case costs SGI Altix 3700 supercomputer in Texas A&M University about two weeks. It should be noted that, at this moment, this study can only focus on the overall film cooling of the rotor in a 1-1/2 turbine stage, instead of a detailed film coolant behavior near the film holes.

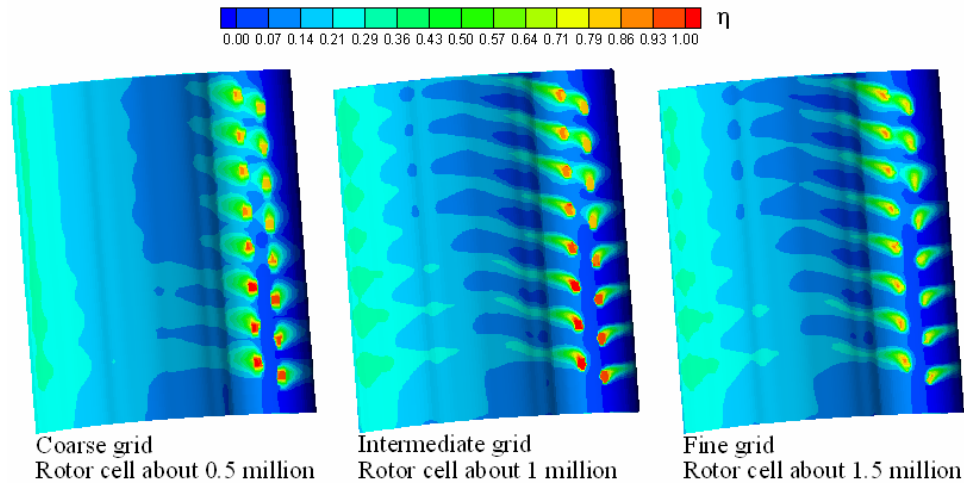


Figure 5.3 Grid independency study.

In addition to the three-dimensional simulations of the 1-1/2 turbine stage, two-dimensional calculations were performed for a three-stage turbine with the same rotor and stator blade profiles at the mid-span of the turbine to provide more detailed understandings of the unsteady flow and heat transfer induced by the rotor interaction in a multi-stage turbine. This multi-stage calculation is more similar to Ahn et al.[34] experimental rig since their rig consists of three stages. Because the number of grid cells and the CPU time requirement are significantly lower for the two-dimensional turbine stages, it is possible to analyze the more detailed heat transfer coefficient and film cooling effectiveness for more time phases. Furthermore, it is also possible to consider additional turbine stages in order to minimize the effects of downstream outlet boundary conditions. Since the stator and rotor blades studied in this paper are fully cylindrical two-dimensional blades without twist in the span-wise direction, the two-dimensional results are also useful in explaining some of the three-dimensional results in the mid-span region. As shown in Table 5.1, totally there are sixteen cases simulated in this paper, including 10 cases of 3-D simulation, and 6 cases of 2-D simulation.

5.2. Results and Discussion for Two-Dimensional Study

Figure 5.4 compares the instantaneous streamlines (colored by Ma number) at absolute and relative references with various rotting speeds, explains the rotor inlet velocity triangle and the stagnation line. The streamlines in Figure 5.4a is based on the absolute reference, i.e., the earth-fixed reference. The turbine

inlet flow is accelerated and guided by the stator 1, turns to the direction that perpendicularly push against the rotor 1. The rotor, therefore, rotates and converts some of the gas total energy to the mechanic energy.

Table 5.1: Matrix of simulation cases.

Calculating cases		Under design condition	At design condition	Over design condition
3-D Heat Transfer	M=0.5		X	
	M=1	X	X	X
	M=2		X	
3-D Film Cooling	M=0.5		X	
	M=1	X	X	X
	M=2		X	
2-D Heat Transfer	M=1	X	X	X
2-D Film cooling	M=1	X	X	X

It is worthwhile to note that the rotor absolute inlet velocity angle does not change significantly with various rotating speeds. Because in this study, the turbine inlet/outlet pressure ratio maintains constant, and the absolute velocity of rotor is mainly decided by the pressure ratio. In addition to the absolute reference, the streamlines based on the rotating relative reference have been plotted in Figure 5.4b. For the stators, the streamlines flow along the blades, this is identical to the absolute reference in Figure 5.4a since the stators do not move. For the rotor, however, the streamlines are totally different from the absolute reference, the fluid flows along the rotor blade instead of pushing against it. Because when the observer jumps from the earth to the rotor, and moves together with the rotor, the fluid looks like that it is guided by the blade profile of the rotor. Also Figure 5.4b indicates that the incident angle of the rotor relative inlet velocity changes with the increasing rotating speed, since the rotor relative velocity is highly related to the rotating speed, which is different from the rotor absolute inlet velocity in Figure 5.3a.

The relationship of rotor inlet absolute and relative velocity with various rotating speeds has been conceptive plotted in Figure 5.4c. As mentioned before, the rotor inlet absolute velocity (V_2) is only slightly affected by the rotating speed, while the rotor inlet relative velocity (W_2) highly depends on the

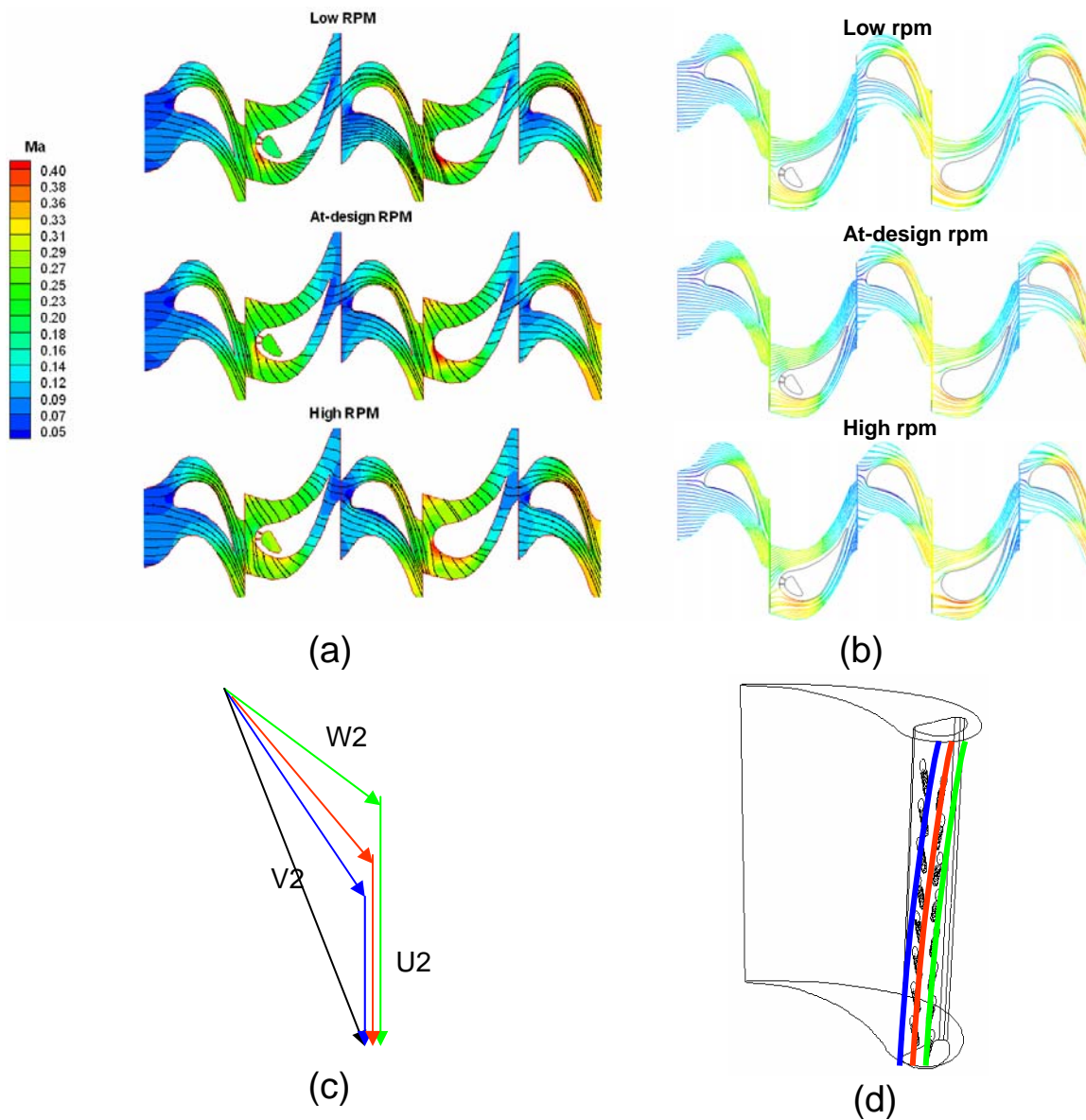


Figure 5.4 Velocity field of two-dimensional 3 turbine stage: a) instantaneous streamlines based on the absolute reference, b) instantaneous streamlines based on the relative reference, c) rotor inlet velocity triangle, and d) stagnation lines of various rotating speed on the leading edge of the three-dimensional rotor blade.

rotating speed as demonstrated in this velocity triangle. It is clear to see that with rotating speed or radial span increases, the rotating velocity (U_2) increase from blue to red and green color. Therefore, the relative inlet velocity (W_2) decreases with an increasing incident angle from the green to red and blue color, respectively. The stagnation lines of various rotating speeds and radial span on the leading edge of the rotor are shown in Figure 5.4d. It is found that the low speed stagnation line (blue) lies on the pressure side due to a large incident angle in Figure 5.4c. When the rotating speed increases, the incident angle

decreases, consequently the stagnation line moves from the pressure side to the leading edge, then to the suction side. Correspondingly the color changes from the blue to the red, then the green. Also it is worthwhile to note that the stagnation line is not a simple straight line for the two-dimensional non-twist blade, it is tilted from the pressure side root region to the suction side tip region, because the increasing radial span increases the U_2 , the W_2 changes on the various span locations, such that the two-dimensional blade is not an optimized design. The authors believe that the well designed three-dimensional twist blade can avoid this defect.

The unsteady characteristic of the rotating turbine stages has received increasingly attention recently, because the temperature fluctuation results in additional thermal stresses in comparison with the steady temperature field. It is, therefore, desirable to investigate the unsteady characteristics of multi-stage turbines for the real turbine flow conditions. However, it is still impractical to perform fully three-dimensional flow simulations of multi-stage turbines over long durations due to the limitation of the available computer resources. In the present study, the two-dimensional simulations have been analyzed to provide more complete information. In order to provide a quantitative measurement of the unsteady characteristics of parameters, such as heat transfer coefficient or film cooling effectiveness, it is necessary to define the unsteady intensity of these parameters. For example, the unsteady intensity of heat transfer coefficient is defined below:

$$Tu_h = \frac{\sqrt{\frac{1}{n} \sum_{i=1}^n (h_i - h_{average})^2}}{h_{average}} \quad (5.1)$$

Where h_i is the instantaneous heat transfer coefficient in the time step i , and n is the total number of time steps. This concept is similar to the turbulence intensity by using Root Mean Square (RMS) method. Also the same definition of unsteady intensity has been applied to the film cooling effectiveness:

$$Tu_\eta = \frac{\sqrt{\frac{1}{n} \sum_{i=1}^n (\eta_i - \eta_{average})^2}}{\eta_{average}} \quad (5.2)$$

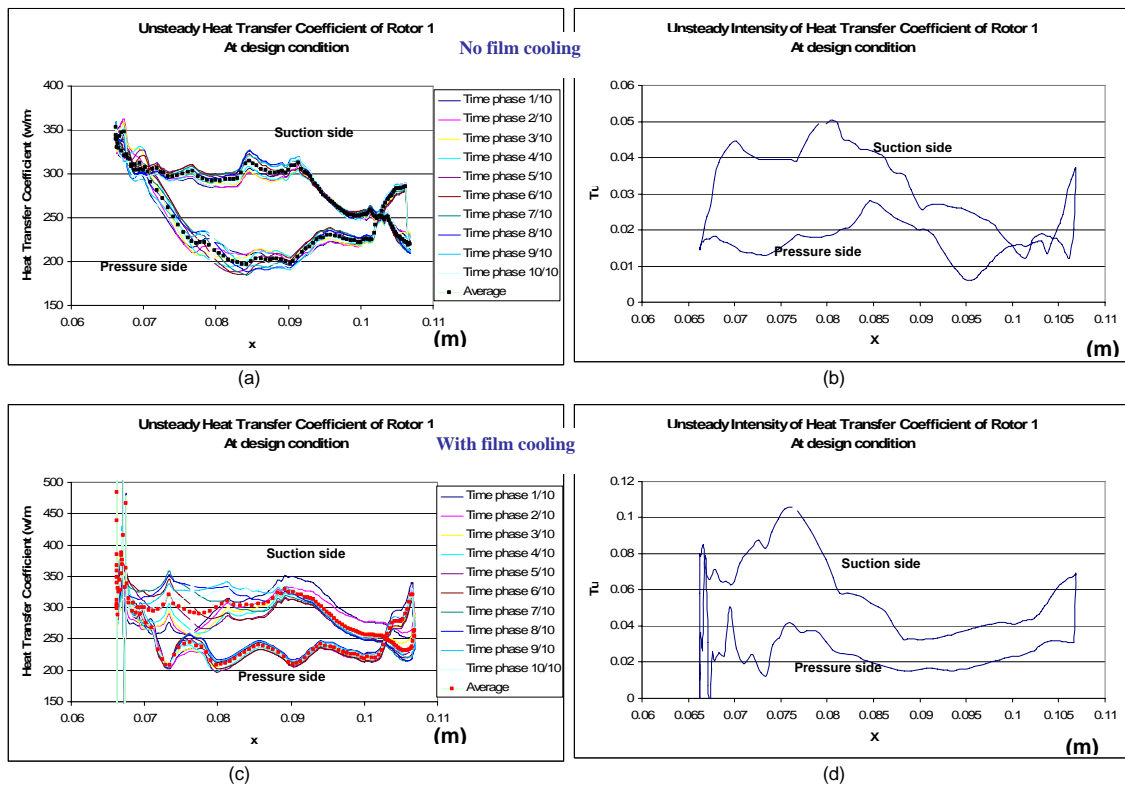


Figure 5.5 Rotor unsteady heat transfer comparison between without and with film cooling, 2500 rpm condition, $M=1$: a) instantaneous and averaged heat transfer coefficient without film cooling, b) unsteady intensity of heat transfer without film cooling, c) instantaneous and averaged heat transfer coefficient with film cooling, and d) unsteady intensity of heat transfer with film cooling.

Figure 5.5 compares the unsteady heat transfer coefficient between with and without film cooling for at-design conditions. The thin lines in the Figures 5.5a and 5.5c show the instantaneous heat transfer coefficient at various time phases, while the bold dot lines demonstrate the averaged one. Figures 5.5a-b show heat transfer coefficient without film cooling cases, while Figures 5.5c-d illustrate the cases with film cooling. From the Figures 5.5a and 5.5b, it is clear to see that the high heat transfer exists on the suction side due to the high velocity, while low heat transfer happens on the pressure side because of low velocity. Also the coolant jet significantly increases the unsteady intensity of heat transfer coefficient, because it disturbs the mainstream flow and magnifies the unsteady characteristic caused by the rotor interaction. The effect of this kind magnification by coolant is significantly high on the suction side, since the flow meets the positive pressure gradient there, and tends to be more easily disturbed. Figure 5.5b shows that the unsteady intensity of heat transfer without film cooling, the suction side Tu_h is higher than the pressure side, and the peak value is about 5%. This means, the effect of the rotor interaction in a subsonic turbine stage is not significant for the non-film-cooled cases; therefore, it sounds good news that most previous studies considering only single rotor can still be applied to the real turbine stages. Figure

5.5d, however, demonstrates that the unsteady intensity of heat transfer coefficient with film cooling is significantly high, and the peak value on the suction side can reach 10%. Consequently, for the film cooled cases, the rotor interaction should be considered by studying a full turbine stages to reach a real understanding of flow physics.

Figure 5.6 shows the unsteady film cooling effectiveness and intensity of the rotor. Figure 5.6a denotes the instantaneous and averaged film cooling effectiveness. It is interesting to find that the pressure side has a small fluctuation of the cooling effectiveness, which is similar to the heat transfer in Figure 5.5c. Because the negative pressure gradient exists there and accelerates the flow, tends to make the flow more stable and yield a high value of cooling effectiveness. The high fluctuation of cooling effectiveness, however, is found on the suction side with a low averaged value. Since the flow on the blade suction side meets the positive pressure gradient, which is against the flow direction and tends to make the flow unstable. The unsteady intensity of cooling effectiveness for the rotor has been plotted in Figure 5.6b. As we expected, the low value of Tu_{η} exists on the pressure side, and high value is found on the suction side. Also it is worthwhile to point out that the peak of cooling effectiveness unsteady intensity on the suction side is about 25%, much higher than that of the heat transfer value 10%. Which means film cooling effectiveness is much more sensitive to the rotor interaction than that of the heat transfer coefficient. The authors tend to believe that the cooling effectiveness is decided by the mixture of coolant and mainstream flow, which is some kind away from the wall, and more sensitive to the rotor interaction; while heat transfer happens very close to the wall, and not as sensitive as cooling effectiveness.

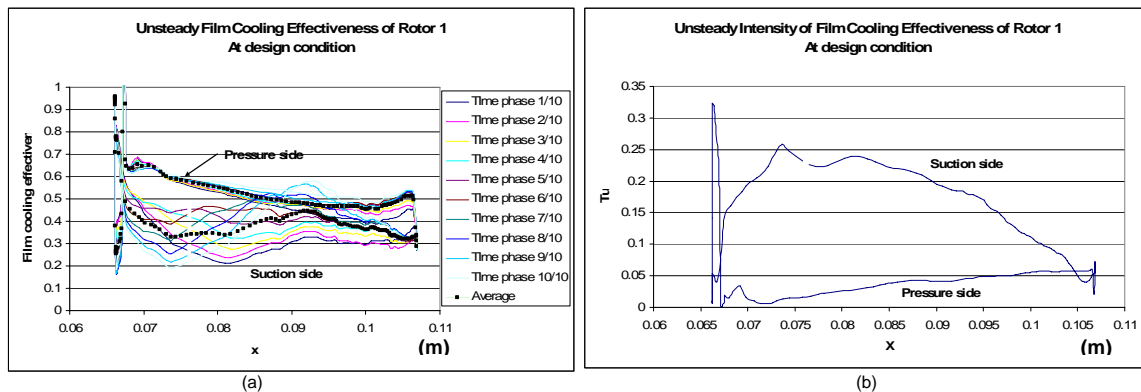


Figure 5.6 Rotor unsteady film cooling effectiveness and intensity, 2550 rpm condition, M=1: a) instantaneous and averaged film cooling effectiveness, and b) unsteady intensity of the film cooling effectiveness.

5.3. Results and Discussion for Three-Dimensional Study

5.3.1. Flow Field

Besides the two-dimensional study of the unsteady characteristic for the 3 turbine stage, the three-dimensional 1-1/2 turbine stage has been studied for the detailed distribution of film cooling and heat transfer on the leading edge of the rotor. From now on, if it is not specially mentioned, all discussion will be based on the three-dimensional simulation.

Figure 5.7 plots the rotor relative position on the mid-span of the three-dimensional 1-1/2 turbine stage together with velocity contour colored by Ma number based on the relative reference. There is a velocity defect region downstream the first stator due to the trailing edge thickness and blade profile boundary layer, which is called wake. When the rotor moves to the middle turbine passage at time phase 1, the stator 1 wake becomes weaker due to the large blockage caused by rotor at that position. Then the rotor moves forward to time phase 2, the stator 1 wake becomes stronger and strikes the pressure side of the rotor leading edge. The wake continually increase to the strongest at time phase 3 and hits the leading edge of the rotor; then discontinues and becomes weak again at time phase 4, sweeps at the suction side of the rotor leading edge. At last, it continues again from the time phase 1 to 4 for the next passing period.

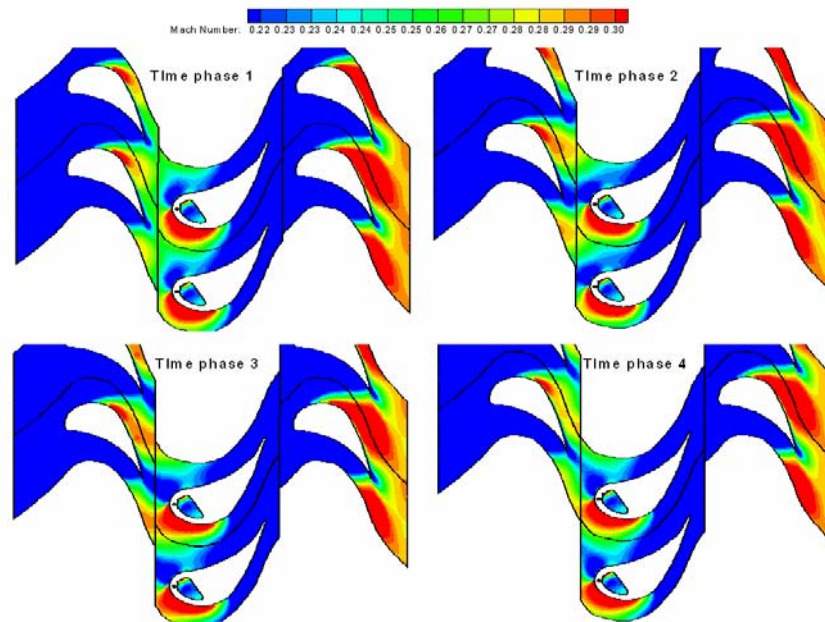


Figure 5.7 Stator 1 wake (colored by relative Ma number) and rotor relative positions for various time phases, 2550 rpm condition, $M=1$.

Correspondingly, the velocity contour at station 2 at four time phases has been compared in Figure 5.8. As noted before in Figure 5.1, the station 2 is located after stator 1 and before the rotor 1. The wake

changes for various time phases not only at the stream-wise direction as shown in Figure 5.8, but also in the span-wise plane. For the time phase 1, the wake is the weakest compared with other time phases because of the large blockage by the rotor. Then the wake becomes stronger and stronger at time phases 2 and 3 as rotor moves away from the mid-passage, decrease again in time phase 4. Some secondary flow caused by the end walls can be clearly detected near the casing and hub region.

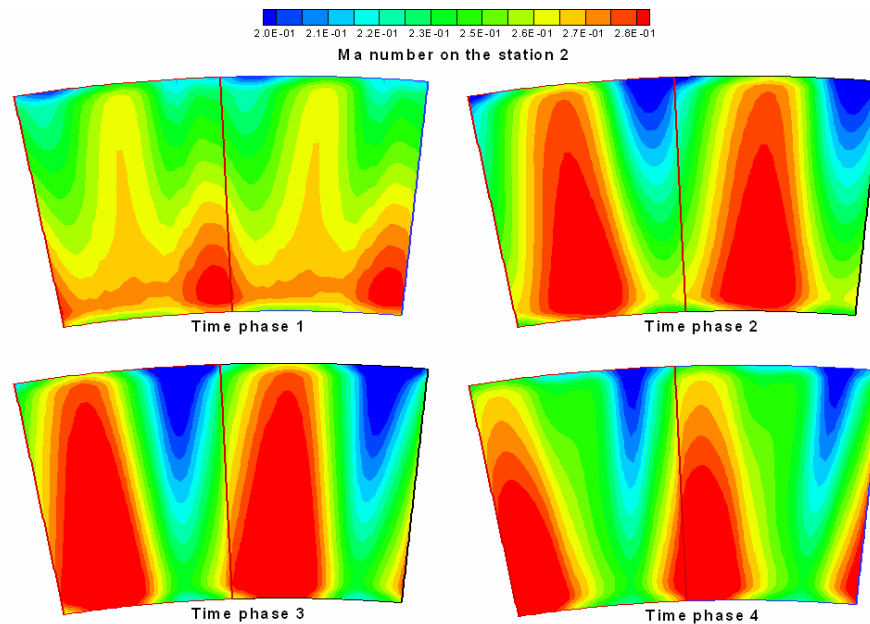


Figure 5.8 Velocity contours comparison (colored by relative Mach number) at station 2 for various time phases, 2550 rpm condition, $M=1$.

Figure 5.9 shows the comparison of static pressure distribution of the 1- $\frac{1}{2}$ turbine stage at four time phases for the design condition, $M=1$. The static pressure decreases along the flow direction in the turbine stage since part of the gas total energy is converted to kinetic energy and transferred to the rotating blades as the air flows through the turbine stage. It is also worthwhile to note that the pressure distribution around the leading edge of the rotor blades varies from one time phase to another due to the rotor interaction. There are two reasons of the rotor interaction in the present study: the main reason is that the rotation-induced pressure gradient propagates both upstream and downstream of the rotor blade and results in pressure fluctuations around the trailing edge of the first-stage stator as well as the leading edge of the second-stage stator. Another reason is due to the fluid viscosity, which causes a low velocity wake region behind the blade trailing edge as shown in Figure 8. Since it is a sub-sonic flow in this paper, the shock effect can not be detected. When the rotor moves into the wake region of the first-stage stator, it experienced a sudden change of inflow velocity and a significant pressure fluctuation. Downstream of the rotor, a much stronger pressure variation is observed for the stator 2 since they are directly affected by the unsteady flow generated by the rotor blades. It should be noted also that the rotor is much closer to the

wake of stator 1 in time phase 2 and 3 than that in the time phase 1 and 4, which can be easily detected by the comparison of the rotor position with the extended camber line from the trailing edge of the stator 1. Due to the two-dimensional blade used in the present study, the pressure distribution on the blades shows nearly two-dimensional pattern except for the end-wall regions of the blade tip and root where the secondary flow effect becomes important. The effect of the film cooling on the pressure field is limited to a small region near film holes, and does not extend to the other portions of the blade. This shows that the film cooling with blowing ratio $M=1$ does not significantly affect the overall aerodynamics performance.

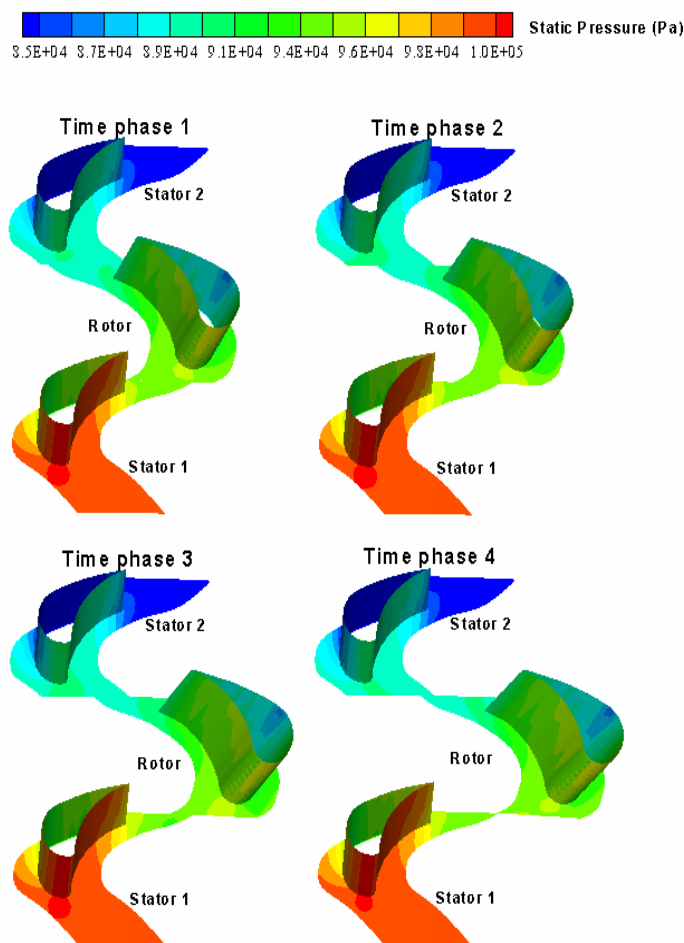


Figure 5.9 Static pressure distribution of 1-1/2 turbine stage for four time phases, 2550 rpm condition, $M=1$.

Figure 5.10 shows the instantaneous streamlines of coolant jets at four time phases for three rotating speeds. It is interesting to note that the film coolant jets are fairly stable at various time phases, although the velocity defect at station 2 shows an unsteady character. This suggests that the stability of coolant pathlines may be damped by the plenum inside the rotor blade. The function of plenum works like a reservoir and damps the fluctuation of film cooling caused by the rotor interaction. The coolant flow

direction is strongly affected by the rotating speed of the rotor blade. For the low rpm, most of the pathlines shift to the suction side except for the pressure side row near the blade tip. For the design condition, as expected, the traces of pressure side coolant always stay on the pressure side in four time phases, while most suction side row film coolant traces cover the suction side. However some suction side row traces near the tip region shift to the pressure side instead of staying on the suction side. For the high rpm condition, all of the coolant traces move from the suction side to the pressure side except for the suction side row traces near the root region, which still adhere to the suction side. The shift of coolant trajectory can clearly be attributed to the change of stagnation line position and the relative velocity incident angle on leading edge of the rotor blade at various rotating speed as shown in Figure 5.4d. The discrepancy of coolant traces near the end walls is similar to the Ahn et al [34] measured results, because the two-dimensional rotor blade is used. The true stagnation line on the leading edge tilted from the pressure side root region to the suction side tip region, instead of a simple straight line as the two-dimensional blade leading edge. It is anticipated that a well-designed three-dimensional twisted blade can avoid this problem, and therefore, increase the aerodynamic performance. However, the purpose of this paper is to calibrate the numerical method with the experimental data of Ahn et al.[34] which is the only one available for rotating film cooling experiments. Therefore, their two-dimensional blade is used instead of a more realistic three-dimensional twisted blade.

5.3.2. Heat Transfer Coefficient

Figure 5.11 shows the heat transfer coefficients on the 1-½ stage stator and rotor blades at four different time phases for the design condition, $M=1$. In general, the highest heat transfer coefficient is observed on the leading edges of the stator and rotor blades due to the presence of the stagnation flow on the blade leading edge. It is also noted that the heat transfer coefficient is higher on the suction side for both the rotor and stator blades because the mainstream velocity on the suction side is significantly higher than that on the pressure side. In the leading edge region of the rotor blade, the heat transfer is further enhanced downstream the film holes by coolant jets which disturb the mainstream flow. There is also a notable decrease on heat transfer coefficient on the second-stage stator blades compared to the first-stage stator blades, although they have the same blade profile. The mainstream temperature in the second stage decreases significantly due to the work process of turbine, although they are located downstream of the rotor blade with high turbulent unsteady wake, the overall effect reduces the heat transfer coefficient on the stator 2. Therefore the heat transfer coefficient on the turbine second stage is not as high as the first stage. On the other hand, the effect of blade rotation on the heat transfer coefficient of the first-stage stator is relatively small and confined to the trailing edge region because the position of stator 1 is located upstream the rotor.

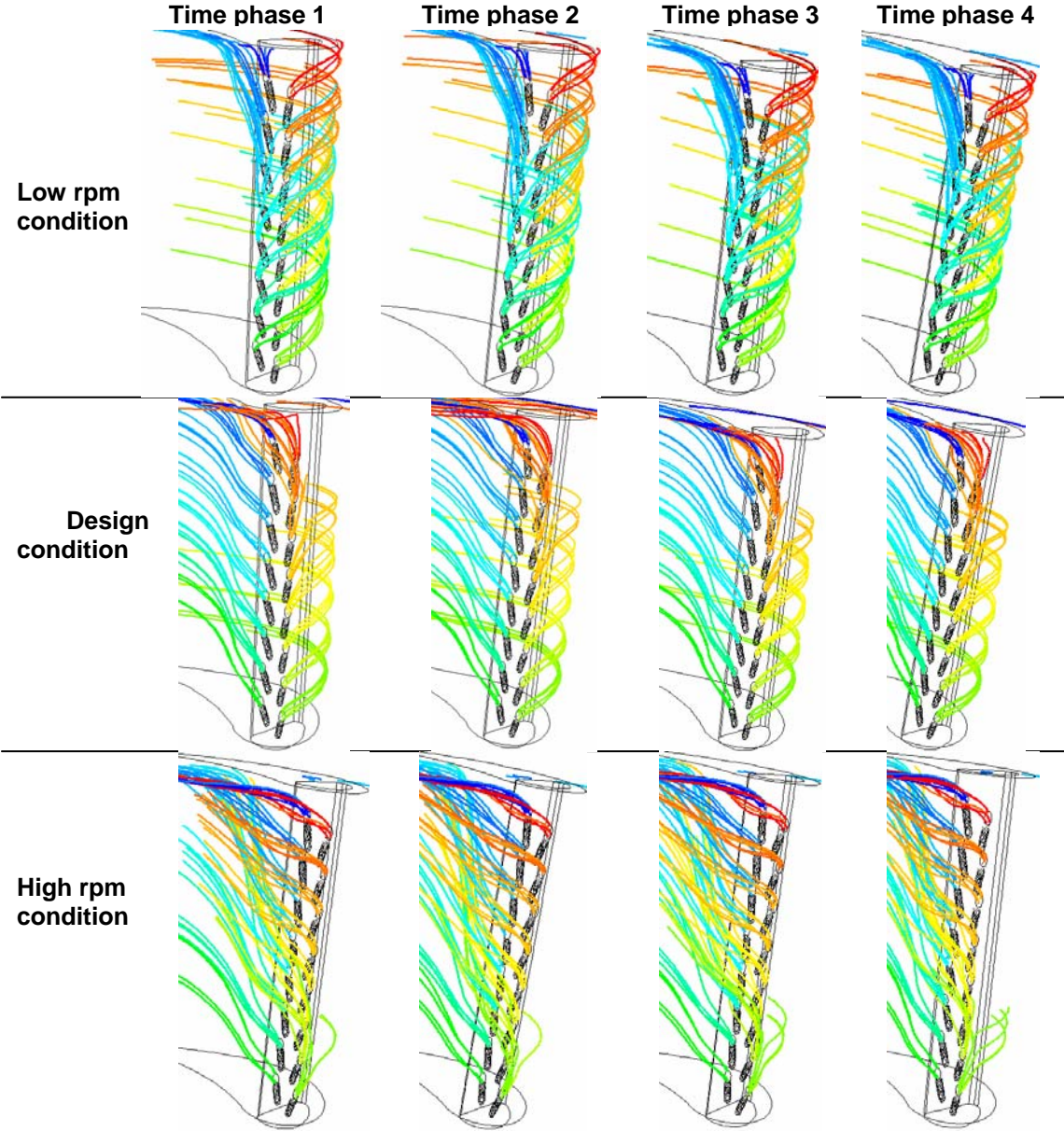


Figure 5.10 Comparison of instantaneous coolant pathlines (colored by the particle number) at four time phases as well as three work conditions, $M=1$.

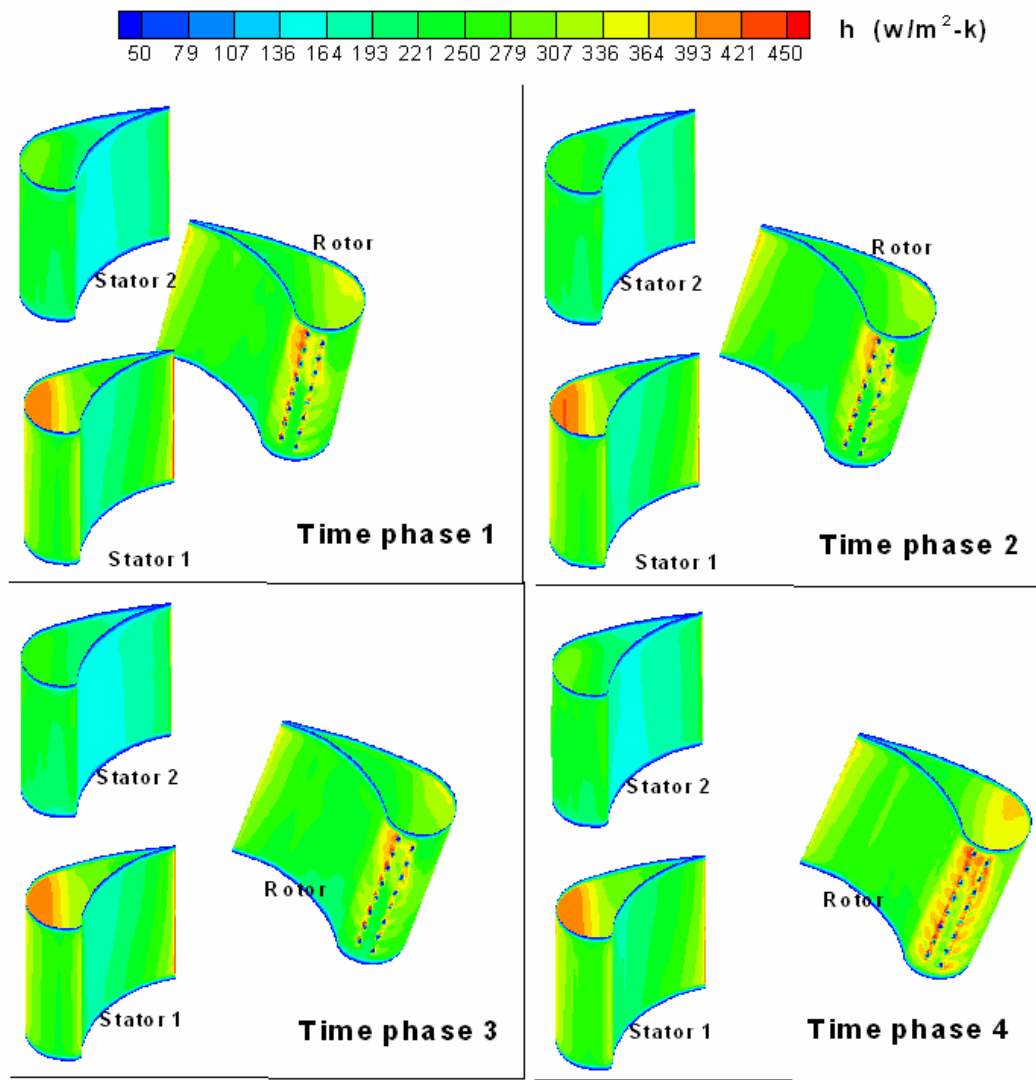


Figure 5.11 Heat transfer coefficient comparison of stator and rotor blades in 1-½ stage turbine for four time phases, design condition, M=1.

Figure 5.12 compares the heat transfer coefficient distribution on the leading edge of the rotor blade at four time phases with three working conditions. In general, the overall heat transfer coefficient slightly increases with increasing rotating speed, although the relative inlet velocity of the rotor decrease as shown in Figure 5.4c. This is because the high speed rotation creates highly unsteady turbulent wake flow, and causes higher heat transfer coefficient. In addition, the coolant jets disturb the mainstream flow and, therefore, increase the heat transfer downstream the film holes. For the low rotating speed condition, the stagnation line lays on the pressure side, the coolant is pushed to the suction side as shown in Figure 5.10. Therefore, the heat transfer increases on the suction side. For the design condition, the stagnation line falls

in the middle of the two film rows, as a result the heat transfer is enhanced on both pressure and suction side downstream of the film holes. For the high rotating speed condition, the coolant pathlines are shifted to the pressure side due to the stagnation line move to the suction side shown in Figure 5.10. Therefore, the heat transfer increases downstream the film holes on the pressure side.

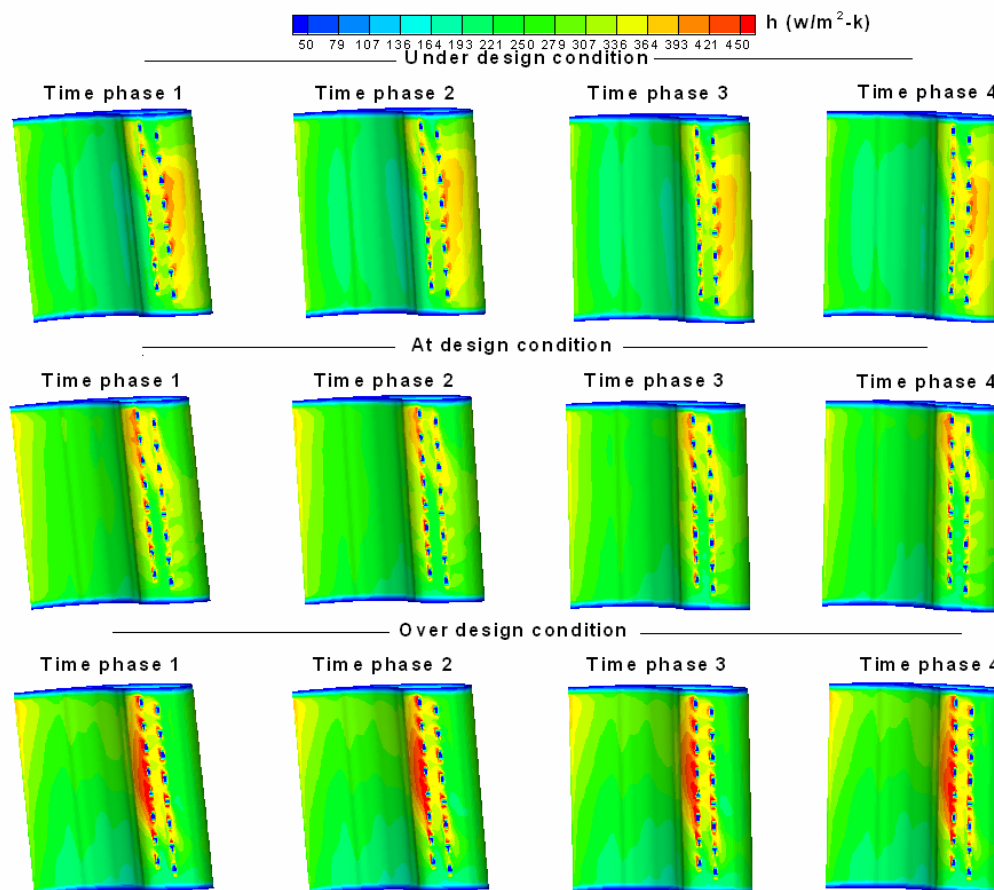


Figure 5.12 Heat transfer coefficient comparison at leading edge of rotor for four time phases with three working conditions, $M=1$.

5.3.3. Film Cooling Effectiveness

The instantaneous film cooling effectiveness for four time phases with three rotating speeds are shown in Figure 5.13. In general, the film cooling effectiveness decreases with increasing rotating speed. Although the high speed rotating decreases the rotor relative inlet velocity, but it creates more unsteady turbulent wake, causes more mixing between coolant and mainstream, and decreases the film cooling effectiveness. For the case of low rpm condition, the tilted stagnation line lays on the pressure side. Therefore, most the coolant from both pressure and suction sides are pushed to the suction side. Some pressure side coolant near the tip region, however, covers the pressure side due to the tilted stagnation line of two-dimensional blade. For the design condition, generally the pressure side row coolant covers the

pressure side, while suction side row protects the suction side; For the high rpm condition, most coolants are shifted to the pressure side due to the stagnation line moving to the suction side. Another interesting finding is that a high film cooling effectiveness exists at the trailing portion of the rotor. This is not due to the film coolant protection from the leading edge. On the contrary, it is due to a low mainstream temperature caused by a high speed compressible flow and work process of turbine.

Figure 5.14 compares the predicted film cooling effectiveness with the experimental data by Ahn et al.[34] using the PSP technique. For simplicity, only the phase 1 results are plotted and compared to the experimental data since the difference among four time phases is not significant. As mentioned earlier, the numerical low-rpm condition of 1800 rpm is different from the experimental 2400 rpm due to the limitation of the turbine rig. It shows that the trend of the cooling coverage and the value of cooling effectiveness match reasonably well between the prediction and experiment. For example, the design condition shows the splitting of coolant to the pressure and suction side, while the high rpm condition shifts the coolant to the pressure side.

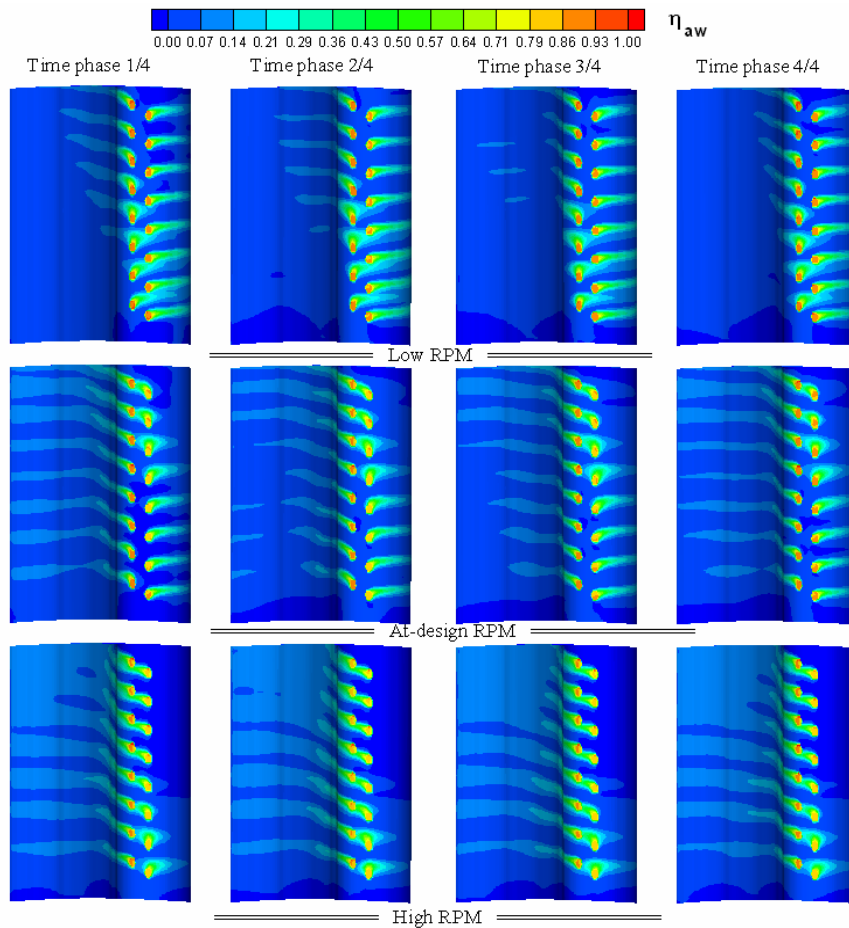


Figure 5.13 Film cooling effectiveness comparison on the rotor blade for four time phases with three working conditions, $M=1$.

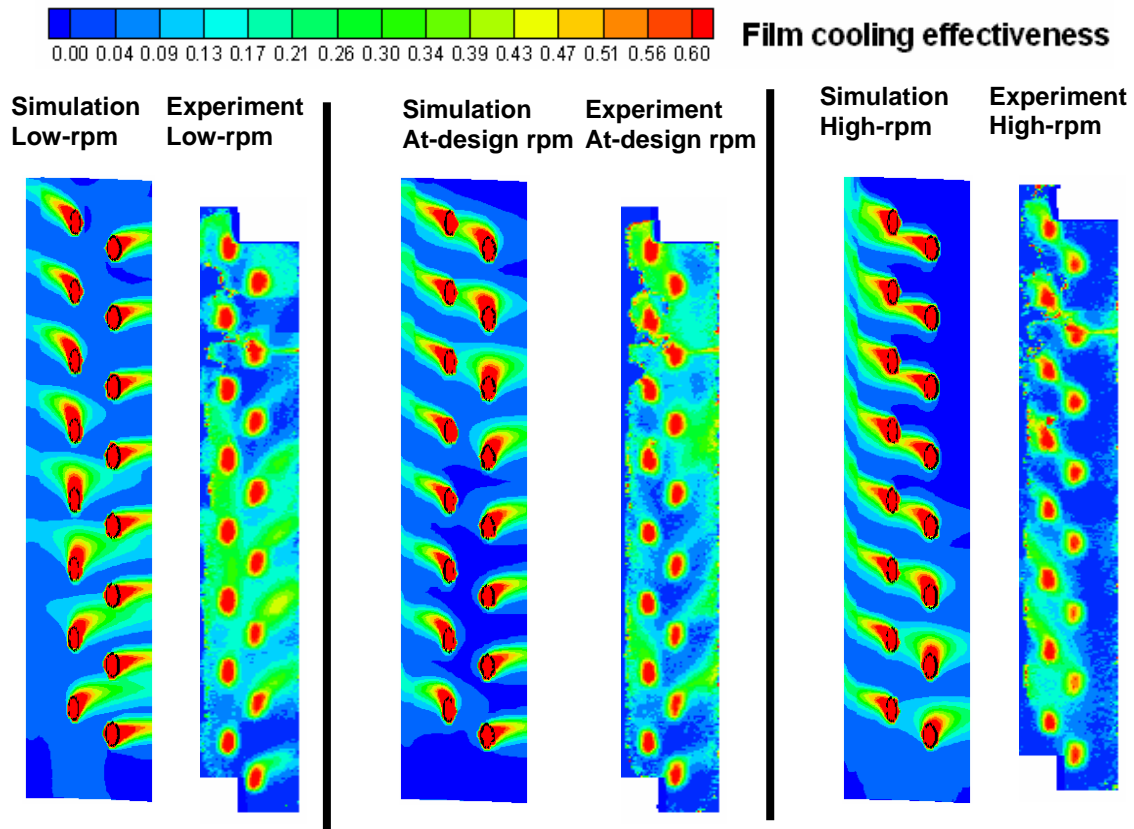


Figure 5.14 Comparison of the predicted (time phase 1) and measured film cooling effectiveness on the leading edge of rotor with three working conditions, $M=1$.

Figure 5.15 shows the comparison of predicted film cooling effectiveness with three blowing ratios for the at-design condition. It's interesting to note that the high blowing ratio reduces the film cooling effectiveness. Since the overall blowing ratio is defined as the coolant jet velocity divided by the rotor absolute inlet velocity as shown in Figure 5.4c. Since V_2 is much higher than the rotor relative inlet velocity W_2 , the real blowing ratio of the rotor is much higher than 1 for the $M=1$ case considered here. When the blowing ratio increases, the actual blowing ratio of rotor increases significantly and the high momentum coolant penetrates the mainstream flow and detaches from the blade surface. Thus, the cooling effectiveness decreases for the higher blowing ratio cases. This predicted film cooling behavior can also be supported by the comparison to the experimental data of Ahn et al.[34]. The difference between experiment and simulation can be attributed to the lack of the grid resolution, or limitation of the turbulence models.

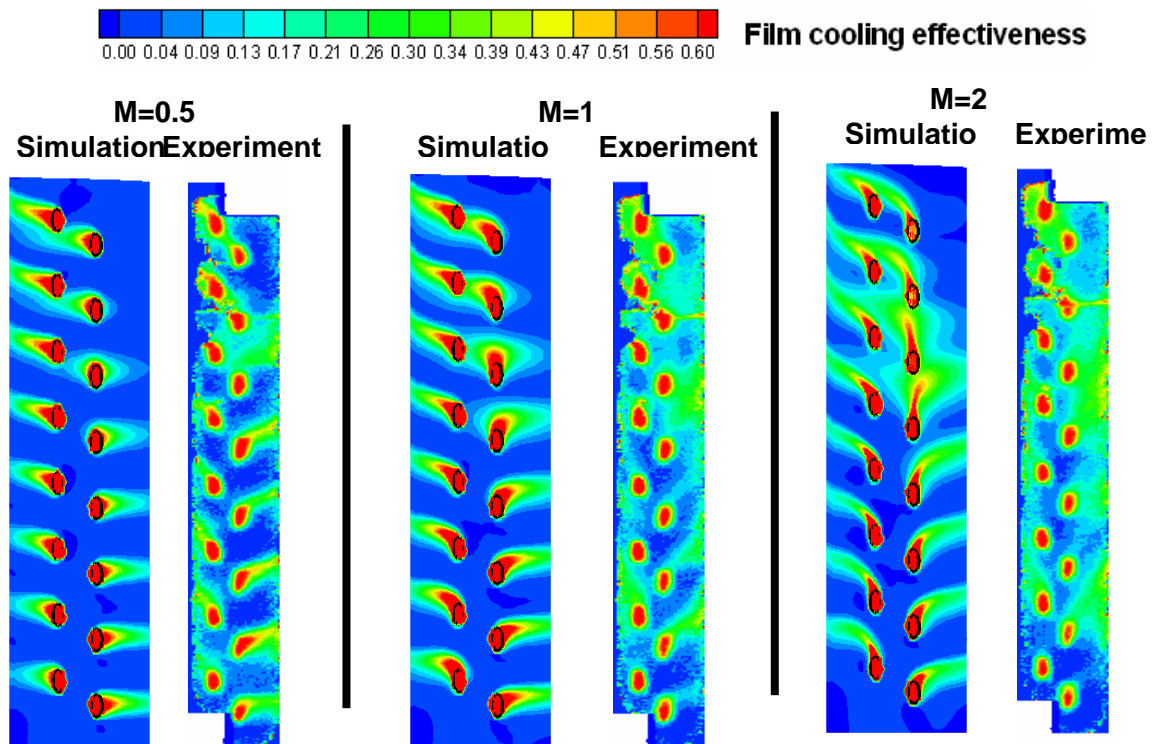


Figure 5.15 Comparison of predicted (time phase 1) and measured film cooling effectiveness on the rotor blade for three blowing ratios, design condition.

5.4. Conclusions of Film Cooling on the Rotor Blade Leading Edge

Numerical simulations were performed for both two-dimensional three turbine stages and three-dimensional 1-½ turbine stage to determine the unsteady film cooling effectiveness and heat transfer coefficients on the leading edge of the first stage rotor blade at design and off-design conditions. The primary findings from this study are summarized as follows:

1) The unsteady intensity of heat transfer coefficient with film cooling is significantly higher than that without film cooling. Because the coolant jet disturbs the mainstream flow, and magnifies the unsteady caused by the rotor interaction.

2) The unsteady intensity of film cooling effectiveness is much higher than that of the heat transfer coefficient, which means the cooling effectiveness is much more sensitive to the rotor interaction than the heat transfer.

3) When the rotating speed increases from the low-rpm condition to the design and high-rpm conditions, the stagnation line on the rotor blade shifts from the pressure side to the leading edge, then to the suction side, respectively due to the increasing incident angle of the rotor relative inlet velocity.

Therefore, the film cooling protection moves from the suction side to the pressure side, so does the increased heat transfer coefficient downstream the film holes.

4) For the two dimensional blade on the present study, the stagnation line is not a simple straight line as the blade leading edge due to the changing of relative velocity incident angle for various span locations. It tilts from the pressure side root region to the suction side tip region.

5) The increasing rotating speed produces more unsteady turbulent wake flow, although it reduces the rotor relative inlet velocity. The overall result increases the heat transfer coefficient, and decreases the film cooling effectiveness on the leading edge region of the rotor blade.

CHAPTER VI

ROTOR BLADE PLATFORM FILM COOLING BY PURGE FLOW

6.1. Problem Definition and Computational Details

The previous chapters have already studied the film cooling on the blade tip and leading edge; therefore, in this chapter, the film cooling on the platform will be numerically investigated. Simon and Piggush [59] have reviewed the most recent development of turbine endwall aerodynamics and heat transfer. Again, as indicated in the chapter I, the corresponding experimental study (Suryanarayanan, et al. [52]) has been carried out on the “state-of-the-art” three stage research turbine facility at the Turbomachinery Performance and Flow Research Laboratory (TPFL) of Texas A&M University. Due to the limitation of the computational resource, the present three-dimensional calculations can only be carried out for the first 1-½ turbine stage, which includes the first-stage stator (stator 1), the first-stage rotor (rotor), and the second-stage stator (stator 2), as shown in Figure 6.1.

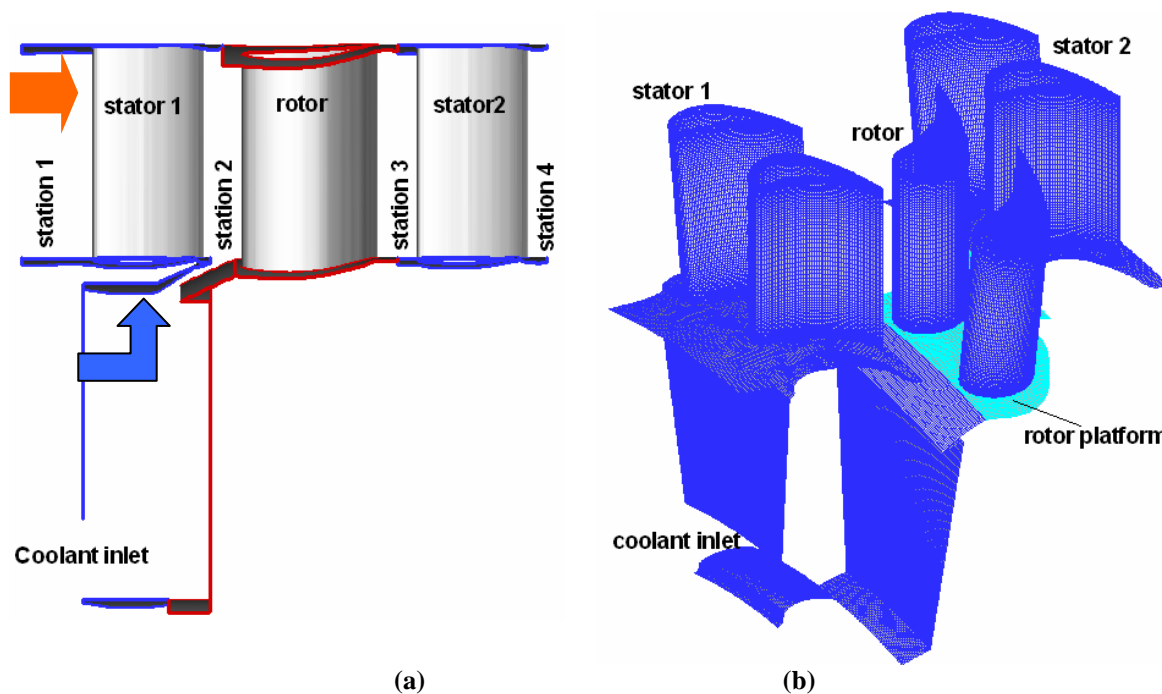


Figure 6.1 (a) Computational domain of slot film cooled platform in a 1-1/2 turbine stage, and (b) numerical grids (repeated two times and the cyan color is the cooled platform).

The film coolant enters the disk cavity of the first stage stator and purges through the angled slot in the hub junction between the first-stage stator and the rotor to form a film cooling sheet to protect the rotating platform as shown in Figure 6.1(a). The portion outlined by blue color is non-rotating, including

stator 1, disk cavity of stator 1 and stator 2; while the red color denotes the rotating domain, such as the rotor and its disk cavity. The horizontal width of the slot is 7 mm with 25 degree inclined angle to the rotor platform. The slot length is 16.5 mm and the slot bottom is connected to both the stator 1 and the rotor disk cavity. The length of the disk cavity for stator 1 is 25.4 mm (1 inch), and 12.7 mm (0.5 inch) for the rotor. The height of the disk cavity is 144.8 mm (5.7 inch). Only the rotor platform is film cooled in the present study. The blade height is 63.5 mm (2.5 inch), the root diameter is 558.8 mm (22 inch), and the shroud diameter is 685.8 mm (27 inch). Both the stator and rotor blades are two-dimensional with the same blade profiles in the spanwise direction. The present blade profiles are exactly the same as the experimental blades used by Suryanarayanan et al.[50]. In their experiment, there are 58 stator 1 blades, 46 rotor blades and 52 stator 2 blades. To simulate the experimental conditions exactly, it is necessary to use 29 first-stage stator blades, 23 rotor blades and 26 second-stage stator blades with periodic boundary conditions along the circumferential direction. In order to significantly reduce the computer memory and CPU time requirements, it is desirable to use the same number of blades for both the rotor and stators in the 1- ½ turbine stage. This enables us to simulate only one flow passage with periodic boundary conditions in the circumferential direction. Since this paper focuses on the film cooling on the rotor platform, it is reasonable to simplify the turbine stage by using 46 blades for both the first- and second-stage stators while maintaining the correct number of rotor blades as shown in Figure 6.1(b). Additional information of the turbine rig and two-dimensional blades can be found in Schobeiri et al. [55-56].

The simulations were performed using the CFD software package Fluent. The solutions are obtained by solving the compressible Reynolds-Averaged Navier-Stokes (RANS) equations together with a Reynolds stress model (RSM) using a finite volume method to discretize the continuity, momentum and energy equations. The GAMBIT software with Turbo function was used to generate the unstructured grids. The computational domain consists of fluid around the stator 1 and its disk cavity, film cooled rotor platform and its disk cavity, and stator 2 with periodic boundary conditions imposed in the circumferential direction as shown in Figure 6.1. The computational domain is composed entirely of the hexahedral cells, which are more accurate with less numerical diffusion. An interface technique was used to handle the information exchanged between stators and rotor since the sliding meshes were used for the rotor domain. Relatively coarse grids are used for the majority of the 1-½ turbine stage, while the angled film (purge) slot, the platform of rotor, and the boundary layer of the stator and rotor blades consist of much finer grids for accurate resolution of the film cooling effectiveness and heat transfer. The $y^* = \rho C_{\mu}^{1/4} k_p^{1/2} y_p / \mu$ value for the non-equilibrium wall function falls between 30 and 100 for most of the regions, where k is the turbulent kinetic energy and the subscript p denotes the near-wall grid point. The geometry and detailed numerical grids around the coolant slot and rotor platform are shown in Figure 6.2.

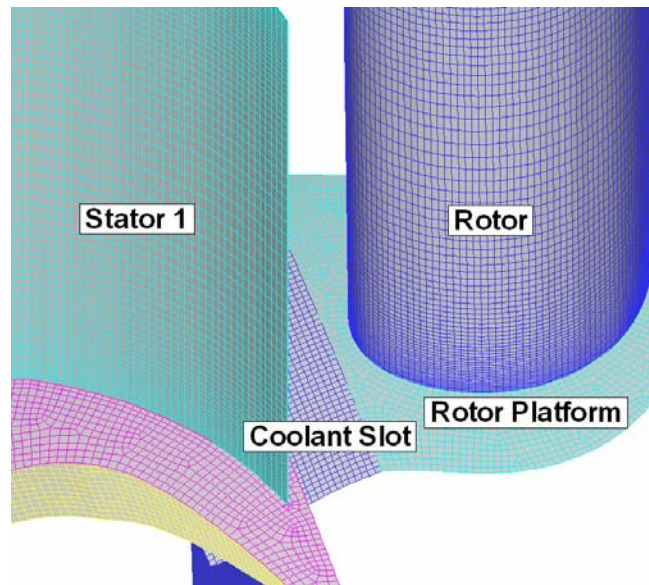


Figure 6. 2. Detailed grid distributions near the angled coolant slot.

Calculations were performed for four different rotating speeds of 2000, 2550, 3000 and 4000 rpm, where 3000 rpm is the design point for the highest turbine efficiency in this study. The inlet total and exit static pressures of the turbine stage are $P_{in} = 101,356$ Pa and $P_{ex} = 85$ kPa, respectively, with a pressure ratio of 1.19. At the inlet of the first stage stator, the total temperature (325 K) and turbulence intensity (5%) are specified with an inlet flow angle of 0 degree.

The absolute velocity at the stator 1 inlet is about 30 m/s. A fixed mass flow rate boundary condition is specified at the inlet of the coolant cavity as shown in Figure 6.1(a), with temperature 300K and overall mass flow ratios $MFR = 0.5\%$, 1% , and 1.5% , which correspond to blowing ratios of $M = 0.12$, 0.24 and 0.36 , respectively.

In this paper, three sets of calculations with different thermal boundary conditions were performed to evaluate the adiabatic film cooling effectiveness (η_{aw}) and the heat transfer coefficient (h_{aw}). For the calculation of adiabatic film cooling effectiveness $\eta_{aw} = (T_{aw,0} - T_{aw,f}) / (T_{aw,0} - T_{tc})$, the turbine inlet total temperature is specified at $T_{to} = 325$ K and the coolant total temperature is $T_{tc} = 300$ K. The adiabatic wall boundary condition is used for the platform and blades to obtain $T_{aw,f}$. It should be noted that $T_{aw,f}$ includes not only the effects of film cooling, but also the temperature change due to turbine work process. In order to determine the true film cooling effectiveness without the complication caused by turbine work process, it is necessary to calculate another adiabatic wall temperature $T_{aw,0}$ for the same blade configurations in the absence film coolant injection. This enables us to achieve the true effect of coolant protection by comparing the temperature differences with and without the presence of purged coolant.

For the calculation of heat transfer coefficient, the coolant total temperature is the same as the turbine inlet total temperature 325 K, while the wall temperature is fixed as 300 K to get q_w . As discussed before,

to achieve the true heat transfer coefficient which is only based on the flow field, the $h_{aw} = q_w / (T_w - T_{aw,o})$ needs to be applied, where the reference temperature, $T_{aw,o}$, isolates the turbine work process. In addition, the overall heat transfer coefficient, $h = q_w / (T_w - T_{to})$ has been reported, including the effects of both turbine work and flow field.

All calculations were converged to residual levels of the order of 10^{-5} , and to less than 0.1% error in the mass flow rate between the turbine mainstream and coolant inlet and outlet of the computational domain. The passing period, T , is defined as the time it takes for the rotor blade to move from one stator to another. The selection of the time step in calculating one passing period of the rotor blade is critical for accurate time-dependent flow predictions. Our previous study shows that the difference between 100 and 200 time steps is below 3%. Therefore, 200 time steps reach the time-step independency, and are used in these simulations. The computed results are recorded and analyzed once every 50 time steps (i.e., every 1/4 passing period). To achieve good periodic results, simulations were performed for 10 passing periods and the numerical results were presented at four different time phases with $t/T = 9/4, 9/2, 9/4, \text{ and } 10$, respectively. The present simulations are computationally intensive since they involve unsteady three-dimensional flow with a sliding rotor mesh. Each simulation was performed using the parallel version of Fluent on two processors, and requires about two weeks of CPU time on the SGI Altix 3700 supercomputer at Texas A&M University. A total of seven simulations were performed to determine the film cooling effectiveness and heat transfer coefficients for the 2000, 2550, 3000 and 4000 rpm, respectively.

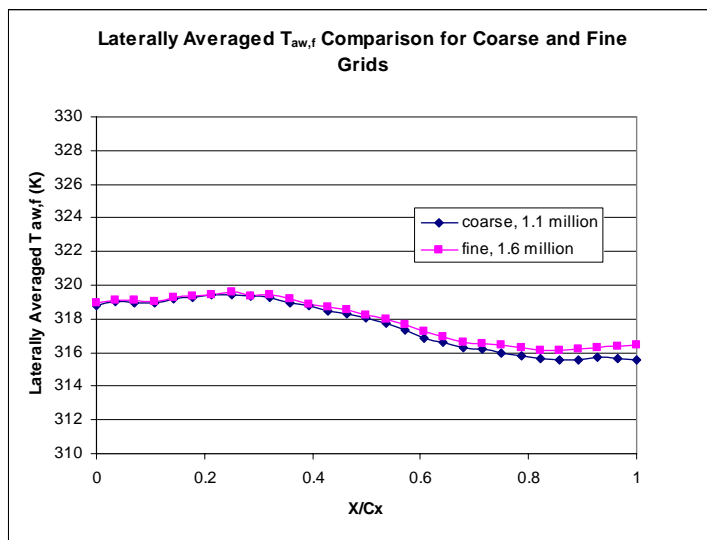
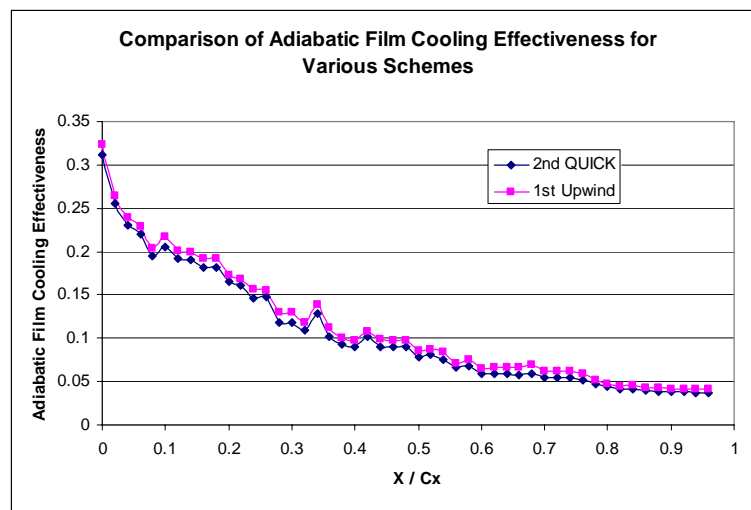


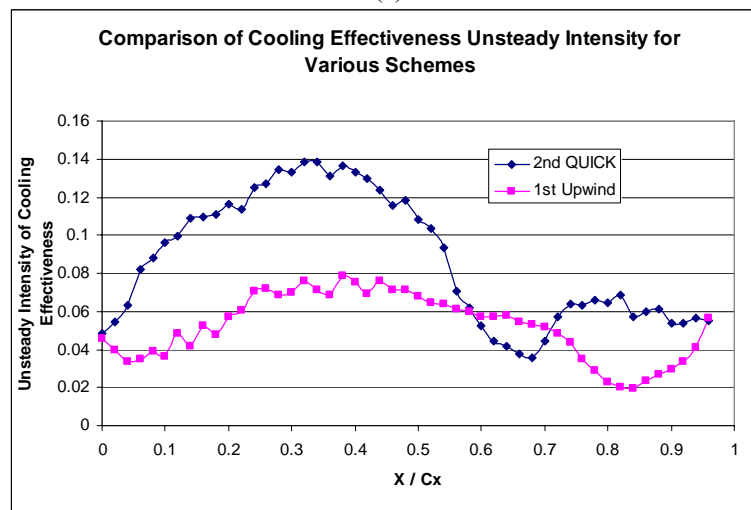
Figure 6.3 Grid refinement study for laterally averaged adiabatic temperature on rotating blade platform.

Figure 6.3 shows the predicted laterally averaged $T_{aw,f}$ for the rotating blade platform using two different numerical grids. The coarse grid consists of about 1.1 million elements with 0.3 million cells for

the stator-1 domain, 0.5 million cells for the rotor domain, and 0.3 million cells for the stator-2 domain. For the fine grid case, the number of numerical elements for the rotor domain was doubled to about 1 million cells. It is seen from Figure 6.3 that the maximum change in the laterally averaged $T_{aw,f}$ is less than 0.83 K, corresponding the error about 0.26%. In addition the grid independency study, the comparison of 1st order upwind and 2nd order QUICK scheme has been plotted in Figure 6.4. The laterally averaged cooling effectiveness shows a small difference between these two schemes in Figure 6.4(a), while unsteady intensity demonstrates a huge difference in Figure 6.4(b). Because the 1st order upwind scheme inherently has numerical diffusion, and dilutes the unsteady fluctuation. All the numerical results presented in this paper were obtained based on the fine grid with QUICK scheme.



(a)



(b)

Figure 6.4 Scheme comparison for laterally averaged adiabatic film cooling effectiveness (a) and cooling effectiveness unsteady intensity, 2550 rpm, MFR=1% ($M=0.24$).

6.2. Flow Structure Study

Figure 6.5 shows a vertical cross section plane and the corresponding streamlines and dimensionless temperature (ϕ) contours for the film cooled platform with the purged coolant slot. Note that the domain on the right hand side of the white vertical line is rotating, while the left hand side solution domain is non-rotating. Due to the rotating centrifugal force, the fluid in the right hand side of the disk cavity is rotating in counter-clockwise direction and driven radically outward. The centrifugal force pushed (purged) the coolant out of the disk cavity through the inclined coolant slot into the rotor blade passage. It is interesting to note that there is a small circulation region near the slot entrance due to the sharp turn between the disk cavity and the coolant slot. In addition, some mainstream flow was entrained into the coolant slot as seen from the relatively low temperature fluid near the slot exit. It should also be noted that the coolant flow in the slot is highly three-dimensional with significant variations in the circumferential directions.

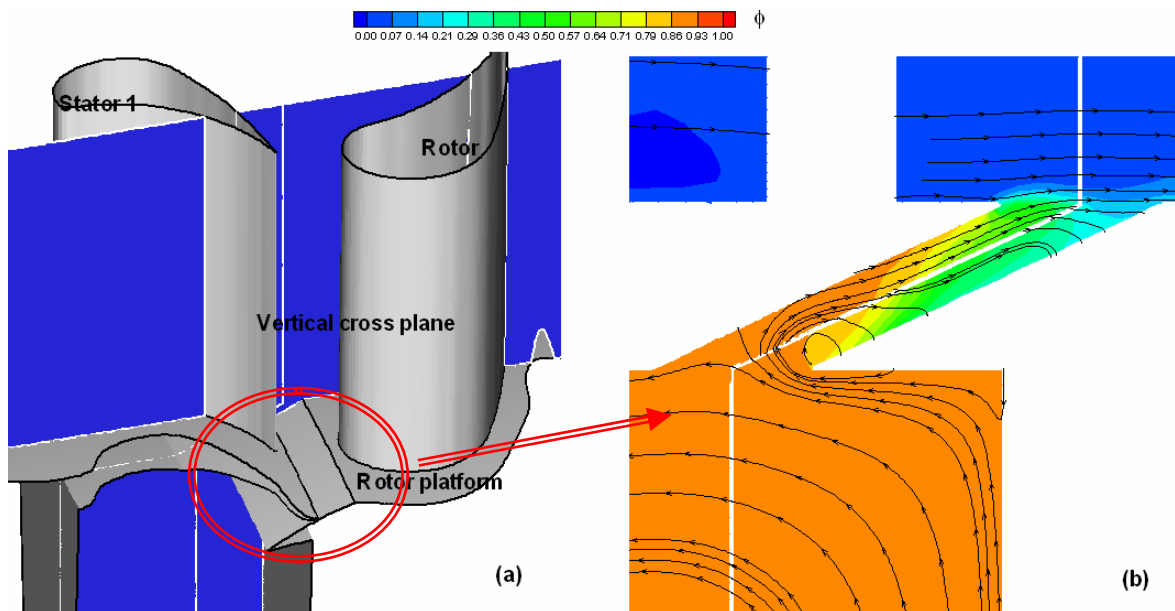


Figure 6.5 (a) Vertical cross section plane and (b) the corresponding dimensionless temperature contours and streamlines, 2550 rpm, MFR=0.5% ($M=0.12$).

Figure 6.6 shows the conceptual rotor inlet velocity triangle and relative inflow angle to the rotor. Our previous studies (Yang 2004, 2005) show that the rotor absolute inlet velocity V_2 mostly depends on the turbine inlet/outlet pressure ratio, while rotor relative velocity W_2 changes with the rotating speed U_2 . When the rotating speed U_2 increases from the low-rpm condition (blue color) to the intermediate-rpm condition (red color), and then the high-rpm condition (green color), the magnitude and the flow angle (β_2) for the relative velocity W_2 decrease as shown in Figure 5.6(a). Correspondingly, the stagnation points on

the rotor leading portion shifts gradually from the pressure side (denoted by the blue color) to the suction side (green color), while the inflow angle changed significantly as shown in Figure 5.6(b).

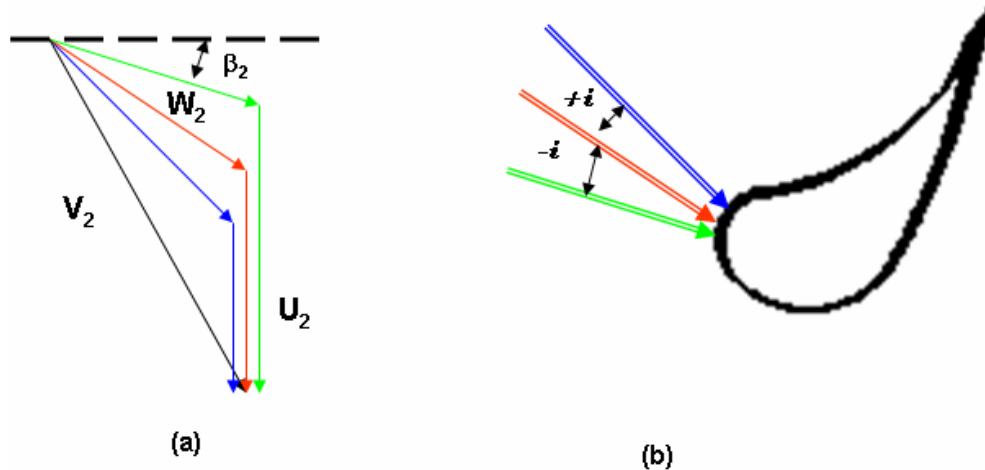


Figure 6.6 (a) Conceptual rotor inlet velocity triangle and (b) relative velocity incidence angle to the rotor leading edge for various working conditions.

Besides the flow pattern in the vertical cross plane in Figure 6.5, an annular (constant radius) cross plane is also shown in Figure 6.7 to provide a better understanding of the pressure and flow fields for various rotating speeds. This annular plane is located at 2% of the blade span away from the hub and parallel to the platform. As mentioned earlier, the increasing rotating speed slightly shifts the stagnation point from the pressure side to the suction side direction with a dramatic change in inflow angle. Figure 6.7(a) compares the pressure ratio ($P_{\text{static, local}}/P_{\infty, t}$) on the annular cross plane. For the 2000 rpm condition, the high pressure region was observed on the pressure side of the leading portion due to the flow impingement in that region. The stagnation point gradually shifts from the pressure side to the leading edge direction with increasing rpm to 2550. When the rotating speed was further increased to the 3000 rpm conditions, the high pressure stagnation region was moved to the leading edge of the best performance point. However, the 4000 rpm shifts the stagnation point to the suction side. Figure 6.7(b) compares the streamlines and dimensionless temperature contours for various rotating speeds. For the 2000 and 2550 rpm condition, the dividing streamline impinges on the pressure side with a positive inflow angle. The coolant from the inclined slot can be clearly detected by the high value dimensionless temperature (φ) near the leading portion. The coolant is pushed away from the blade leading portion suction side by the positive incidence angle flow. For the 3000 rpm condition, the stagnation point shifts to the leading edge of best performance and the coolant is converged near to the blade suction side. However, the coolant does not adhere to the suction side due to the presence of horseshoe vortex along the blade-hub junction. For the 4000 rpm condition, the rotor inlet flow angle switches to negative and the stagnation

point is shifted to the suction side. Generally, the streamlines move parallel to the blade pressure side, but converged on the suction side due to the passage vortex. The high value of ϕ on the rotor trailing portion is not due to the coolant protection. It is, in fact, due to the turbine work process since the mainstream total temperature decreases significantly along the flow direction.

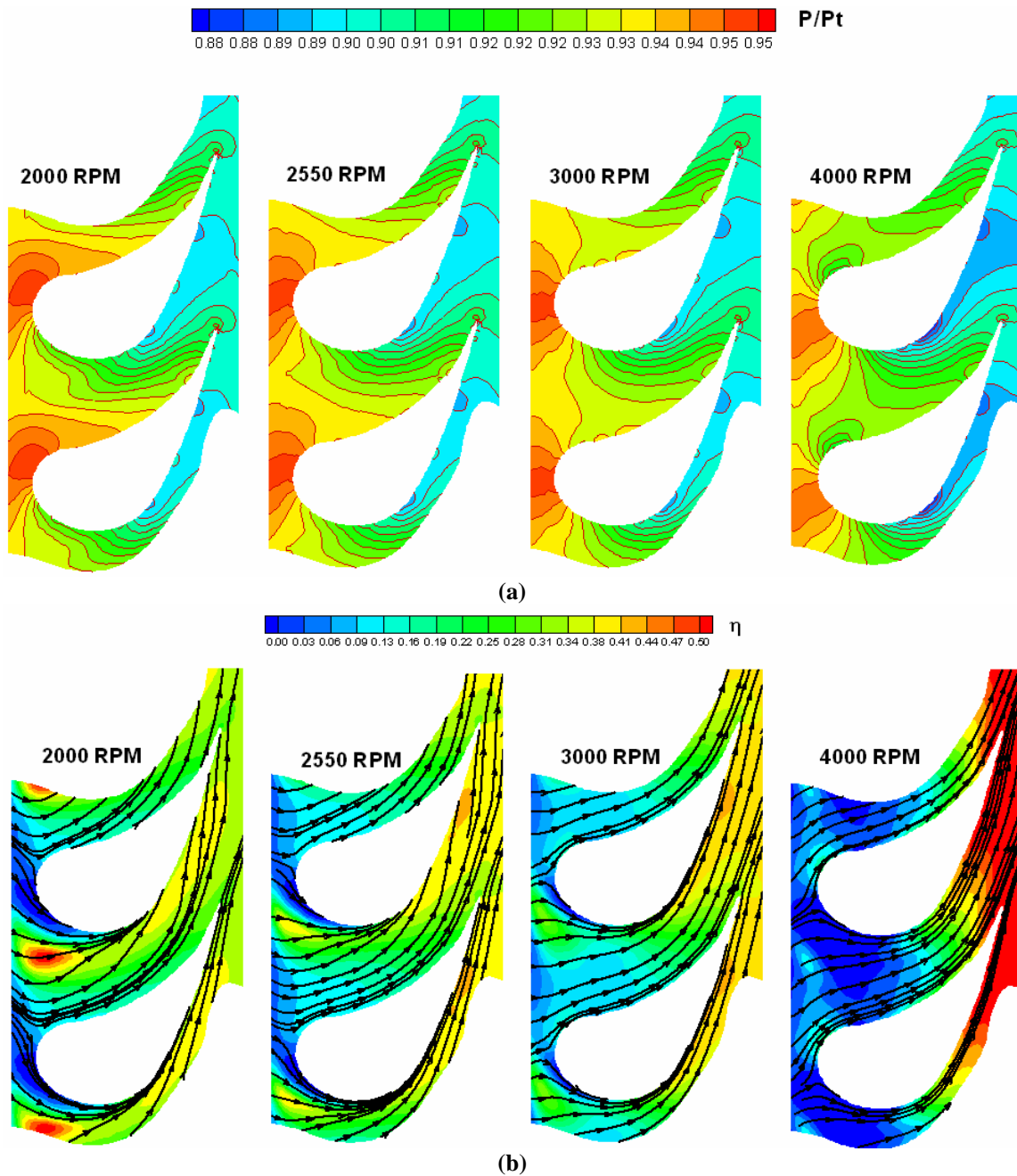


Figure 6.7 Comparison of (a) pressure ratio and (b) streamlines and dimensionless temperature contour on the annular cross plane for various working conditions, time phase $\frac{1}{4}$.

Figure 6.8 shows a comparison of the static pressure contours around the rotor blade hub region with and without film cooling. For the non-film-cooled blade shown in Figure 6.8(a), a low static pressure region is seen on the suction side rotor region. On the other hand, a higher pressure region was observed on the suction side root region for the film-cooled blade shown in Figure 6.8(b) since the purged coolant from the angled slot was pushed towards the suction side of the rotor blade. It is also worthwhile to note that the effect of the purged coolant is confined to the root region.

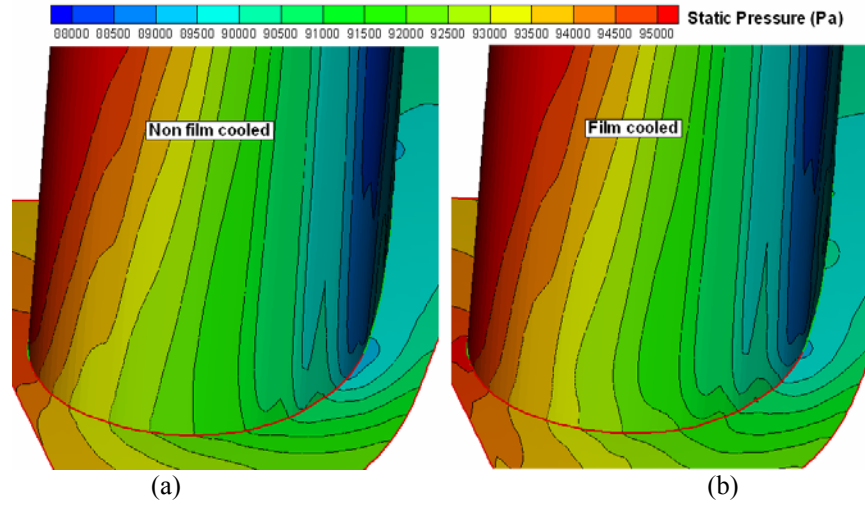


Figure 6.8 Comparison of static pressure contours on the rotor blade hub region: (a) without purge flow and (b) with purge flow; 2550 rpm, time phase $\frac{1}{4}$, MFR=1% ($M=0.24$).

6.3. Adiabatic Film Cooling Effectiveness Study

Figure 6.9 compares the adiabatic total wall temperature on the rotating blade platform with and without film coolant to facilitate a direct evaluation of the true film cooling effectiveness. It is quite clear that the adiabatic wall temperature around the leading edge region is significantly lower for the film cooling case shown in Figure 6.9(a) as a result of purged coolant protection. In the trailing edge section of the blade passage, however, both blade configurations show a significant decrease in the adiabatic wall temperatures either with or without film coolant protection. As noted earlier, the reduction of the adiabatic total temperature in the trailing edge region is due to the turbine work process rather than the coolant protection.

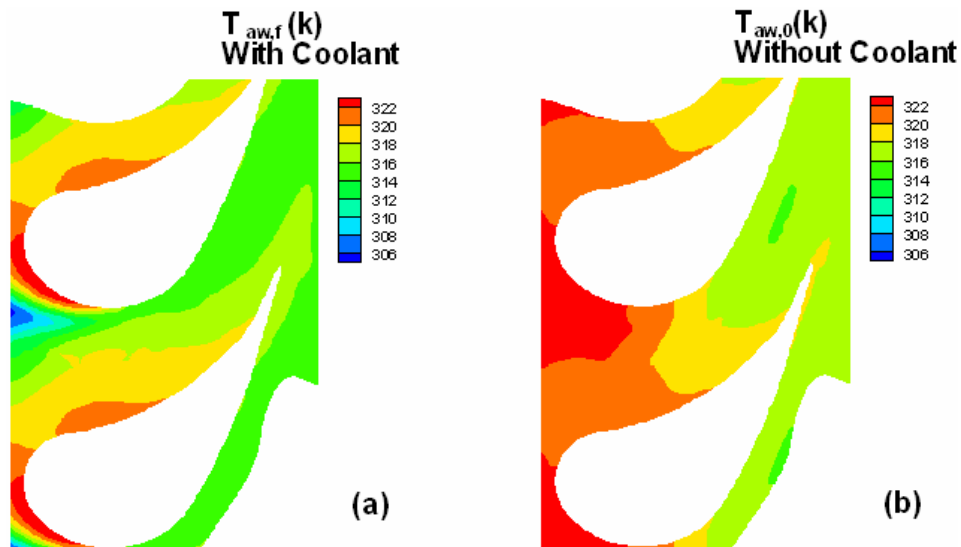


Figure 6.9 Adiabatic total wall temperature comparison with and without purge flow on the rotating blade platform, time phase $\frac{1}{4}$, MFR=1% ($M=0.24$).

Figure 6.10 compares the instantaneous adiabatic cooling effectiveness for various rotating speeds. Note that the 4000 rpm has been re-plotted at bottom with a small color level for a better reading. Generally speaking, the cooling effectiveness decreases along the passage flow due to the mixture with the turbine passage mainstream flow, and separates from the leading portion suction side because of the horseshoe vortex there. The protection area shapes as a curve triangle and accumulates near the suction side due to the low pressure. For the low rpm cases (2000 and 2550 rpm cases), the coolant is pushed away from the suction side due to the positive inlet flow angle of rotor. The difference of effectiveness for the various time phases is not significant, because the rotor-stator interaction is weak for such low rotating speeds; and the wake and turbulence intensity is not strong enough to affect the purged coolant flow distribution on the rotor platform. For the high rpm cases (3000 and 4000 rpm), however, the coolant is pushed towards the blade suction side because of decreasing inlet flow angle shown in Figure 6.7(b). The cooling effectiveness shows a significant difference among various time phases. This maybe attributed to: 1) the high rpm increases the rotor-stator interaction affect; 2) high turbulence and high wake are introduced by the increased rpm; and 3) more chaos, especially for the 4000 rpm case, are produced by the high rotating speed.

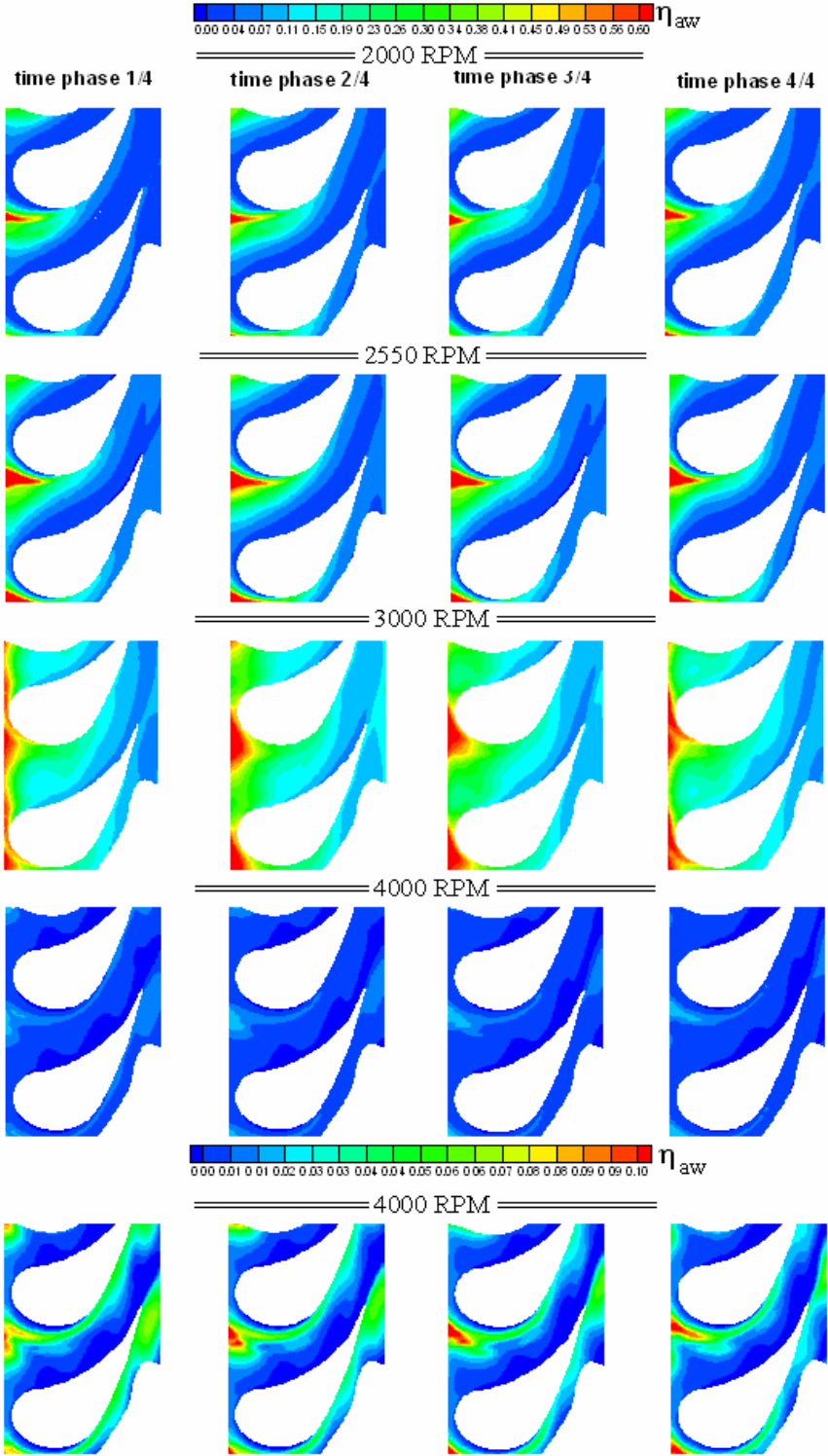
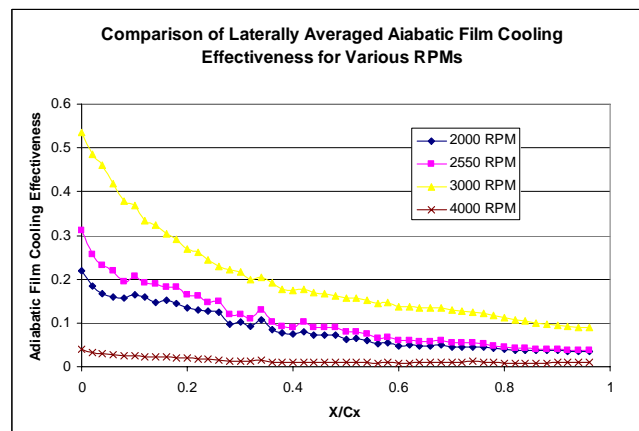


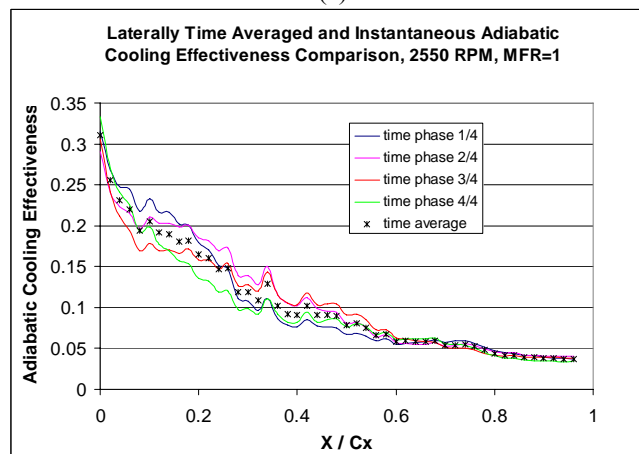
Figure 6.10 Comparison of adiabatic film cooling effectiveness on the rotating blade platform for various time phases and rpm, MFR=1%, (M=0.24).

Figure 6.11 compares the laterally averaged cooling effectiveness and unsteady intensity on the rotating platform. The laterally averaged adiabatic cooling effectiveness has been compared in Figure 6.11(a) for various rotating speeds with MFR=1% (M=0.24). As discussed before, the film cooling decreases along the turbine passage flow direction. Also the effectiveness increases with increasing rpm from 2000, 2550 to 3000, since 3000 rpm is the best performance point. Then it dramatically decreases for 4000 rpm case due to the over-design condition. The instantaneous and time averaged adiabatic cooling effectiveness has been plotted in Figure 6.11(b) for 2500 rpm condition with MFR=1%. Clearly to see that the fluctuation of cooling effectiveness increase from the leading edge to the middle chord of the blade, then decreases at the trailing portion. Therefore, it is desirable to quantitatively study the unsteady characteristics of the film cooling effectiveness by defining a cooling effectiveness unsteady intensity $\sqrt{\frac{\sum(\eta-\bar{\eta})^2}{N}}/\bar{\eta}$ with Root Mean Square (RMS) method, a similar concept of turbulence intensity. Figure 6.11(c) shows the comparison of cooling effectiveness unsteady intensity for various rotating speeds. Generally, the off-design conditions increase the unsteady intensity. For the 2000 rpm case, the unsteady intensity increases from the leading edge to the peak value of 22% at the location x/C_x of 0.6. With rpm increasing to 2550 rpm, which is more close to the best performance condition, the intensity decreases to the peak value of 15% and locates at the x/C_x of 0.38. The rpm is further increased to the best performance condition of 3000, the unsteady intensity is further reduced, and the peak value is about 12% with location at x/C_x 0.22. The best performance working condition streamlined the passage flow, and thus damped the unsteady fluctuation. The shifting of the intensity peak from the mid-chord of blade to the leading portion with increasing rpm can be attributed to the changing of inlet flow angle of rotor as shown in Figure 6.7(b). The 4000 rpm, however, dramatically increases the intensity and produced a lot of chaos, especially on the passage trailing portion. Since this flow is out of control for such high rpm off-design condition.

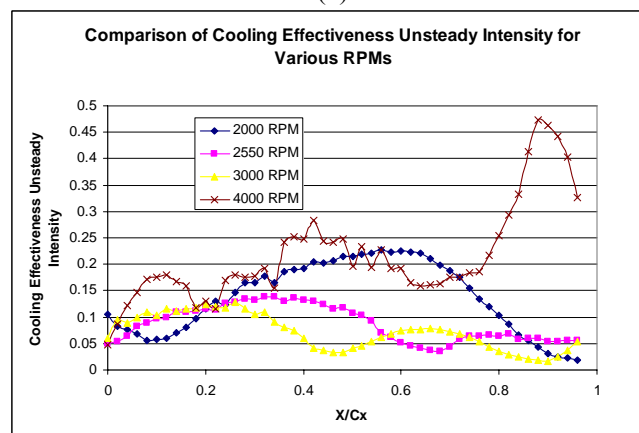
Figure 6.12 compares the calculated and measured (Suryanarayanan et al. [52]) adiabatic cooling effectiveness for various mass flow ratios (MFRs) for the 2550 rpm condition. Both the simulation and experiment indicate that the film cooling effectiveness as well as the area of coolant protection increase with increasing mass flow ratio and accumulate near the suction side. All simulations show that the film cooling covers a wide area when existing from the slot, but contracts gradually downstream and adheres to the blade suction side to form a curved triangle region of high effectiveness. In the leading edge portion of the blade passage, the coolant was pushed away from the blade root region by the horseshoe vortex. The experiment (Suryanarayanan et al.[52]), however, shows that the film cooling is more uniform in the passage and adheres to the platform leading edge region. In addition, the reattachment of film coolant near the platform leading edge region was also observed in the experiment for the high mass flow ratio (MFR = 1.5%) case. The failure of prediction can be attributed to the turbulence model, or non-developed swirling flow inside the rotating cavity.



(a)



(b)



(c)

Figure 6.11 (a) Laterally averaged adiabatic cooling effectiveness comparison for various rpms with MFR=1%; (b) Instantaneous and time averaged adiabatic film cooling effectiveness for 2550 rpm, MFR=1% ($M=0.24$); (c) Laterally averaged unsteady intensity of adiabatic cooling effectiveness for various rpms, MFR=1%, ($M=0.24$).

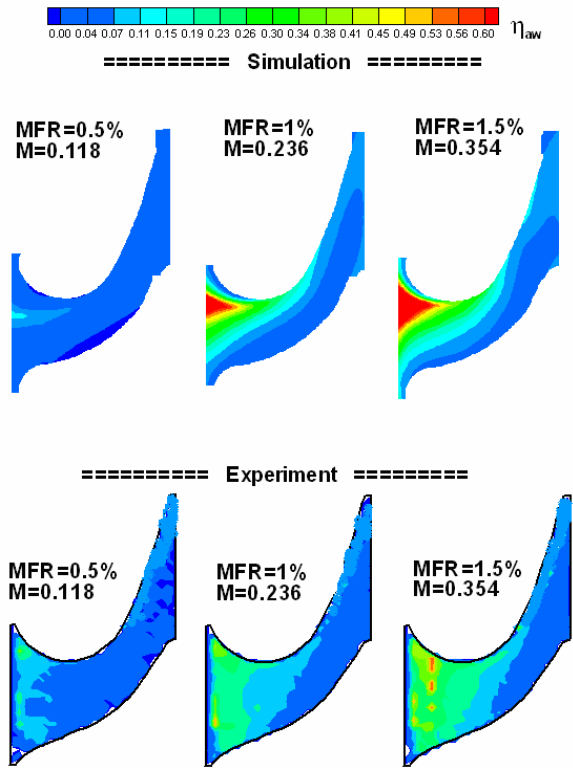


Figure 6.12 Adiabatic film cooling effectiveness comparison on the rotating blade platform between simulation and experiment for various MFRs, 2550 rpm.

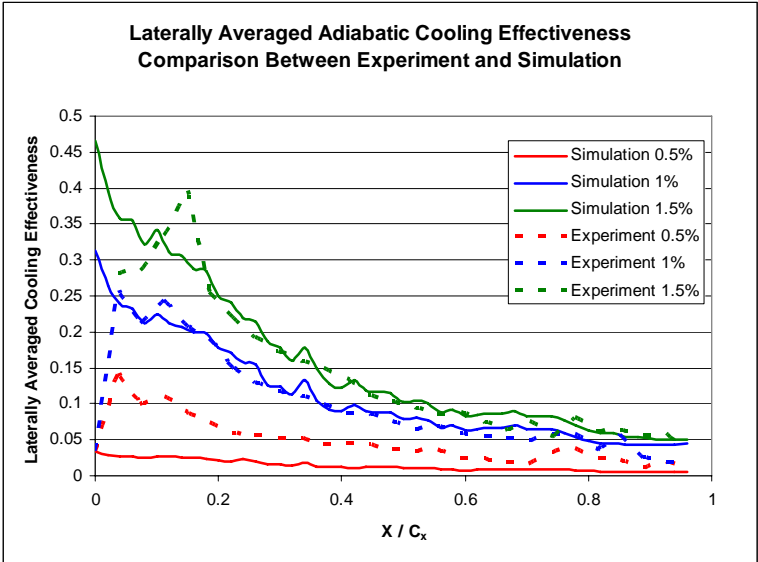


Figure 6.13 Laterally averaged adiabatic cooling effectiveness comparison between simulation and experiment for various MFRs, 2550 rpm.

Figure 6.13 shows a comparison of the calculated and measured (Suryanarayanan et al. [52]) laterally average adiabatic film cooling effectiveness for various mass flow ratios. Except for the leading edge portion, the predictions are in good agreement with the experiment data for the middle and high mass flow ratio cases. The experiment, however, shows some coolant reattachments in the leading edge portion, which was not predicted in the present simulations. Also, the simulation underpredicts the film cooling effectiveness for the MFR=0.5% case.

Figure 6.14 compares the simulated and measured (Suryanarayanan et al.[52]) laterally averaged adiabatic film cooling effectiveness on the rotating blade platform for various rotating speeds. Both the experiment and simulations indicated that the film cooling effectiveness increases with increasing rotating speed for the range considered. For the 2550 rpm case, the predicted adiabatic film cooling effectiveness is in good agreement with the corresponding measurement except for the leading edge region. However, the film cooling effectiveness is overpredicted for the 2000 rpm case. Another interested fact is that the simulation shows a similar trend for these two rotating speeds, while experiment demonstrates a total different trend in the leading portion.

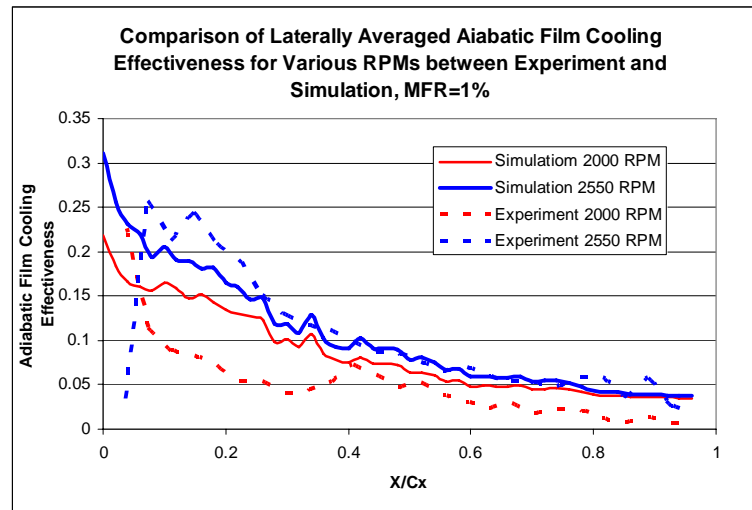


Figure 6.14 Laterally averaged adiabatic film cooling effectiveness comparison between simulation and experiment on the rotating blade platform for various rotating speeds, MFR=1% (M=0.24).

Figure 6.15 shows a comparison of the adiabatic film cooling effectiveness on the blade suction side for various rotating speeds with MFR = 1%. The experimental data on the suction side is not available for comparison at this moment. In general, the coolant jet from the slot gap not only protects the rotating platform, but also benefits the root region of the rotor blade suction side. A high effectiveness strip, extending from the leading edge to the trailing edge, is observed on the suction side. The cooling effectiveness increases with increasing rpm until 3000 rpm of the best performance condition, then drops significantly for the 4000 rpm of over-design condition.

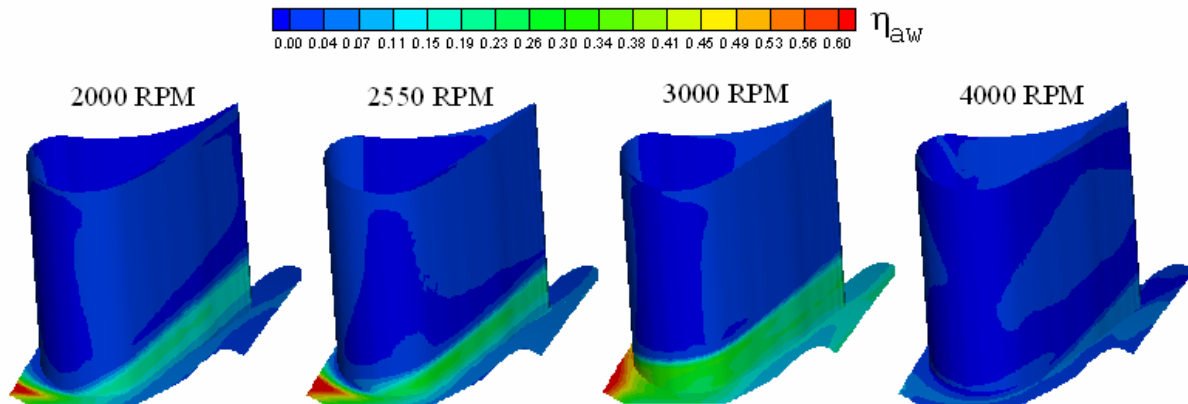


Figure 6.15 Adiabatic film cooling effectiveness comparison on the rotor blade suction side for various rotating speeds, time phase $\frac{1}{4}$, MFR=1% ($M=0.24$).

6.4. Heat Transfer Study

Figure 6.16 compares the overall heat transfer coefficient and heat transfer coefficient on the rotating blade platform at various time phases for the 2550 rpm condition with MFR = 0.5%. The overall heat transfer coefficient is based on the turbine stage inlet total temperature, which is widely used in the industry due to the simple. Thus it includes the effect of both turbine work process and flow field. While the heat transfer coefficient is referred to the local adiabatic total temperature, which can isolate the effect of turbine work process as discussed before, therefore this heat transfer coefficient only depends on the flow field. For both kinds of heat transfer coefficient, a high heat transfer coefficient exists at the rotor leading edge root region due to the horseshoe vortex. A high heat transfer strip develops on the trailing passage portion because of the accelerated high velocity flow and the passage vortex. Also, there is a low heat transfer region downstream of the rotor trailing edge due to the low velocity in the wake. The unsteady characteristic of both heat transfer coefficient is explicitly, especially for the overall one. It's also worthwhile to note that a low heat transfer coefficient in curve triangle shape exists downstream the coolant slot, this can be attributed to the low velocity coolant blockage. The heat transfer coefficient (Figure 6.16b) shows a higher value compared with the overall heat transfer coefficient (Figure 6.16a), especially on the trailing passage portion. Because the adiabatic total temperature decreases along the passage flow direction due to the turbine work process, the driving temperature difference of heat transfer coefficient decreases too.

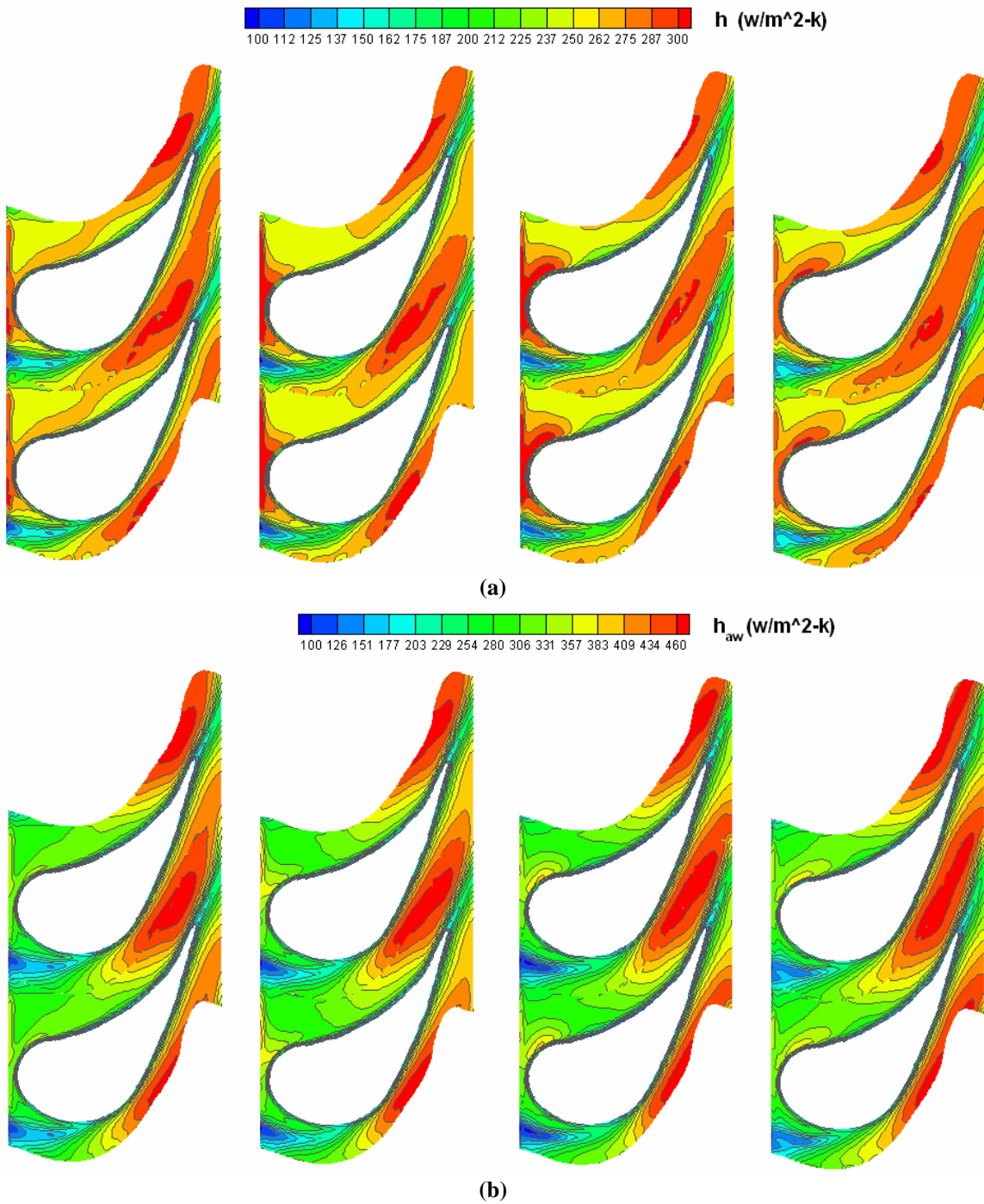


Figure 6.16 Overall heat transfer coefficient and heat transfer coefficient comparison on the rotating platform for various time phases, 2550 rpm, MFR=0.5% (M=0.12).

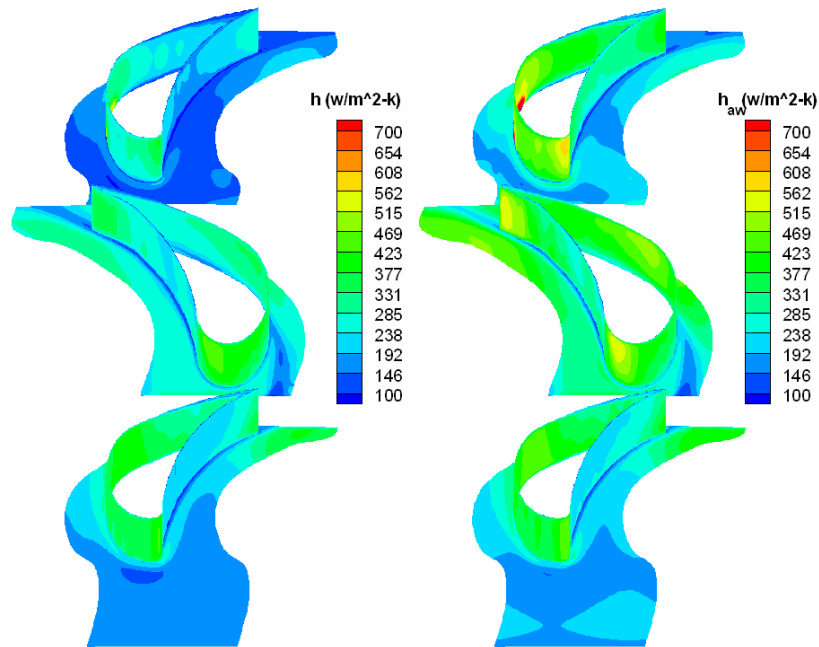


Figure 6.17 Overall heat transfer coefficient and heat transfer coefficient comparison for the whole turbine stage, 2550 rpm, time phase $\frac{1}{4}$, MFR=0.5% ($M=0.12$).

Figure 6.17 compares the overall heat transfer coefficient and heat transfer coefficient for the whole turbine stage. Similar as discussed before, the heat transfer coefficient demonstrates a higher value than the overall one because of the turbine work process, especially for the downstream location of the turbine due to the turbine work process, such as rotor and stator 2. In that location, the dramatically dropping of the adiabatic total temperature happens, which will be further discussed in the later section. Also for each stator and rotor blade endwalls, both the overall heat transfer coefficient and heat transfer coefficient increase from the leading edge to the trailing edge due to the flow acceleration by the blades, which are confirmed by experiment measurement of Harasgama and Burton [39-40].

6.5. Turbine Work Process Impacting on Film Cooling Effectiveness

Figure 6.18 shows the area averaged total and static temperature at various stations in the 1-1/2 turbine stage. The four station positions have been denoted in Figure 6.1(a). Turbine is a rotating machine, which extracts the total energy from the hot gas and transfers it into the mechanical energy by the rotating blades. Due to the turbine work process, it is seen that the total energy decreases significantly from station 2 to station 3, where the rotor converts the thermal energy into the mechanical energy. On the other hand, the total energy remains the same across the stators, such as from station 1 to station 2 (position of stator 1), and from station 3 to the station 4 (position of stator 2). The static temperature, however, changed significantly for each station, even for the stators. Because the flow is accelerated

through the blades to achieve the kinetic energy, the difference between the total and static temperature of each station reflects the gas kinetic energy. By comparing the total and static temperatures in Figure 6.18, it is desirable to use the total temperature rather than the static temperature as the reference temperature for the study of film cooling effectiveness and heat transfer coefficient since the total temperature is constant across the stators. In view of this, it is useful to define an overall film cooling effectiveness $\eta = (T_{t0} - T_{aw,f}) / (T_{t0} - T_{tc})$ based on the turbine inlet total temperature T_{t0} . As noted earlier, the adiabatic wall temperature $T_{aw,f}$ includes not only the temperature change due to film cooling but also the turbine work process. For the overall film cooling effectiveness in the turbine stage shown in Figures 6.19 and 6.20, the high cooling effectiveness in the leading portion is due to the coolant protection, while the high value in the trailing portion can be attributed to the low mainstream temperature caused by the turbine work process.

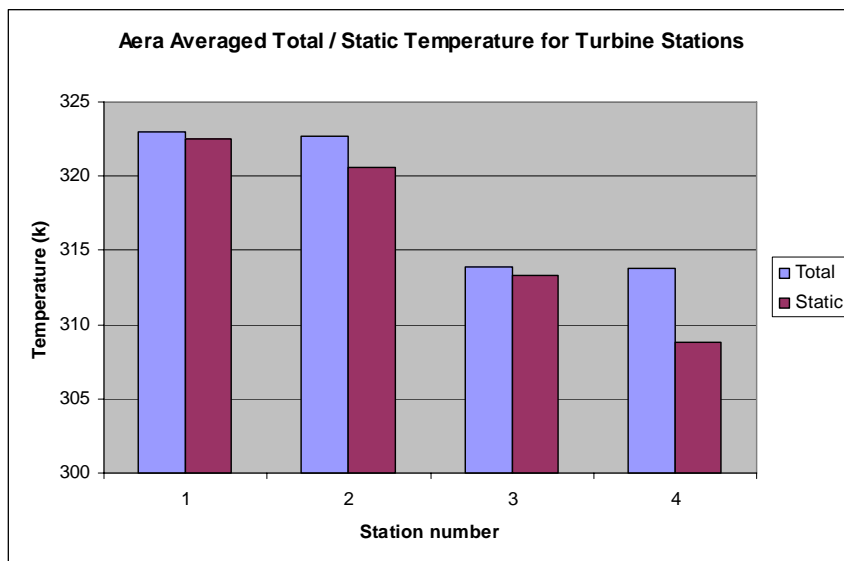


Figure 6.18 Area averaged total/static temperature for various stations in the turbine stage, 2550 rpm.

Figure 6.19 compares the three-dimensional coolant images in the rotor passage for various rotating speeds. Generally speaking, the coolant accumulates on the blade suction side due to the low pressure, decreases in the value and area, and lifts off towards to the trailing portion, shapes a curve triangle. Due to the horseshoe vortex on the blade leading edge root region, the coolant does not attach the leading edge suction side. For the adiabatic cooling effectiveness in Figure 6.19 (a), the 2000 rpm pushes the coolant to the middle of the rotor passage by the positive incident angle shown in Figure 6.7(b), and looks more concentrated compared with other conditions. With rpm increasing, the incident angle of inlet flow decreases, and the coolant is pushed more close to the suction side with more spreading on the lateral direction. For the 3000 rpm, some coolant is even pushed on the suction side of the blade instead of the

horseshoe vortex there. For the over-design 4000 rpm case, the cooling effectiveness decreases dramatically, and the shape looks more chaos.

Figure 6.19(b) compares the overall cooling effectiveness for various rpms. As noted before, the overall cooling effectiveness not only considers the coolant effect, but also the turbine work process impact. Therefore, high cooling effectiveness can be observed on the trailing portion of the blades, especially for the high rpm cases. Because the higher rpm, the more thermo energy has been extracted from the gas, and the lower temperature of turbine passage flow.

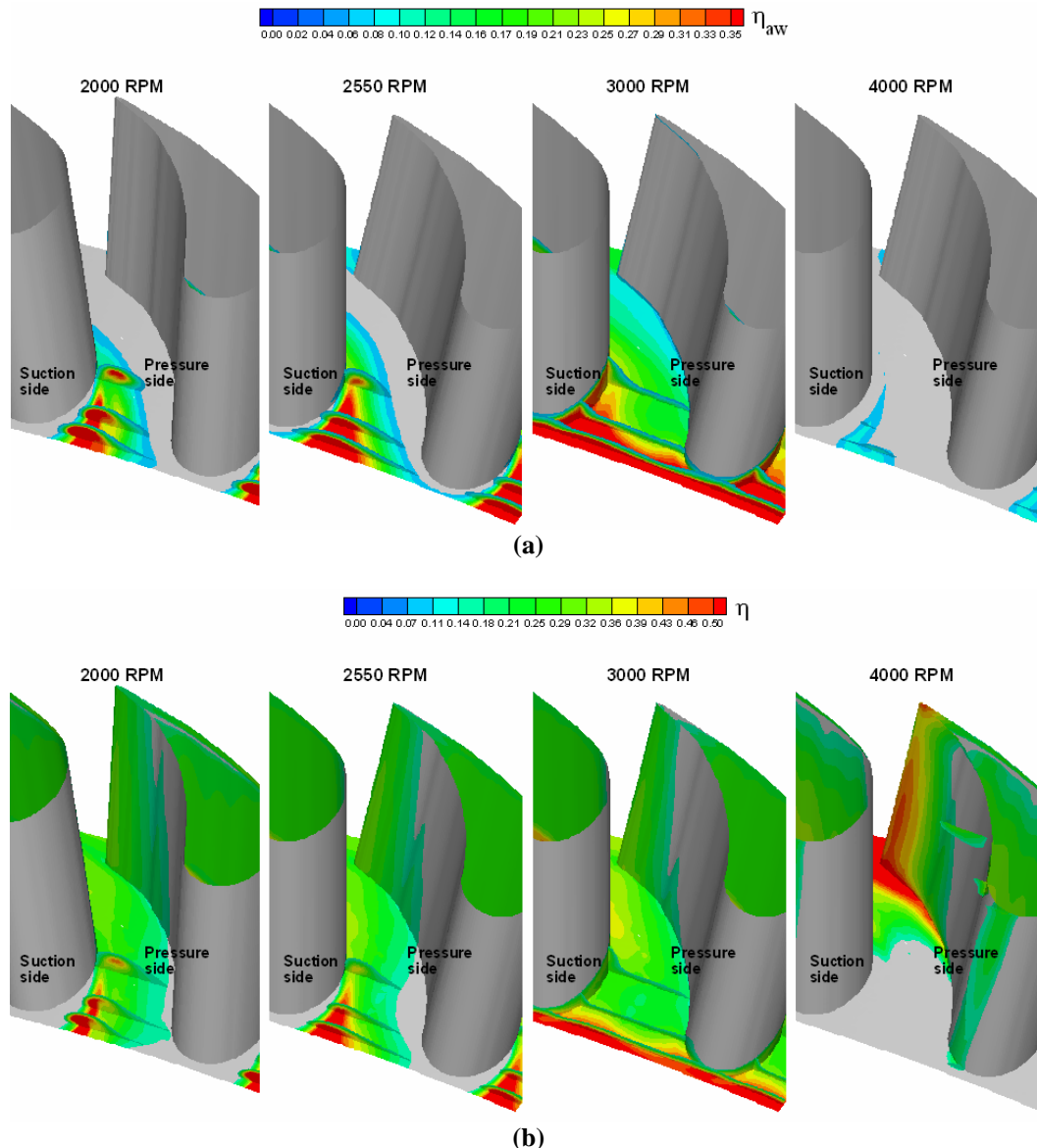


Figure 6.19 Coolant 3-D image comparison contoured by the adiabatic film cooling effectiveness (a) and overall film cooling effectiveness (b) inside a rotor passage for various rotating speeds, time phase $\frac{1}{4}$, MFR=1% ($M=0.24$).

Figure 6.20 compares the overall film cooling effectiveness on the rotor blade platform at four time phases for 2550 rpm condition with MFR = 1%. Generally, the difference of cooling effectiveness among the various time phases is not significant in the leading edge portion. The high cooling effectiveness stays outside of the blade leading edge due to the horseshoe vortex, and exists near the suction side due to coolant streamline convergence in the low pressure region. Also as indicated before, the high cooling effectiveness on the trailing portion is not due to the coolant protection. This is because of the turbine work process decreasing the mainstream temperature in the trailing portion, which is strongly influenced by the stator-rotor interaction for various time phases, especially in the rotor wake region.

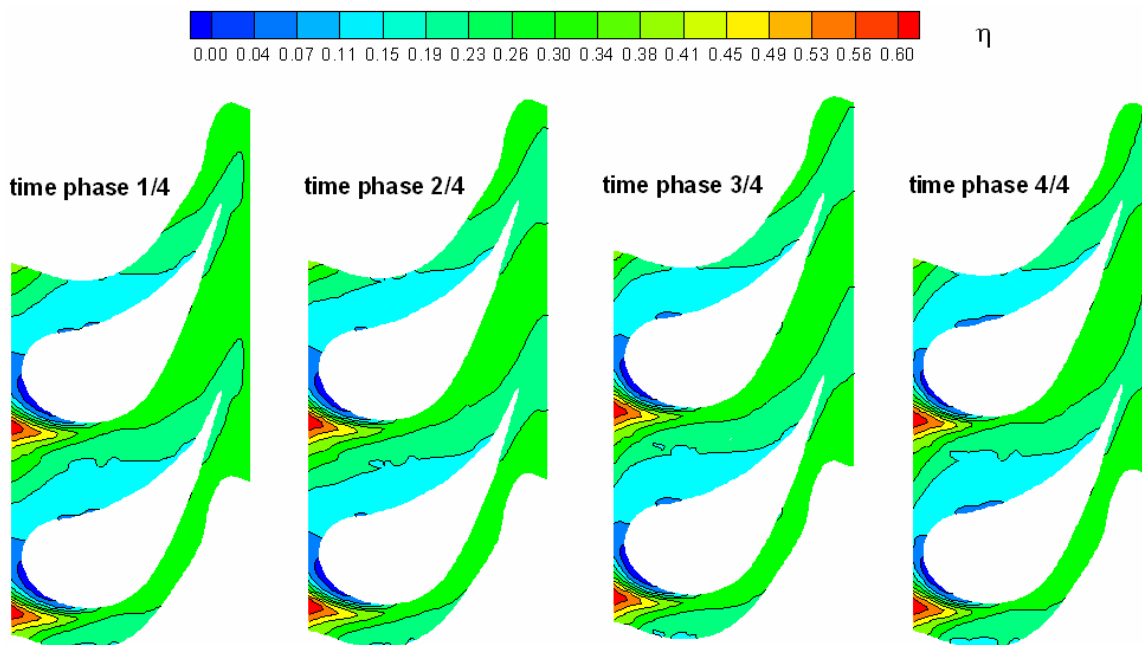


Figure 6.20 Overall film cooling effectiveness comparison on the rotating blade platform for various time phases, 2550 rpm, MFR=1% ($M=0.24$).

6.6. Conclusions of Platform Film Cooling

Numerical simulations were performed for the three-dimensional 1- $\frac{1}{2}$ turbine stage to determine the effect of coolant purging rate on the rotating platform film cooling and heat transfer of the first stage rotor blade. Three coolant purging ratios (0.5%, 1% and 1.5% of mainstream) and three rotating speeds (2000, 2550, 3000, and 4000 rpm) were investigated. Both the adiabatic and overall film cooling effectiveness, together with the heat transfer coefficient and overall heat transfer coefficient, were evaluated to determine the true effect of the film cooling as well as the combined effects of the turbine work process and coolant protection. The primary findings from this study are summarized as follows:

1) With increasing rotating speed, the inflow angle reduced significantly and the stagnation point on the rotor leading portion shifts gradually from the pressure side to the suction side. This affects the rotating platform film cooling and heat transfer.

2) The adiabatic film cooling effectiveness increases with increasing the rpm, until it reaches the best performance point, then drops dramatically.

3) In addition to the effects of rotating speed, the film cooling effectiveness is also affected by the coolant purging rate. For rang considered in this paper, the high coolant purging ratio increases the film cooling effectiveness.

4) The predicted laterally averaged adiabatic film cooling effectiveness is in good agreement with the corresponding experiment data except for the leading edge region. However, the detailed effectiveness distribution on the platform is not well predicted by the present study.

5) The best performance working condition provides a low unsteady intensity of film cooling effectiveness.

6) The overall heat transfer coefficient and film cooling effectiveness include the effect of both flow field and turbine work process, while the heat transfer based on the adiabatic wall temperature and adiabatic film cooling effectiveness only depend on the flow field.

CHAPTER VII

SUMMARY AND CONCLUSIONS

Turbine blade edge regions, including blade tip, leading edge and the platform, experience a high heat load. Numerical investigations have been applied on the flow and film cooling for these critical regions. The compressible Navier-Stokes equation, Reynolds stress turbulence model together with non-equilibrium wall function, have been solved by Fluent in these studies. Generally, the predicted pressure and heat transfer coefficient agree well with the experimental data, while the film cooling effectiveness tends to be over-predicted in the value. Major conclusions for the each blade regions are summarized as follows:

For the blade tip flow and heat transfer, both the experimental and numerical results show that the single suction side squealer tip is the best configuration to reduce the tip leakage flow and lower the heat transfer coefficient on the squealer cavity floor on the blade tip. For both the double squealer tip and single suction-side squealer tip, the heat transfer coefficient on the cavity floor also decreases with increasing cavity depth. However, the heat load rate was found to increase with increasing cavity depth since the available heat transfer area increases at a faster rate than the reduction in heat transfer coefficient. Therefore, it is desirable to use the tip configuration with shallow squealer cavity to reduce the overall heat load. For the 1.5% tip clearance cases considered here, the area averaged Stanton number and the heat load rate are only slightly affected by the blade rotation. However, the heat transfer coefficient on the stationary shroud is significantly higher under the rotating conditions due to dramatic increases of the velocity and temperature gradients in the shroud boundary layer. The heat transfer coefficients on the pressure and suction sides of the blade are also significantly changed due to the passage vortex migration induced by the blade rotation.

For the blade tip film cooling, the existence of film cooling does not affect the overall blade pressure ratio distribution significantly, except for the region downstream of the film holes. The upstream and two-row arrangements provide better film cooling performance on both the plane and squealer blade tips than the camber arrangement, especially at the high blowing ratios. When the blowing ratio M reaches 1, the film cooling effectiveness cease to increase for the camber arrangement on both the plane and squealer tips due to the coolant separation from the blade tip. However, the film cooling effectiveness in the upstream and the two-row arrangements still tend to increase with higher blowing ratios. The film cooling effectiveness on the shroud depends mostly on the blowing ratio, and is only slightly affected by the film-hole arrangements. The higher blowing ratio produces higher cooling effectiveness on the shroud for all cases considered. For the range of blowing ratio considered in the present study, the coolant jets act as a blockage to the tip leakage flow. Therefore, low heat transfer coefficient is dictated downstream of

the film holes on plane, squealer tips, and squealer shroud. The rotation reduces the film cooling effectiveness on the plane tip significantly, while the film cooling effectiveness on the squealer tip is only slightly affected due to the large cavity depth. The rotation significantly increases the heat transfer coefficient on the shrouds due to the increasing velocity and temperature gradient inside the shroud boundary layer. The simulation shows that the blade suction side does not benefit from the tip film cooling for all cases considered. The film cooling reduces the tip leakage mass flow rate for both the plane and squealer tip configurations. The squealer tip reduces the leakage flow velocity, but the overall leakage mass flow rate increases for the film-cooled cases due to increased flow area in the squealer cavity.

For the film cooling on the blade leading edge, the unsteady intensity of heat transfer coefficient with film cooling is significantly higher than that without film cooling. Because the coolant jet disturbs the mainstream flow, and magnifies the flow fluctuation caused by the rotor interaction. Also the off-design conditions yield more heat transfer fluctuation than the at-design condition does. The unsteady intensity of film cooling effectiveness is much higher than that of the heat transfer coefficient, which means the cooling effectiveness is much more sensitive to the rotor interaction than the heat transfer. When the rotating speed increases from the low rpm condition to the design and high rpm conditions, the stagnation line on the rotor blade shifts from the pressure side to the leading edge, then to the suction side, respectively due to the increasing incident angle of the rotor relative inlet velocity. Therefore, the film cooling protection moves from the suction side to the pressure side, so does the increased heat transfer coefficient downstream the film holes. The stagnation line is on the 2-D blade is not a simple straight line as the blade leading edge, which can be attributed by the changing of relative velocity incident angle at various span locations. It tilts from the pressure side root region to the suction side tip region. The increasing rotating speed produces more unsteady turbulent wake flow, although it reduces the rotor relative inlet velocity. The overall result increases the heat transfer coefficient, and decreases the film cooling effectiveness on the leading edge region of the rotor blade.

For the film cooling on the rotating blade platform, the increasing rotating speed change the relative velocity incident angle significantly and the stagnation point on the rotor leading portion shifts gradually from the pressure side to the suction side. The adiabatic film cooling effectiveness increases with increasing the rpm, until it reaches the design point, then drops dramatically for the high rpm condition. In addition to the effects of rotating speed, the film cooling effectiveness is also affected by the coolant purging rate. For range considered in this paper, the high coolant purging ratio increases the film cooling effectiveness. The predicted laterally averaged adiabatic film cooling effectiveness is in good agreement with the experiment data, except for the leading edge region. However, the detailed effectiveness distribution on the platform is not well predicted by the present study. This is maybe due to the turbulence model, or non-developed swirling flow inside the rotating cavity. The design working condition provides a low unsteady intensity of film cooling effectiveness and highest coolant protection. The overall heat

transfer coefficient and the overall film cooling effectiveness include the effects of both flow field and turbine work process, while the heat transfer coefficient (based on the adiabatic wall temperature) and the adiabatic film cooling effectiveness only depend on the flow field.

REFERENCES

- [1] Han, J.C., Dutta, S., and Ekkad, S.V. 2000, *Gas Turbine Heat Transfer and Cooling Technology*, Taylor and Francis, New York.
- [2] Ameri, A.A., Steinthorsson, E., Rigby, D.L., 1997, "Effect of Squealer Tip on Rotor Heat Transfer and Efficiency," Proceedings of ASME Turbo Expo, ASME Paper 97-GT-128.
- [3] Ameri, A.A., Steinthorsson, E. and Rigby, D.L., 1999, "Effects of Tip Clearance and Casing Recess on Heat Transfer and Stage Efficiency in Axial Turbines," ASME Journal of Turbomachinery, **121**, No.4, pp. 683-693.
- [4] Ameri, A.A. and Bunker, R.S., 2000, "Heat Transfer and Flow on the First Stage Blade Tip of a Power Generation Gas Turbine: Part 2: Simulation Results," ASME Journal of Turbomachinery, **122**, No. 2, pp. 272-277.
- [5] Bunker, R. S., Baily, J.C., and Ameri, A.A., 2000, "Heat Transfer and Flow on the First Stage Blade Tip of a Power Generation Gas Turbine: Part 1: Experimental Results," ASME Journal of Turbomachinery, **122**, No.2, pp. 263-271.
- [6] Ameri, A.A., 2001, "Heat Transfer and Flow on the Blade Tip of a Gas Turbine Equipped With a Mean-Camberline Strip," ASME Journal of Turbomachinery, **123**, No.4, pp. 704-708.
- [7] Yang, H., Acharya, S., Ekkad, S. V., Prakash, C., and Bunker, R., 2002, "Flow and Heat Transfer Predictions for A Flat-Tip Turbine Blade," Proceedings of ASME Turbo Expo, ASME Paper GT-2002-30190.
- [8] Yang, H., Acharya, S., Ekkad, S.V., Prakash, C., and Bunker, R., 2002, "Numerical Simulation of Flow and Heat Transfer Past a Turbine Blade with a Squealer-Tip," Proceedings of ASME Turbo Expo, ASME Paper GT-2002-30193.
- [9] Azad, GM S., Han, J.C., Teng, S., and Boyle, R., 2000, "Heat Transfer and Pressure Distributions on a Gas Turbine Blade Tip," ASME Journal of Turbomachinery, **122**, No.4, pp.717-724.
- [10] Azad, GM S., Han, J.C., and Boyle, R., 2000, "Heat Transfer and Pressure Distributions on the Squealer Tip of a Gas Turbine Blade," ASME Journal of Turbomachinery, **122**, No.4, pp. 725-732.

- [11] Azad, GM S., Han, J.C., Bunker, R.S., and Lee, C.P., 2002, "Effect of Squealer Geometry Arrangement on a Gas Turbine Blade Tip Heat Transfer," ASME Journal of Heat Transfer, **124**, No.3, pp. 452-459.
- [12] Papa, M., Goldstein, R.J., and Gori, F., 2002, "Effects of Tip Geometry and Tip Clearance on the Mass/Heat Transfer From a Large-Scale Gas Turbine Blade," Proceedings of ASME Turbo Expo, ASME Paper GT-2002-30192.
- [13] Kwak, J.S., Ahn J., Han, J.C., Lee, C.P., Boyle, R. and Gaugler, R., 2003, "Heat Transfer Coefficient on the Squealer Tip and Near Tip Region of a Gas Turbine Blade with Single Squealer," Proceedings of ASME Turbo Expo, ASME Paper GT2003-38907.
- [14] Kwak, J.S. and Han, J.C., 2002, "Heat Transfer Coefficient on a Gas Turbine Blade Tip and Near Tip Regions," 8th AIAA/ASME Joint Thermophysics and Heat Transfer Conference, St. Louis, June, 2002, AIAA-2002-3012.
- [15] Kwak, J.S. and Han, J.C., 2002, "Heat Transfer Coefficient on the Squealer tip and Near Squealer Tip Regions of a Gas Turbine Blade," 2002 ASME International Mechanical Engineering Congress & Exposition, New Orleans, ASME Paper IMECE 2002-31109.
- [16] Kim, Y.W., Abdel-Messeh, W., Downs, J.P., Soechting F.O., Steuber G.D. and Tanrikut, S., 1994, "A summary of the cooled turbine blade tip heat transfer and film effectiveness investigation performed by Dr. D.E. Metzger," Proceedings of ASME Turbo Expo 1994, ASME Paper 94-GT-167.
- [17] Ameri A.A. and Rigby, D.L., 1999, "A numerical analysis of heat transfer and effectiveness of film cooled turbine blade tip model," NASA/CR, 1999-209165.
- [18] Kwak, J.S. and Han J.C., 2002, "Heat transfer coefficient and film cooling effectiveness on a gas turbine blade tip," Proceedings of ASME Turbo Expo, ASME Paper GT-2002-30194.
- [19] Kwak J.S. and Han J.C., 2002, "Heat transfer coefficient and film cooling effectiveness on the squealer tip of a gas turbine blade," Proceedings of ASME Turbo Expo, ASME Paper GT-2002-30555.
- [20] Achary, S. Yang, H., and Ekkad, S., 2002, "Numerical simulation of film cooling on the tip of a gas turbine blade," Proceedings of ASME Turbo Expo, ASME Paper GT-2002-30553.

- [21] Hohlfield, E.M., Christophel, J.R., Couch, E.L., and Thole, K.A., 2003, "Predictions of cooling flow dirt purge holes along the tip of a turbine blade," Proceedings of ASME Turbo Expo, ASME Paper GT 2003-38251.
- [22] Ahn, J., Mhetras S.P. and Han, J.C., 2004, "Film cooling effectiveness on a gas turbine blade tip and shroud using PSP," Proceedings of ASME Turbo Expo, ASME Paper GT2004-53249.
- [23] Dunn, M.G., 1986, "Heat Flux Measurement for a Rotor of a Full Stage Turbine. Part I: Time averaged Results." ASME Journal of Turbomachinery, **108**, No.1, pp.90-97.
- [24] Dunn, M.G., George, W.K., Rae, W.J., Woodward, S.H., Moller, J.C., and Seymour, J.P., 1986, "Heat Flux Measurement for a Rotor of a Full Stage Turbine, Part II: Description of Analysis Technique and Typical Time-Resolved Measurements." ASME Journal of Turbomachinery, **108**, No.1, pp.98-107.
- [25] Abhari, R.S., and Epstein, A.H., 1994, "An Experimental Study of Film Cooling in a Rotating Transonic Turbine", ASME Journal of Turbomachinery, **116**, No.1, pp.63-70.
- [26] Takeishi, K., Aoki, S., and Sato, T., 1992, "Film Cooling on a Gas Turbine Rotor Blade." ASME Journal of Turbomachinery, **114**, No. 4, pp. 828-834.
- [27] Camci, C., and Arts, T., 1985, "Short-Duration Measurement and Numerical Simulation of Heat Transfer Along the Suction Side of a Gas Turbine Blade," ASME Journal of Engineering for Gas Turbines and Power, **107**, No.4, pp.991-997.
- [28] Camci, C., and Arts, T., 1985, "Experimental Heat Transfer Investigation Around the Film Cooled Leading Edge of a High Pressure Gas Turbine Rotor Blade," ASME Journal of Engineering for Gas Turbines and Power, **107**, No.4, pp. 1016-1021.
- [29] Mehendale, A.B., Ekkad, S.V., and Han, J.C., 1994, "Mainstream Turbulence Effect on Film Effectiveness and Heat Transfer Coefficient of a Gas Turbine Blade with Air and CO₂ Film Injection," International Journal of Heat and Mass Transfer, **37**, No.10, pp. 2707-2714.
- [30] Mehendale, A.B., Han, J.C., Ou, S., and Lee, C.P., 1994, "Unsteady Wake Over a Linear Turbine Blade Cascade with Air and CO₂ Film Injection. Part II: Effect on Film Effectiveness and Heat Transfer Distributions," ASME Journal of Turbomachinery, **116**, No. 4, pp. 730-737.

- [31] Du, H., Han, J.C., and Ekkad, S.V., 1998, "Effect of Unsteady Wake on Detailed Heat Transfer Coefficient and Film Effectiveness Distribution for a Gas Turbine Blade," ASME Journal of Turbomachinery, **120**, No. 4, pp. 808-817.
- [32] Schobeiri, M. T., Gilarranz, J.L, Johansen, E.S., 2000, "Aerodynamic and Performance Studies of a Three Stage High Pressure Research Turbine with 3-D-Blades, Design Points and Off-Design Experimental Investigations," Proceedings of ASME Turbo Expo, ASME Paper 2000-GT-484.
- [33] Schobeiri, M.T., Suryanarayanan A., Jermann, C., Neuenschwander, T. 2004,"A Comparative Aerodynamic and Performance Study of a Three-Stage High Pressure Turbine with 3-d Bowed Blades and Cylindrical Blades," Proceedings of ASME Turbo Expo, ASME Paper GT2004-53650.
- [34] Ahn, J., Schobeiri M.T., Han. J.C., and Moon H.K., 2004, "Film Cooling Effectiveness on the Leading Edge of a Rotating Turbine Blade," Proceedings of ASME Turbo Expo, ASME Paper, IMECE 2004-59852.
- [35] Abhari, R.S., Guenette, G.R., Epstein, A.H., and Giles, M.B., 1991, "Comparison of Time-Resolved Turbine Rotor Blade Heat Transfer Measurements and Numerical Calculations," Proceedings of ASME Turbo Expo, ASME Paper 91-GT-268.
- [36] Dunn, M.G., Kim, J., Givinkas, K.C., and Boyle, R.J., 1992, "Time Averaged Heat Transfer and Pressure Measurement and Comparison with Prediction for a Two-Stage Turbine." Proceedings of ASME Turbo Expo, ASME Paper 92-GT-194.
- [37] Lin, Y.L., Stephens, M.A., and Shih, T.I-P., 1997, "Computation of Leading Edge Film Cooling with Injection through Rows of Compound Angel Holes," Proceedings of ASME Turbo Expo, ASME Paper 97-GT-298.
- [38] Garg, V.K., and Ameri, A.A., 1997, "Comparison of Two-Equation Turbulence Models for Prediction of Heat Transfer on Film-Cooled Turbine Blades," Numerical Heat Transfer, Part A, **32**, No.4, pp.347-355.
- [39] Harasgama, S.P., and Burton, C.D., 1992, "Film Cooling Research on the Endwall of a Turbine Nozzle Guide Vane in a Short-Duration Annular Cascade, Part I: Experimental Technique and Results," ASME Journal of Turbomachinery, **114**, No.4, pp.734-740.

- [40] Harasgama, S.P., and Burton, C.D., 1992, "Film Cooling Research on the Endwall of a Turbine Nozzle Guide Vane in a Short-Duration Annular Cascade, Part II: Analysis and Correlation of Results," *ASME Journal of Turbomachinery*, **114**, No.4, pp.741-746.
- [41] Friedrichs, S., Hodson, H.P., and Dawes, W.N., 1996, "Distribution of Film-Cooling Effectiveness on a Turbine Endwall Measured Using the Ammonia and Diazo Technique," *ASME Journal of Turbomachinery*, **118**, No.1, pp. 613-621.
- [42] Roy, R.P., Squires, K.D., and Song, S. 2000, "Flow and Heat Transfer at the Hub Endwall of Inlet Vane Passages- Experiments and Simulations," *Proceedings of ASME Turbo Expo*, ASME Paper 2000-GT-198.
- [43] Burd, S.W., and Simon T.W., 2000, "Effects of Slot Bleed Injection Over a Contoured Endwall on Nozzle Guide Vane Cooling Performance: Part I – Flow Filed Measurements" *Proceedings of ASME Turbo Expo*, ASME Paper 2000-GT-199.
- [44] Burd, S.W., Satterness, C.J., and Simon, T.W., 2000, "Effects of Slot Bleed Injection Over a Contoured Endwall on Nozzle Guide Vane Cooling Performance: Part II- Thermal Measurements," *Proceedings of ASME Turbo Expo*, ASME Paper 2000-GT-200.
- [45] Radomsky, R.W., and Thole K.A., 2000, "High Free Stream Turbulence Effects on End Wall Heat Transfer for a Gas Turbine Stator Vane," *Proceedings of ASME Turbo Expo*, ASME Paper 2000-GT-2001.
- [46] Lin, Y-L, Shih T. I-P., 2000, "Effects of Gap Leakage on Fluid Flow in a Contoured Turbine Nozzle Guide Vane," *Proceedings of ASME Turbo Expo*, ASME Paper 2000-GT-0555.
- [47] Nicklas M. 2001, "Film-cooled Turbine Endwall in a Transonic Flow Field: Part II-Heat Transfer And Film-Cooling Effectiveness," *Proceedings of ASME Turbo Expo*, ASME Paper 2001-GT-0146.
- [48] Knost D. G. and Thole K.A., 2003, "Computational Predictions of Endwall Film-Cooling For a First Stage Vane," *Proceedings of ASME Turbo Expo*, ASME Paper GT2003-38252.
- [49] Zhang, L and Moon H.K., 2003, "Turbine Nozzle Endwall Inlet Film Cooling- The Effect of a Back-Facing Step," *Proceedings of ASME Turbo Expo*, ASME Paper GT2003-38319.

- [50] Han, S. and Goldstein, R.J., 2005, "Influence of Blade Leading Edge Geometry on Turbine Endwall Heat/Mass Transfer," Proceedings of ASME Turbo Expo, ASME Paper GT2005-68590.
- [51] Cardwell, N.D., Sundaram N., and Thole K.A., 2005, "Effects of Mid-Passage Gap, Endwall Misalignment and Roughness on Endwall Film-Cooling," Proceedings of ASME Turbo Expo, ASME Paper GT2005-68900.
- [52] Suryanarayanan, A., Mhetras, S.P., Schobeiri, M.T., and Han, J.C., 2006, "Film-Cooling Effectiveness on a Rotating Blade Platform," Proceedings of ASME Turbo Expo, ASME Paper, GT-2006-90034.
- [53] Fluent Inc., Version 6.0, 2002 CD-ROM, Fluent Inc, Lebanon, New Hampshire.
- [54] Hanjalic,K., 1994, "Advanced Turbulence Closure Models, A View of Current Status and Future Prospects," Intl. J. of Heat and Fluid Flow, **15**, No.3, pp. 178-200.
- [55] Launder, B. E., and Spalding, D. B., 1974, "The Numerical Computation of Turbulent Flows," Computer Models in Applied Mechanics and Engineering, **3**, No.2, pp. 269-289.
- [56] Chen H. and Patel V. 1988, "Near-Wall Turbulence Models for Complex Flows Including Separation," AIAA Journal, **26**, No.6, pp.641-648.
- [57] Bunker R.S. 2006, "Axial Turbine Blade Tips: Function, Design, and Durability", Journal of Propulsion and Power, **22**, No. 2, pp 271-285.
- [58] Bogard, D.G., Thole, K.A., 2006, "Gas Turbine Film Cooling," Journal of Propulsion and Power, **22**, No.2, pp. 249-269.
- [59] Simon, T.W., Piggush , J.D., 2006, "Turbine Endwall Aerodynamics and Heat Transfer," Journal of Propulsion and Power, **22**, No. 2, pp. 301-311

VITA

Huitao Yang received his Bachelor of Engineering in thermo energy engineering, and his first Ph.D. in aerospace propulsion theory and engineering from the Department of Aerospace Propulsion at Beijing University of Aeronautics and Astronautics, People's Republic of China. In August 2006, he received his second Ph.D. in mechanical engineering from Texas A&M University (College Station). Huitao Yang married Maggie Zhu, and has one daughter, Katherine.

Permanent address:
9801 Veridian Lane
Johnston, Iowa, 50131

Email: yang123@gmail.com